UNIVERSITY OF CALIFORNIA
RIVERSIDE

Cuprate Superconductivity Analysis via Helium Ion Microscopy

A Dissertation submitted in partial satisfaction
of the requirements for the degree of

Doctor of Philosophy

in

Physics

by

Jay Clayton LeFebvre

September 2021

Dissertation Committee:

Professor Shane A. Cybart, Chairperson
Professor Peng Wei
Professor Yong-tao Cui

The Dissertation of Jay Clayton LeFebvre is approved:

Committee Chairperson

University of California, Riverside

Acknowledgments

It takes an army to support advancements in science. I appreciate all the scientists for whom my work is based on and hope my own work will join that uninterrupted chain of progress stretching back millennia. First and foremost, I would like to acknowledge my advisor Shane Cybart for incubating an environment that provided the social and technical requirements in which novel science may be performed. I also profoundly appreciate his guidance through a quite meandering path that culminated in the following dissertation. Throughout my research career I have been blessed with a series of dedicated mentors. My first tentative steps into research were patiently overseen by Zachery Keane, Baladitya Suri, Jen-Hao Yeh, Sergei Novikov, Jennifer Robinson and Shavindra Premaratne. A very special thank you is given to Benjamin Palmer who cultivated the lab that brought this special group of scientists together. It was in his lab that I made the decision to dedicate my life to the pursuit of scientific research. I especially want to single out Ethan Cho who dedicated a non-trivial amount of time and effort to demonstrate and discuss with me the rigorous and not-so-glamorous details of performing research. I appreciate all these amazing scientists and people and recognize their influence on my work.

I would also like to acknowledge my generation of scientists for their time is now. I want to recognize my colleagues at ONELAB with whom I crawled through the trenches and built a fraternal bond that I have always dreamed about. I acknowledge especially Yanting Wang with whom I was tightly bonded due to the entanglement of our corresponding projects and our shared appreciation of Japanese culture. Also, I acknowledge Stephen McCoy, who demonstrated to me that being one of the greatest researchers doesn't require

conducting oneself with any decorum. I am proud to include Hao Li, Yuchao Zhou, Anthony Cortez, and Han Cai as scientific peers and close friends with whom we built something I would have considered magical if I didn't understand the physics of it. Miranda Vinay deserves to be specially called out as being brave enough and talented enough to tame several hydra-like manuscripts that threatened to outmatch me. I would also like to take the time to encourage ONELAB's next generation, Joseph Forman and Adhilsha Parachikunnumal. You have some large shoes to fill.

I would also like to acknowledge a long list of collaborators with whom much progress was made: Robert Dynes and Uday Goteti at UCSD, Kevin Pratt at Tristan Technologies, Inc., Leila Kasaei and Ke Chen at Temple University, Atsutaka Maeda at University of Tokyo, Ramamoorthy Ramesh at UCB, Horst Rogalla at NIST, Edward Bielejec at Sandia, Jiarui Li and Riccardo Comin at MIT, Nobuyuki Yoshikawa at Yokohama National University, Oleg Mukhanov at Hypres, Inc. and Chiharu Urano at AIST.

I would also like to gratefully acknowledge the funding agencies and sources that supported this endeavor. This work was supported by AFOSR Grant No. FA9550-20-1-0144, FA9550-17-C-0006 and FA9550-15-1-0218, NSF Grant No. 1664446, UCOP MRPI Award No. 009556-002, and ARO Grant W911NF1710504.

Finally, I thank my family and friends for supporting me during my adventure. My parents sparked my interest in science and physics and always encouraged and aided me to achieve my dreams. Their contribution cannot be understated. Its incomprehensible to me the totality of the ramifications on my life trajectory by picking up my two-in-one copy of Stephen Hawking's *A Brief History of Time* and *The Universe in a Nutshell*.

To my parents, without them I would not be here literally and figuratively

and

to Stephanie who has been a constant source of motivation and self-improvement.

ABSTRACT OF THE DISSERTATION

Cuprate Superconductivity Analysis via Helium Ion Microscopy

by

Jay Clayton LeFebvre

Doctor of Philosophy, Graduate Program in Physics
University of California, Riverside, September 2021
Professor Shane A. Cybart, Chairperson

Understanding superconductivity at high temperatures has been an evasive scientific hurdle. This dissertation outlines efforts taken by the author to exploit recent advances in nanofabrication through helium focused ion beam (He-FIB) microscopy for the advancement of scientific and technical understanding of high-transition temperature superconductivity. The He-FIB technology has recently been shown to be a promising technique for the fabrication of high-quality directly-written planar Josephson junctions (JJs) with tunable parameters in $YBa_2Cu_3O_{7-\delta}$ (YBCO). Herein, it is demonstrated that these He-FIB JJs are fundamental building blocks of common superconducting circuits in novel planar geometries like superconducting quantum interference devices, gradiometers, and single flux quantum logic. Furthermore, it is demonstrated that the He-FIB direct-write technique can be utilized in rare earth based cuprates, such as HoBCO, and exfoliated BSCCO, which may lead to advanced three-dimensional circuits by combining the He-FIB direct-written JJs with the intrinsic *c*-axis BSCCO JJs.

I demonstrate that series arrays of closely spaced, planar long JJs are transducers of

magnetic flux featuring high-dynamic range and wide-bandwidth and that they are operable at cryogenic nitrogen temperatures. For this application, a robust automated process using FIB nanolithography for layout designs with feature sizes from sub-nanometer to millimeter scales is developed. Additionally, the JJ array's geometry and properties for magnetic flux sensing are optimized. I present a series array of long JJs fabricated in YBCO containing 2640 JJs with a critical current deviation of 30% exhibiting a sensitivity of 1.7 mV/μT and a linear response over a range of 10 μT at 40 K, resulting in a dynamic range of 100 dB.

The exact nature of the order parameter is not completely understood in cuprate materials, which can impact the performance of these devices. Direct-written planar JJs offer a novel way to characterize cuprate superconductors in their a-b plane regarded to be the site of superconductivity in these materials. Measurements of the density of states are taken at variable angles to help determine the practical order pairing symmetry. Measurements indicate a significant s-wave component mixed with no more than 30% of the prominent d-wave symmetry.

Contents

List of Figures

List of Tables

Chapter 1

Introduction

The phenomenon of superconductivity is one that has fascinated researchers for decades and provides a unique material to exploit for the advancement of our understanding of the natural sciences. Originally stemming from the field of physics, the study of superconductivity has matured and permeated nearly all branches of science and engineering research. The fruit from these research efforts have far-reaching consequences in academic and commercial fields, influencing sectors such as health care, advanced computing, geology, and communication. While the contents of this work will focus on the physics of superconducting devices, there are also high-power applications for superconductivity in magnetics, transportation, and power transmission. Advancements in superconductivity can have profound impacts on humanity, from alleviating energy concerns to developing next generation computation. The demand for advancements in the field of superconductivity is continuously growing as the technical challenges facing humanity increase in complexity.

Superconductors and devices comprised thereof are not bereft from industry, such

as in magnetic resonance imaging (MRI) machines in radiology. However, their widespread use is limited by difficulty and cost of operation as the most sophisticated superconductors operate only at or below 4 K (-452 °F or -269 °C)[1]. Currently, one of the greatest technical and scientific challenges of superconductivity is its understanding at higher temperatures. Currently, researchers lack a fundamental theory describing these materials. Additionally, fabrication methods for them lack the sophistication of more widespread semiconductor electronics. This thesis outlines efforts of the author to advance the experimental science and techniques regarding superconductors operating at higher temperatures to achieve smaller sizes and improved performance with the hope of reducing the associated cost and difficulty of operating superconducting devices.

This work builds on the thesis work of my advisor, Shane Cybart, and my colleague, Ethan Cho, who developed a novel fabrication method for superconducting devices [1, 2]. This breakthrough technique allows for the fabrication of superconducting devices with smaller dimensions than previously demonstrated while operating at higher temperatures. Chapter 2 aims to provide background information on fundamental concepts in superconductivity and superconducting devices for physics and engineering students with limited prior exposure. Chapter 3 will discuss experimental techniques in the development of this work and the novel fabrication techniques pioneered by my advisor, colleagues, and myself. The following chapters will demonstrate basic circuit elements of superconducting devices fabricated with this novel method that demonstrate its scalability to larger, more complicated devices. Chapter 4 will outline advancements that culminated in the

[1]This is just a few degrees higher than the absolute lowest limits of temperature. Different units included for greater impact on the reader depending on where they were brought up. Scientists please don't prosecute the author at the use of imperial units. This introduction was crafted to accommodate all levels of scientific literacy not just the 98%.

prototype of a commercial superconducting magnetic field sensor first proposed by Shane Cybart. Finally, in Chapter 5 I will present a series of experiments that illuminate the underlying physics of the yet undiscovered fundamental theory of superconductors operating significantly above the lowest limits of temperature.

Chapter 2

Concerning Superconductivity

2.1 Historical Context

The history of superconductivity began in 1908, well over a hundred years prior to the author's study of its underlying physics. A great deal of effort has been expended since then to progress our scientific understanding. Like most scientific breakthroughs, its discovery relied on a paradigm shift caused by a related technological advancement. In 1908, Heike Kamerlingh Onnes was the first to liquefy helium, imparting the ability for scientists to probe physics at cooler temperatures than previously achieved [3]. It was not a coincidence that in 1911 he then announced that mercury exhibits a transition to zero resistivity when cooled to liquid helium temperatures [4]. The new state was found to be a perfect diamagnet, expelling all internal magnetic flux. This discovery was awarded the Nobel Prize in 1913 and was termed "superconductivity." Since then, research in superconductivity has produced its own expansive branch of research and has permeated many others, culminating in five Nobel Prizes awarded for related work.

A sufficient microscopic model for the prediction of superconducting behavior was not developed until 1957 [5]. In 1972, John Bardeen, Leon Cooper, and John Schrieffer shared the Nobel Prize for developing insight into the microscopic mechanisms of superconductivity, later colloquially referred to as the "BCS theory." Around the same time, Vitaly Ginzburg formulated a theory for the flow of magnetic fields within superconductors that is now termed as "type-I" [6]. Alexei Abrikosov would then expand on this work by predicting the behavior of magnetic flux that could penetrate and coexist inside a second category of superconductor at high magnetic fields, now referred to as "type-II" [7]. Together they would share the Nobel Prize in physics recognized in 2003.

In the early 1960s, Brian Josephson was defending his theory in which he claimed to explain the behavior of the current flowing without voltage across a non-superconducting junction which joined two superconducting electrodes [8]. Staunch critics argued the barrier must be electrically shorted. However in 1973, Josephson shared the Nobel Prize in physics for the theoretical prediction of quantum mechanical tunneling of superconducting charge carriers without voltage, referred to as the "Josephson effect." This effect was first experimentally reported by Phillip Anderson and John Rowell in 1963 [9], and the device would come to be known as a Josephson junction. Josephson junctions are fundamental components in superconducting devices in the same way that resistors, capacitors and inductors are in electronics.

BCS theory and the Josephson effect account for the theory of some of the most important applications of superconductors. An example application is their use in defining the international voltage standard [10]. Moreover, superconducting circuits have provided

the most sensitive detectors of magnetic flux by connecting one or two Josephson junctions in a loop, referred to as a "superconducting quantum interference device" or a "SQUID" [11, 12]. It is often shocking to contemporaries to know that it was the Ford Motor Company's research laboratory that first reported on its experimental demonstration [13]. Additionally, Josephson junctions are promising candidates for elements of advanced computing with applications in quantum mechanical computing [14], digital-based computing [15], reversible computing [16], and neuromorphic computing [17, 18]. Furthermore, they have applications in medicine [19, 20, 21], geology [22, 23, 24], and communication [25, 26, 27]. In fact, the Josephson junction is so synonymous with superconducting devices that there are too many important applications to list in this format. Novel applications are still being developed at the time of writing.[1] I direct the reader to Ref. [28, 29] to a more comprehensive list of the applications of Josephson junctions.

Given the many possible applications of Josephson junctions, one might question why superconducting devices aren't more prevalent in the commercial sector. As briefly discussed in Chapter 1, superconductors require immense cooling power that has historically required expensive cryogenics like liquid helium and bulky insulation. Moreover, the Josephson effect is difficult to measure requiring both low-noise electronics and technical experience for transport measurements. It wasn't until the discovery of superconductors operating at higher temperatures that researchers dared to hope that superconductivity could be brought to the masses. In 1987, the Nobel Prize was presented to Georg Bednorz and Alex Müller for their discovery of ceramic superconductors that boasted a superconducting transition at 30 K [30]. In quick succession thereafter, several ceramics were discovered with

[1] Several are subjects in this dissertation!

superconducting transition temperatures (T_C) above liquid nitrogen temperatures at ambient pressures [31, 32]. These discoveries kick-started the mania referred as the "Woodstock of Physics" at the 1987 American Physical Society's March Meeting conference. These materials captured the attention of physicists and they dreamed of a room temperature superconductor that would revolutionize technology and human innovation. Significant funding and research efforts were focused into the field of high-T_C superconductivity in the 1990s. Despite these efforts, progress wasn't advancing quickly enough and funding was diverted. Sophisticated fabrication techniques from low-T_C superconductors and semiconductor electronics were unsuitable for the complex ceramic crystal lattice structures common in high-T_C superconductors. Additionally, many of these high-T_C superconductors were found to deviate significantly from BCS theory and were termed "unconventional." A microscopic theory of high-T_C superconductivity remains elusive at this time. Despite this, progress in superconductivity will continue because the spirit of scientific advancement that inspired the Woodstock of Physics remains.

2.2 Theories of Superconductivity

Superconductivity is a phase change characterized by several unique observable behaviors. For example, current flows without voltage inside a superconductor, referred to as a "supercurrent." The London brothers Fritz and Heinz investigated the consequences of Maxwell's equations on a material featuring zero resistance, predicting the expulsion of the magnetic flux from within the resistance-less material [33]. In superconductors, the magnetic field is observed to be screened from within the material by the flow of supercurrent. This

phenomena is referred to as the Meissner Effect [34]. The London equations are able to predict the length scale to which the magnetic flux may penetrate into the material known as the London penetration depth (λ_L). λ_L is inversely proportional to the square root of the number density of available superconducting charge carriers and typically ranges from 10s to 100s of nanometers. Finally, magnetic flux quantization is observed within a loop of superconducting material, meaning total flux within the contour of that loop contains magnetic flux (Φ) which is equal to $n\Phi_0$, where n is some whole number and Φ_0 is the magnetic flux quantum [35]. Φ_0 was found to be $h/(2e)$, where h is Planck's constant, and e is the elementary charge. The observation of supercurrent and magnetic flux quantization in superconducting loops strongly indicates long range coherence causing the wavefunction interference to act macroscopically. Moreover, Φ_0 provides a strong first clue as to the underlying nature of the superconducting charge carriers and consequently the microscopic theory. These unique observables are exploited for applications that address complex technical challenges and, importantly, yield clues as to the fundamental nature of superconductivity.

London equations are good approximations for superconductors in weak fields; however, they can not capture local variations. This motivated the work by Pippard to expand on their model by introducing spatial variations [36]. He found that local variations could only occur within a spatial dimension referred as the coherence length. In addition to the phenomenological models, there have been several other models that have been shown to produce useful theories for the behavior of superconductivity. As mentioned previously, superconductivity is a phase change phenomenon. At some critical pressure

and/or temperature a material may undergo a superconducting transition. Consequently, the minimization of the free energy is a useful means of characterization. This macroscopic method used to describe superconductivity is termed the "Ginzburg-Landau theory" after the physicists who formulated it [37]. However, for the experiments elaborated on in this work, a microscopic theory of superconductors will be much more enlightening, so here the existence of the Ginzburg-Landau theory is noted for completeness.[2]

2.2.1 Electron Paired Bound State

Magnetic flux quantization was the major indicator towards formulation of BCS theory, due to its inclusion of $2e$. Therefore, the primary assumption of BCS is that the superconducting charge carriers are paired electrons. The notion of paired electrons violates basic intuition of electromagnetics. Cooper in 1956 demonstrated that a bound state was possible for an arbitrarily small attractive potential between two electrons at 0 K [39]. To maximize cross-sectional probability of interaction, it assumes each electron has equal momentum ($\vec{k}$) with opposite direction. Under the exchange of the two electrons a wavefunction must obey Pauli's exclusion principle, and hence Cooper's wavefunction is anti-symmetric. Either singlet or triplet spin functions were possible solutions in this model. Singlet states have cosinusiodal dependence ($\cos\vec{k}(\vec{r}_1 - \vec{r}_2)$)), whereas triplet states are products of sinusoidal functions ($\sin\vec{k}(\vec{r}_1 - \vec{r}_2)$)). For two electrons in close proximity, the wavefunction is maximized in the singlet state, so his model assumes a singlet state function.

Cooper's goal was to demonstrate that there was a solution to the wavefunction for

[2]I encourage dedicated readers towards Tinkham's *Introduction to Superconductivity* [38] for a full treatment of the Ginzburg-Landau theory which was my superconducting Bible throughout my graduate studies.

which its energy eigenvalues were less than the Fermi energy, which indicates the presence of a bound state of electrons. To greatly simplify this endeavor Cooper made the assumption that the electron scattering potential is a constant attractive potential (V) up to an energy limit, beyond which it is assumed to be zero. He found, based on these assumptions, that there was a bound state of electrons, regardless of the magnitude of the attractive potential. This demonstration is presented with more rigor in the following section, where the ground state of the BCS theory is calculated.

2.2.2 The BCS Ground State

In this section, the BCS ground state is calculated and Cooper's conclusions for an electron bound state are demonstrated.

When confronting the mathematics of BCS theory, some techniques from advanced quantum mechanics are introduced solely to organize the unwieldy expressions for quantum many-body problems. The following discussion will utilize the formulation of second quantization. This should not be a source of confusion since it is only being used as an abbreviated formalization for $N \times N$ Slater matrices, which may be recalled from undergraduate quantum mechanics as an expression for determining the anti-symmetry requirements of the wavefunction of two fermions.

Here I present a few assumptions. First, we will assume there is some unspecified attractive potential between the electrons. To simplify the mathematics, we will assume this potential is constant (-V) for energy states ($\vec{k}$) up to a cutoff energy ($\hbar\omega_c$) and the potential is equal to 0 for $\vec{k} > \hbar\omega_c$. Moreover, we expect the lowest-energy state to have zero total momentum, so we can assume electrons with equal and opposite momenta. Under

exchange of two electrons the wavefunction must be anti-symmetric. We will assume an anti-symmetric singlet spin function anticipating that it would maximize the probability amplitude of an attractive potential for electrons in close proximity. Now we can write down the most general N-electron wavefunction (ψ) for two interacting bodies:

$$|\psi_N\rangle = \sum g(\vec{k_i}, ...\vec{k_l}) c^*_{\vec{k_i}\uparrow} c^*_{-\vec{k_i}\downarrow} ... c^*_{\vec{k_l}\uparrow} c^*_{-\vec{k_l}\downarrow} |\psi_0\rangle \tag{2.1}$$

c^* and c are respectively the creation and annihilation operators for $\vec{k}$ which also include a spin index (σ). They obey the anti-commutation relations characteristic of fermion operators and they define the number operator $n = c^*_{\vec{k}\sigma} c_{\vec{k}\sigma}$. $|\psi_0\rangle$ is the vacuum state and g is a weighting function which mediates electron interaction. $\vec{k}$ runs through all occupied states in the energy band from $\vec{k_i}$ to $\vec{k_l}$.

Since there are a great number of particles being considered, we can make the approximation that N is fixed and work in the grand canonical ensemble. Therefore, the ground state wavefunction is written as

$$|\psi_G\rangle = \prod_{\vec{k}} (u_{\vec{k}} + v_{\vec{k}} c^*_{\vec{k}\uparrow} c^*_{-\vec{k}\downarrow}) |\psi_0\rangle \tag{2.2}$$

where $|u_{\vec{k}}|^2 + |v_{\vec{k}}|^2 = 1$. Suggesting the probability of a pair being occupied is given by $|v_{\vec{k}}|^2$. $u_{\vec{k}}$ and $v_{\vec{k}}$ differ by a phase factor $e^{i\varphi}$ that will be shown to be the phase of the macroscopic wavefunction.

There are several methods that can be used to solve for the BCS ground state coefficients. The modern approach is by canonical transformation, whereas the original BCS paper used a variational method. Here the variational method is used because it is commonly taught in undergraduate quantum mechanics classes.

The variational method begins by writing down the so called "reduced Hamiltionian" referred as such because it contains only terms of consequence in superconductivity.

$$H = \sum_{\vec{k}\sigma} \epsilon_{\vec{k}} n_{\vec{k}\sigma} + \sum_{\vec{k}\vec{l}} V_{\vec{k}\vec{l}} c^*_{\vec{k}\uparrow} c^*_{-\vec{k}\downarrow} c_{-\vec{l}\downarrow} c_{\vec{l}\uparrow} \tag{2.3}$$

Since we are considering a system at absolute zero, the chemical potential is equivalent to the Fermi energy. We can then set the zero of kinetic energy to be $E_F n$ and minimize the energy states by calculating

$$\delta \langle \psi_G | H - E_F n | \psi_G \rangle = 0 \tag{2.4}$$

which after applying the operators and defining $\xi_{\vec{k}} = \epsilon_{\vec{k}} - E_F$ (the grand canonical ensemble condition) becomes the energy states by calculating

$$\langle \psi_G | H - E_F n | \psi_G \rangle = 2 \sum_{\vec{k}} \xi v^2_{\vec{k}} + \sum_{\vec{k}\vec{l}} V_{\vec{k}\vec{l}} u_{\vec{k}} v_{\vec{k}} u_{\vec{l}} v_{\vec{l}} \tag{2.5}$$

We can minimize Eq. 2.5 by imposing the constraint $u^2_{\vec{k}} + v^2_{\vec{k}} = 1$. Utilizing Pythagoras and other trigonometric identities and combining the Eqs. 2.4 and 2.5 we arrive at the following

$$\tan 2\theta_{\vec{k}} = \frac{\sum_{\vec{l}} V_{\vec{k}\vec{l}} \sin 2\theta_{\vec{l}}}{2\xi_{\vec{k}}} \tag{2.6}$$

It becomes convenient to define

$$\Delta_{\vec{k}} = -\sum_{\vec{l}} V_{\vec{k}\vec{l}} u_{\vec{l}} v_{\vec{l}} = -\frac{1}{2} \sum_{\vec{l}} V_{\vec{k}\vec{l}} \sin \theta_{\vec{l}} \tag{2.7}$$

and

$$E_{\vec{k}} = (\Delta^2_{\vec{k}} + \xi^2_{\vec{k}})^{1/2} \tag{2.8}$$

$E_{\vec{k}}$ is the excitation energy of a quasi-particle. That is, electrons with energies far from the Fermi surface, of momentum $\hbar\vec{k}$. "Bogoliubon" is the name given to quasi-particle

excitations in superconductors. They are characterized as spin-1/2 fermions which are electrons or holes that have been excited from the ground state. Note that $\Delta_{\vec{k}}$ does not depend on $\vec{k}$ and indicates the minimum energy needed to excite a quasi-particle. We can solve for the coefficients by Eq. 2.6 and the definitions given by Eqs. 2.7 and 2.8

$$v_{\vec{k}}^2 = \frac{1}{2}\left(1 - \frac{\xi}{E_{\vec{k}}}\right) = \frac{1}{2}\left(1 - \frac{\xi_{\vec{k}}}{(\Delta^2 + \xi_{\vec{k}}^2)^{1/2}}\right) \tag{2.9}$$

and $u_{\vec{k}}^2$ is trivial due to the minimization constraint. Additionally, we note that the potential weighting coefficients $u_{\vec{k}}$ and $k_{\vec{k}}$ only depend on $\epsilon_{\vec{k}} - E_F$, and therefore the potential has spherical symmetry.

It is now possible to calculate the ground state energy and show that it is lower than the Fermi level, predicting a bound state. Eq. 2.5 and our definitions for the coefficients result in

$$\langle\psi_G|H - E_F n|\psi_G\rangle = \sum_{\vec{k}}\left(\xi_{\vec{k}} - \frac{\xi_{\vec{k}}^2}{E_{\vec{k}}}\right) - \frac{\Delta^2}{V} \tag{2.10}$$

We can compare this to the normal state where $\Delta = 0$

$$\langle\psi_N|H - E_F n|\psi_N\rangle = \sum_{|\vec{k}|<k_F} 2\xi_{\vec{k}} \tag{2.11}$$

and the difference is

$$\langle E\rangle_S - \langle E\rangle_N = \sum_{|\vec{k}|>k_F}\left(\xi_{\vec{k}} - \frac{\xi_{\vec{k}}^2}{E_{\vec{k}}}\right) - \frac{\Delta^2}{V} \tag{2.12}$$

If we replace the summation with an integral with integrands from E_F to $E_F + \hbar\omega_c$, and define $N(0)$ as the density of states at the Fermi level for electrons, in the weak-coupling approximation where $N(0)V \ll 1$ the preceding equation becomes

$$\langle E\rangle_S - \langle E\rangle_N = -\frac{1}{2}N(0)\Delta^2 \tag{2.13}$$

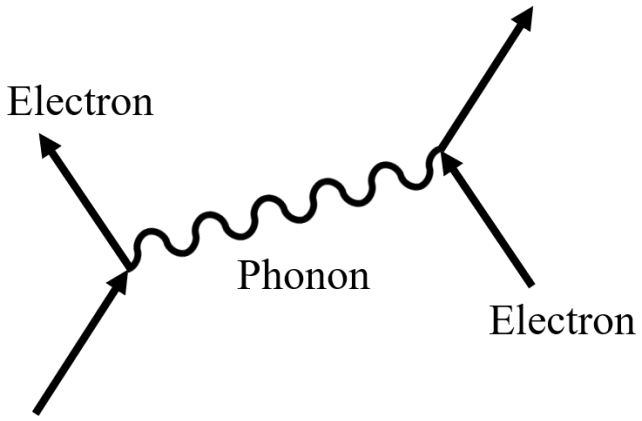

Figure 2.1: Feynman diagram representation of electron-phonon interaction that mediates the BCS attraction potential.

Consequently, there is a bound state no matter how small V is since V is cancelled out. This bound state is singlet pairing of two electrons resulting in a bosonic particle which is termed as the "Cooper pair" and it is the charge carrier in superconductors. This results in a collapse of the paired electrons into a macroscopic and highly degenerate ground state as the electrons are no longer bound to higher energy states by the Pauli exclusion principle.

The nature of the electron pairing term for BCS theory is suggested to be a retarded potential that is resultant of electron-lattice interactions [40]. The theory is that an initial electron polarizes nearby ion cores as it passes through the lattice. Then, a second electron is attracted to these positively polarized cores resulting in an attraction potential between the two electrons. Fig. 2.1 represents this interaction in the form of a Feynman diagram. If this electron-lattice mediated potential is greater than the repelling Coulomb potential, there is a net negative potential which results in superconductivity. This theory was supported by experiment [41, 42]. Its important here to note that BCS assumes an isotropic attraction potential, however our requirement for the formation of Cooper pairs is only that we can

approximate the potential as -V near E_F. Different natures of attractive potentials may lead to superconductivity with *other symmetries* of electron pairing.

2.2.3 Superconducting Order Parameter

Lets examine the density of states by comparing the excitations of quasi-particles by equating the superconducting density of states ($N_s(E)$) and the normal density of states ($N_n(\xi)$)

$$N_s(E)\ dE = N_n(\xi)\ d\xi \tag{2.14}$$

If we consider energies ξ near the Fermi energy we can assume $N_n(\xi) = N(0)$ leading to

$$\frac{N_s(E)}{N(0)} = \frac{d\xi}{dE} = Re\left[\frac{E}{(E^2-\Delta^2)^{(1/2)}}\right] \tag{2.15}$$

Fig. 2.2 plots the density of states for the BCS superconductor and compares them to the normal state at absolute zero temperature. It is now obvious that Δ characterizes an energy gap in the density of states. Quasi-particles with $E < \Delta$ are paired and condense into the BCS ground state. We observe that quasi-particle energy states are pushed above Δ resulting in a peak that approaches the constant $N(0)$ for $E \gg \Delta$.

In the phenomenological theory formulated by Ginzburg and Landau, Δ is the order parameter which characterizes the degree of phase transition. Importantly, it is also related to the superconducting attractive potential. Δ may be obtained by measuring the density of states of the superconducting material. Therefore, measurement of Δ yields fundamental information regarding the nature of the superconducting pairing potential.

Thus far we have limited the analysis to a system at absolute zero temperature. Of course, achieving that in experiment is impossible so it is more practical to consider Δ

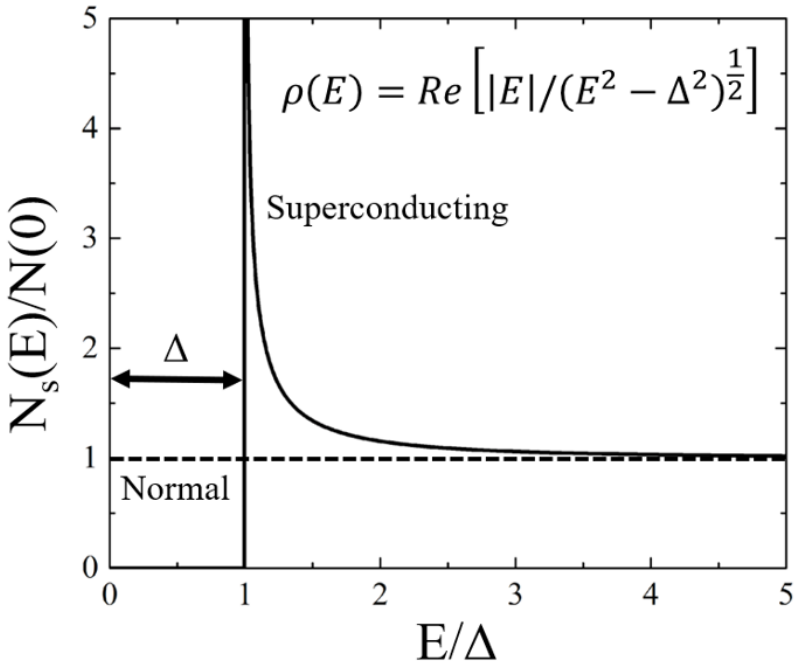

Figure 2.2: Density of states for the BCS superconductor (solid line) compared to the normal state (dotted line) at absolute zero temperature.

at finite temperatures. The Fermi function gives the probability of an excitation at thermal equilibrium

$$f(E_{\vec{k}}) = (e^{\beta E_{\vec{k}}} + 2)^{-1} \tag{2.16}$$

where β is defined as the inverse of the product of the Boltzmann constant k_B and temperature (T) or $1/(k_B T)$. Applied to our definition for Δ

$$\Delta_{\vec{k}} = -\sum_{l} \frac{\Delta_{\vec{l}}}{2E_{\vec{l}}} V_{\vec{k}\vec{l}} \tanh \frac{\beta E_{\vec{l}}}{2} \tag{2.17}$$

If we utilize the BCS approximation of a constant potential and that Δ does not have any $\vec{k}$ dependence, the preceding Eq. becomes

$$\frac{1}{V} = \frac{1}{2} \sum_{\vec{k}} \frac{\tanh \beta E_{\vec{k}}/2}{E_{\vec{k}}} \tag{2.18}$$

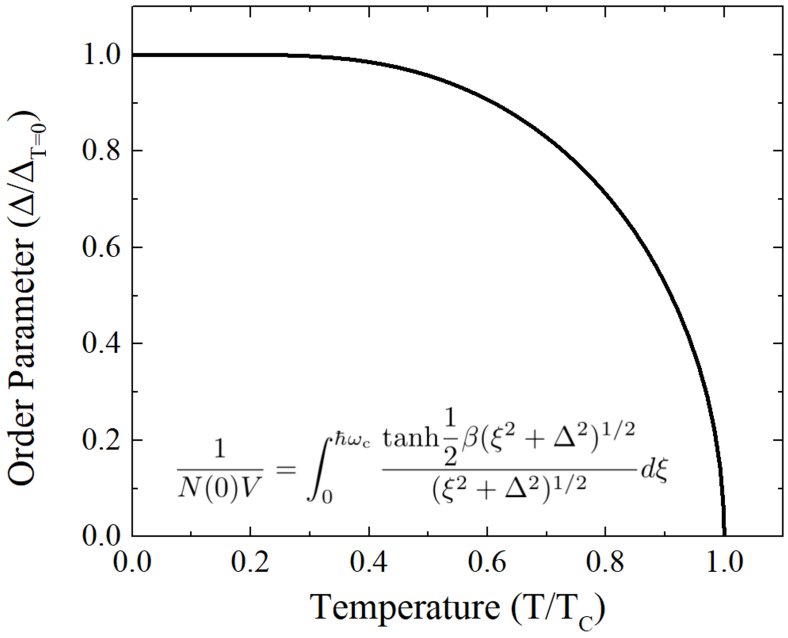

Figure 2.3: Normalized energy gap as a function of normalized temperature, determined by BCS in the weak-coupling limit.

We have the temperature dependence of Δ. Note that Δ goes to zero at some temperature that we will call the critical temperature (T_C). This behavior suggests that the energy gap is the order parameter. We can perform the same conversion from sum to integral as was utilized in the formulation of Eq. 2.13

$$\frac{1}{N(0)V} = \int_0^{\hbar\omega_c} d\xi \, \frac{\tanh\frac{1}{2}\beta(\xi^2+\Delta^2)^{1/2}}{(\xi^2+\Delta^2)^{1/2}} \tag{2.19}$$

Now $\Delta(T)$ may be computed by numerical integration [43]. Fig. 2.3 yields the normalized energy gap vs. normalized energy. Often the dimensionless quantity, $\Delta_{BCS}(0)/k_BT_C \approx 1.76$, is compared against experimental values to determine how well a real material follows theoretical predictions.

2.3 Electron Tunneling

The most accurate measurements of the superconducting energy gap are done using quasi-particle tunneling measurements, which involve measuring the conductivity at the interface of two bulk materials [44]. In the quantum mechanical tunneling of Bogoliubons across a superconducting junction, the characteristic coherence factors of the superconducting wavefunction ($u_{\vec{k}}$ and $v_{\vec{k}}$) do not contribute to the current across the junction, which is related to a constant tunneling probability which we will define as $|G|^2$. Consequently, we can utilize the so-called "semiconductor model" for electron tunneling in a superconducting junction which is commonly visualized in Fig. 2.4.

We will start by considering the general geometry of two bulk metals with a thin barrier at their interface. In the semiconductor model, all the states are filled up to the E_F at absolute zero temperature. Additionally, we will once again utilize the Fermi function to qualify thermal excitations. We can model the current across the junction geometry as

$$I = |G|^2 \int_{-\infty}^{\infty} dE\ N_2(E+V)N_1(E)[f(E) - f(E+V)] \tag{2.20}$$

This is a general model for normal, superconducting, or mixed bulk material junctions. In the normal-insulating-normal (NIN) junction, the density states N are constant.

$$I_{NIN} = |G|^2 N_1(0)N_2(0) \int_{-\infty}^{\infty} dE\ [f(E) - f(E+V)] = |G|^2 N_1(0)N_2(0)eV \tag{2.21}$$

Notice, that Eq. 2.21 only depends on constant terms and V so that it resolves the ohmic expression with the conductance defined as $|G|^2 N_1(0)N_2(0)e$.

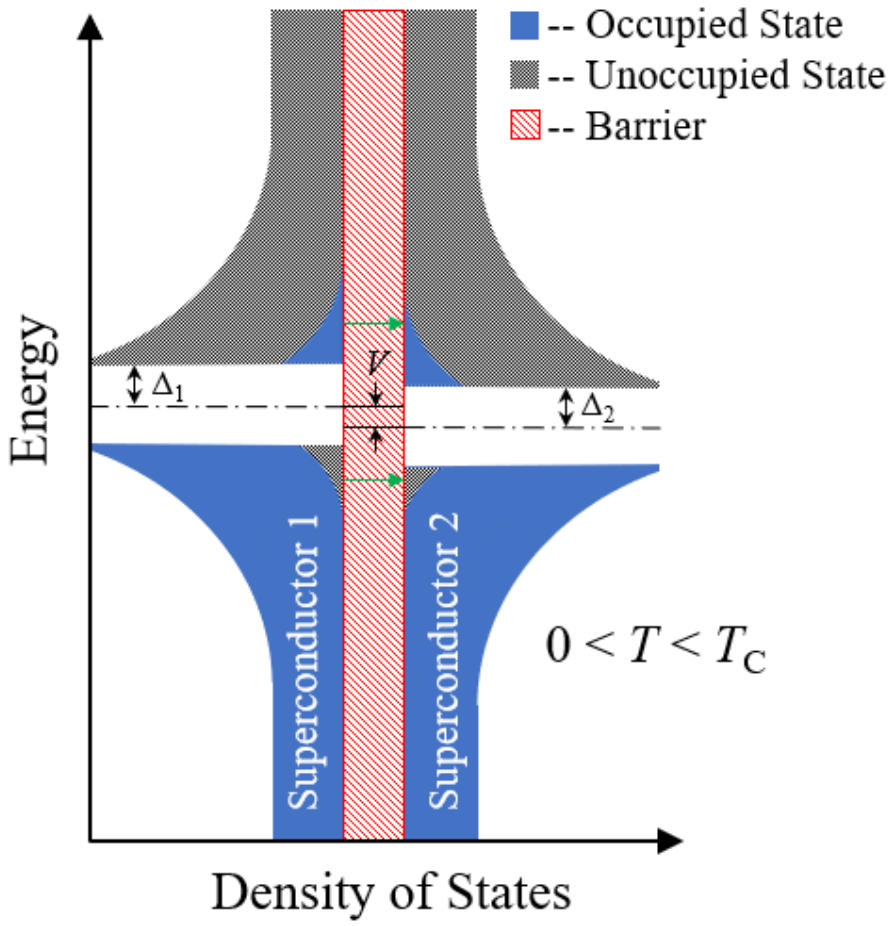

Figure 2.4: Illustration representing the semiconductor model of superconductor-superconductor tunneling with bias voltage (V) less than $\Delta_1 + \Delta_2$ at $0 < T < T_C$.

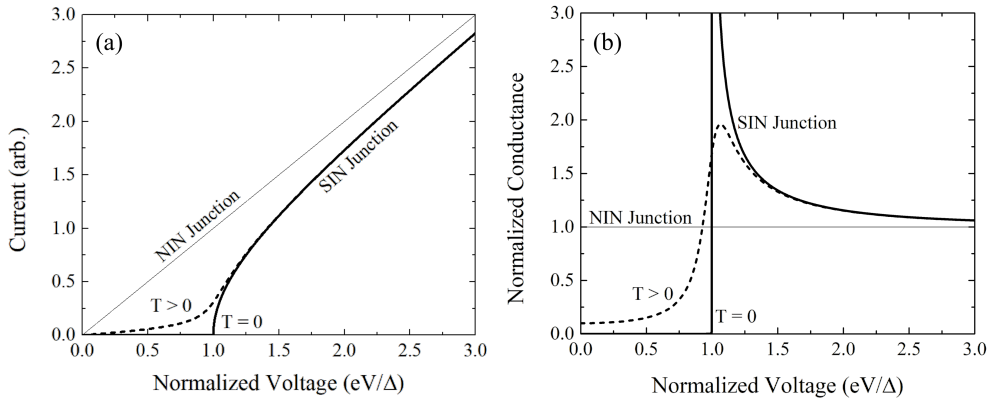

Figure 2.5: Characteristics of quasi-particle tunneling in normal-normal (thin line) and normal-superconductor junctions (thick lines). a) Current (in arbitrary units)-voltage characteristics. b) Differential conductance (normalized to the normal metal conductance) vs. voltage. Voltage is normalized to the energy gap (Δ). Solid curves for $T = 0$ and dashed curves for finite temperature.

Next, the superconductor-insulator-normal (SIN) junction is presented.

$$I_{SIN} = |G|^2 N_N(0) \int_{-\infty}^{\infty} dE \; N_S(E)[f(E) - f(E+V)] \tag{2.22}$$

This expression may be calculated by numerical means. Examples of the current-voltage and differential-conductivity characteristics for NIN and SIN junctions are plotted in Fig. 2.5.

While it is possible to measure the density of states in a SIN junction, the resolution for determining Δ is greater in superconducting-insulator-superconducting (SIS) junctions since the peaks in conductivity just above the gap will be sharper. Elaborating on SIS junctions, if Eq. 2.15 is inserted into Eq. 2.20, we arrive at the electron tunneling current

$$I_{SIS} = \frac{1}{eR} \int_{-\infty}^{\infty} dE \; \frac{|E|}{(E^2 - \Delta_1^2)^{1/2}} \frac{|E+V|}{[(E+V)^2 - \Delta_2^2]^{1/2}} [f(E) - f(E+V)] \tag{2.23}$$

Here R is the normal state resistance. It should be noted explicitly here that the prior discussion of electron tunneling is strictly limited to Bogoliubons, or non-Cooper pair charge

carriers.

If we take a more generalized approach and now include Cooper pair charge carriers, we can examine the zero applied voltage case. For this case, our previous assumptions regarding the tunneling probability fails. A more general case of the tunneling probability with matrix elements G_{kq} that includes arbitrary phase is required. There is a set of highly degenerate states with equivalent total electrons but differing number of Cooper pairs on either bulk electrode. For a phase coherent superposition of these states, a diagonal matrix element exists [45]. This may be expressed in the following expression

$$I_{SIS}|_{V=0} = \sin(\varphi) \left\{ 4e \sum_{kq\sigma} \frac{|G_{kq} G_{-k-q} \Delta_1^* \Delta_2|}{4 E_q E_k} \times P \left[\frac{f(-E_q) - f(-E_k)}{E_q - E_k} + \frac{f(E_q) - f(-E_k)}{E_q + E_k} \right] \right\} \quad (2.24)$$

where k and q represent the 1 and 2 bulk materials and $P[x]$ is the principle value of x. This expression hints at a coherent supercurrent across the junction and will be elaborated on in Sec. 2.5.

For practical purposes, Eq. 2.23 is unwieldy. It is preferable to use a phenomenological model for the density of states. Dynes et al. crafted such a model that is useful for characterizing most conventional superconductors [46]

$$N_{Dynes}(E, \Gamma) = Abs \left[\frac{E - i\Gamma}{[(E - i\Gamma)^2 - \Delta^2]^{1/2}} \right] \quad (2.25)$$

This expression captures the broadening of the gap edge in the density of states due to thermally excited quasi-particles characterized by the Γ term. Examples of Eq. 2.25 is plotted with several varying Γ in Fig. 2.6.

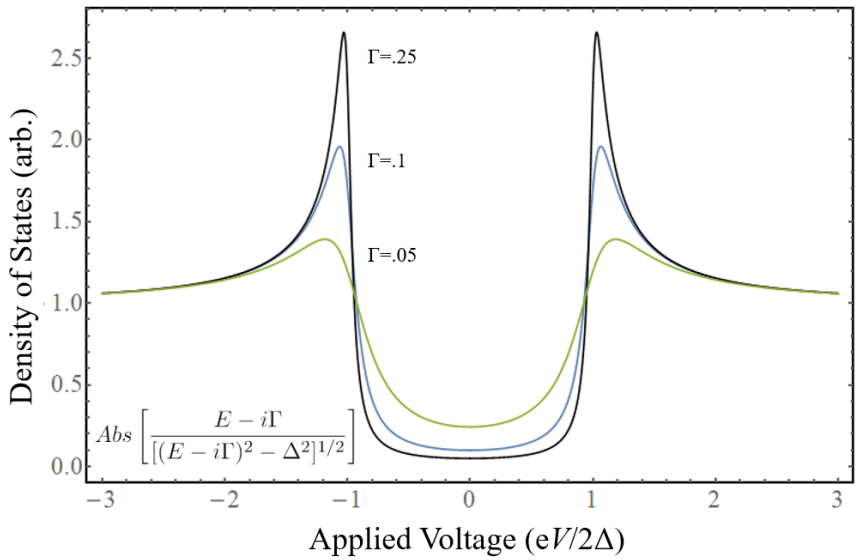

Figure 2.6: Phenomenological model for density of states for electron tunneling in a superconducting-insulating-superconducting junction at finite temperature for varying $\Gamma =$ .25 (Black), .1 (Blue), and .05 (Green).

Here it is important to also comment on the nature of the junction barrier. Blonder, Tinkham and Klapwijk devised a clever semiclassical model for normal-superconductor junctions that examines interfaces with arbitrary strength from the metallic to the tunneling regime [47]. They found that with weak barriers, an electron scattering event may produce a Cooper pair and a reflected hole. These scattering events are known as "Andreev reflections" and generate current. This is referred to as "excess current" that is not modulated by the superconducting macroscopic phase [48]. Therefore, it is important for tunneling experiments to utilize a strong barrier to prevent the excess current from poisoning the transport measurements.

2.4 Long Range Coherence

By calculating the BCS ground state, it was shown that two electrons form Cooper pairs that obey Bose-Einstein statistics because the sum of the spin quantum numbers is an integer. Many of these charge carriers near the Fermi surface condense into the same energy state, which is the superconducting ground state. This results in the overlap of many Cooper pairs. A macroscopic phase coherence forms that minimizes the free energy as the phases become locked together. This superfluid condensate can be described by a single wavefunction, sometimes referred to as the order parameter. Furthermore, this superfluid state has important effects on the flow of charge carriers allowing resistance-less supercurrent. This macroscopic wavefunction varies over a characteristic length scale referred to as the coherence length (ξ) and also defines a length scale between paired electrons. It is this phase coherence that accounts for the observation of magnetic flux quantization, since the phase of this macroscopic wavefunction must remain single valued and unique. Therefore, around any contour of superconducting material the phase must advance 2π onto itself. This condition enforces that any flux threading within that contour is quantized to values $n\Phi_0$.

2.5 The Josephson Effect

While investigating electron tunneling, Eq. 2.23 hinted at a coherent tunneling of Cooper pairs across a non-superconducting barrier sandwiched between two superconducting electrodes in the absence of a voltage difference across the junction. This phenomenon, known as the "Josephson effect," was named after the theorist who first described this

device's behavior [8]. Recall that devices that are characterized by the Josephson effect are referred to as Josephson junctions and are fundamental components of superconducting circuits.

Josephson was able to derive the Josephson effect by considering a Cooper pair tunneling term that was omitted in the original formulation of BCS theory. To derive the Josephson equations, first consider the coupling between two wavefunctions ($\psi = \sqrt{\rho}e^{i\phi}$) of superconducting electrodes across a barrier, where ρ is the Cooper pair density and ϕ is the superconducting phase of the respective superconducting bulk electrode. We can define K to be the coupling constant and V to be the potential across the barrier, and write down the coupled Schrödinger equations for the system

$$i\hbar\frac{\partial}{\partial t}\begin{pmatrix}\psi_1\\ \\ \psi_2\end{pmatrix} = \begin{pmatrix}eV & K\\ \\ K & -eV\end{pmatrix}\begin{pmatrix}\psi_1\\ \\ \psi_2\end{pmatrix} \tag{2.26}$$

We can substitute in ψ and arrive at the following system of equations

$$\begin{cases} \frac{\dot{\rho_1}}{2\sqrt{\rho_1}}e^{i\phi_1} + i\dot{\phi_1}\sqrt{\rho_1}e^{i\phi_1} = -\frac{i}{\hbar}(eV\sqrt{\rho_1}e^{i\phi_1} + K\sqrt{\rho_2}e^{i\phi_2}) \\ \\ \frac{\dot{\rho_2}}{2\sqrt{\rho_2}}e^{i\phi_2} + i\dot{\phi_2}\sqrt{\rho_2}e^{i\phi_2} = -\frac{i}{\hbar}(-eV\sqrt{\rho_2}e^{i\phi_2} + K\sqrt{\rho_1}e^{i\phi_1}) \end{cases} \tag{2.27}$$

Taking the real part of the preceding equation

$$\begin{cases} \frac{\dot{\rho_1}}{2\sqrt{\rho_1}} = \frac{K}{\hbar}\sqrt{\rho_2}\sin(\phi_2 - \phi_1) \\ \\ \frac{\dot{\rho_2}}{2\sqrt{\rho_2}} = \frac{K}{\hbar}\sqrt{\rho_1}\sin(\phi_1 - \phi_2) \end{cases} \tag{2.28}$$

Assuming the two superconducting electrodes are the same material, defining the macroscopic superconducting phase as $\varphi = \phi_2 - \phi_1$ and summing the two conjugate equations yields

$$\dot{\rho} = 2\frac{K}{\hbar}\sin(\varphi) \tag{2.29}$$

This is Josephson's first equation, or the so called DC Josephson equation, which resembles Eq. 2.23. It describes a supercurrent I that flows without resistance up to a critical current I_C without a potential difference across the barrier. This is more conventionally expressed as

$$I = I_C \sin(\varphi) \tag{2.30}$$

Now if we consider the imaginary part of Eq. 2.27

$$\begin{cases} \sqrt{\rho_1}\dot{\phi_1} = -\frac{i}{\hbar}[eV\sqrt{\rho_1} + K\sqrt{\rho_2}\cos(\phi_2 - \phi_1)] \\ \sqrt{\rho_2}\dot{\phi_2} = -\frac{i}{\hbar}[-eV\sqrt{\rho_2} + K\sqrt{\rho_1}\cos(\phi_1 - \phi_2)] \end{cases} \tag{2.31}$$

Once again assuming the same material and subtracting the two conjugate equations one finds

$$V = \frac{\hbar}{2e}\frac{\partial\varphi}{\partial t} \tag{2.32}$$

This is Josephson's second equation, or the so called AC Josephson equation, which describes that the voltage across the barrier is given by the time dependence of the macroscopic phase difference.

A fixed voltage will indicate a linearly varying φ in time. Consequently, Josephson junctions are characterized as non-linear inductors. The Josephson equations may be rewritten as

$$\begin{aligned} \frac{\partial I}{\partial \varphi} &= I_C \cos\varphi \\ \frac{\partial \varphi}{\partial t} &= \frac{2\pi}{\phi_0} V \end{aligned} \tag{2.33}$$

Applying the chain-rule and massaging Eq. 2.33 becomes

$$V = \frac{\Phi_0}{2\pi I_C \cos\varphi}\frac{\partial I}{\partial t} \tag{2.34}$$

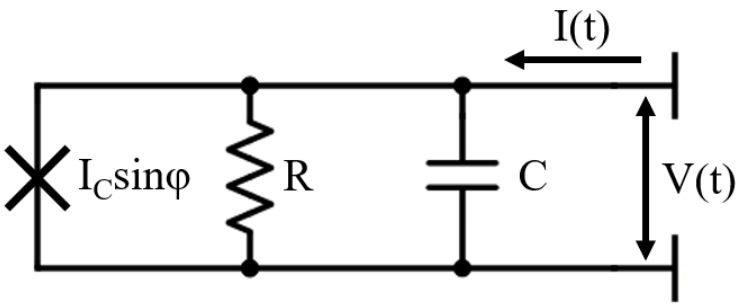

Figure 2.7: Equivalent circuit for the resistively and capacitively shunted model for a Josephson junction.

Here we can define a kinetic inductance as a function of the phase

$$L(\varphi) = \frac{\Phi_0}{2\pi I_C \cos\varphi} = \frac{L_J}{\cos\varphi} \tag{2.35}$$

where L_J, the Josephson inductance, is a fundamental parameter of the Josephson junction and is inversely proportion to the I_C.

By analogy to Faraday's law, it is therefore possible to store energy in a Josephson junction.

$$\Delta E = \int_{t_1}^{t_2} dt\ IV = \int_{t_1}^{t_2} d\Phi\ I_C \sin\varphi = \frac{I_C\Phi_0}{2\pi}\int_{\varphi_1}^{\varphi_2} d\varphi\ I_C \sin\varphi = -\frac{I_C\Phi_0}{2\pi}\cos\varphi \tag{2.36}$$

Here we can define the change in energy as a function of the phase

$$E(\varphi) = -\frac{I_C\Phi_0}{2\pi}\cos\varphi = -E_J\cos\varphi \tag{2.37}$$

where E_J, the Josephson coupling energy, characterizes the reduction in energy of the uncoupled system as compared to the coupled one.

2.5.1 The Resistively Capacitively Shunted Junction Model

The resistively capacitively shunted junction (RCSJ) model was simultaneously arrived at by the physicists Stewart and McCumber [49, 50]. They both considered the DC Josephson component in parallel with a resistor (R) and capacitor (C) (see Fig. 2.7). If we consider such a system with Kirchhoff's rules for circuits we arrive at the following expression

$$I = I_C \sin\varphi + \frac{V}{R} + C\frac{dV}{dt} \tag{2.38}$$

We can insert Josephson's second equation (Eq. 2.32)

$$I = I_C \sin\varphi + \frac{\hbar}{2eR}\frac{d\varphi}{dt} + \frac{\hbar C}{2e}\frac{d^2\varphi}{dt^2} \tag{2.39}$$

It is common to rewrite the preceding equation using dimensionless variables

$$\frac{I}{I_C} = \sin\varphi + \frac{d\varphi}{d\theta} + \beta_C\frac{d^2\varphi}{d\theta^2} \tag{2.40}$$

By defining the following

$$\theta = \frac{2e}{\hbar} I_C R t \tag{2.41}$$

and the so called "Stewart-McCumber parameter"

$$\beta_C = \frac{2e}{\hbar} I_C R^2 C \tag{2.42}$$

Eq. 2.40 is a second order differential equation that is analogous to a driven damped pendulum and can be solved for arbitrary values of β_C by numerical integration. Solving this equation can yield the time-varying phase (See Fig. 2.8) which can be input to the Josephson equations to predict the current-voltage (I-V) characteristics of the Josephson

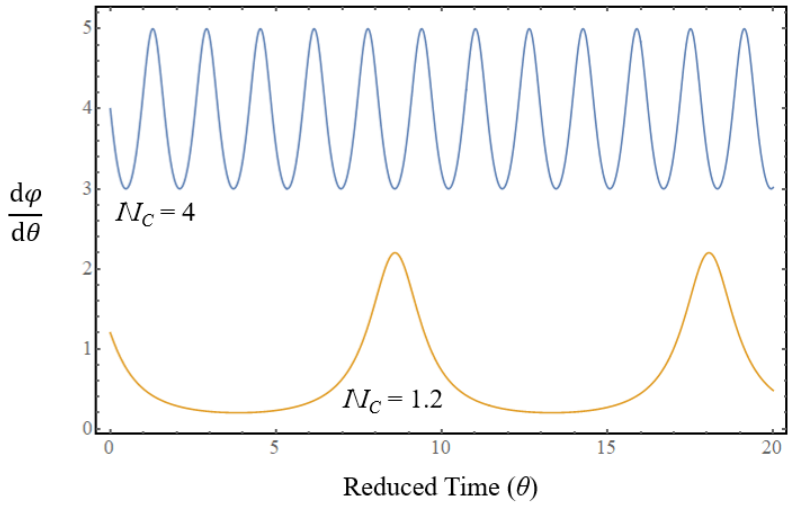

Figure 2.8: Numerically evaluated time varying Josephson phase for $I/I_C = 1.2$ (orange) and 4 (blue).

junction. I-V characteristics are a common experimental measurement for determining junction parameters.

For the overdamped case ($\beta_C \ll 1$) the curve is non-hysteretic and Eq. 2.40 becomes a trivial first order differential equation

$$V = \begin{cases} 0 & I < I_C \\ I_C R\sqrt{(\frac{I}{I_C})^2 - 1} & I > I_C \end{cases} \tag{2.43}$$

In the overdamped case, the capacitance in the junction may be neglected, which is why this expresion is often referred as the resitively shunted junction (RSJ) model (see Fig. 2.9). Note that the product of I_C and R is an important parameter that characterizes the quality of the junction. $I_C R$ of a Josephson junction is related to the superconducting order parameter by the Ambegaoker-Baratoff relation and can yield an estimate for the quality of the junction by comparing to the fraction of the superconducting bulk electrode's energy gap value [45].

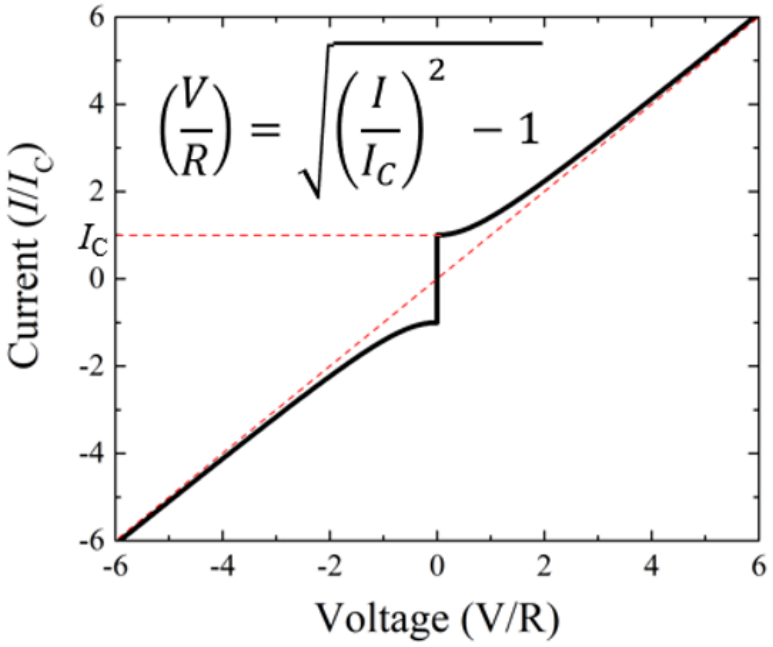

Figure 2.9: Resistively shunted junction model (β_C=0) current-voltage characteristic.

Whereas, for large β_C ($\beta_C \gg 1$), the I-V curve can be hysteretic and is termed an underdamped junction. In the arbitrary β_C case, numerical integration can be used to calculate the current-voltage characteristics, which is plotted in Fig. 2.10.

The RSCJ model can be extended to include effects from thermal noise and was first shown by Ambegaokar and Halperin [51]. In order to consider thermal effects they consider a Fokker-Plank model for the Brownian motion of the charge particles. To simplify the required numerical integration they consider a Josephson junction in the overdamped limit such that the Fokker-Planck equation reduces to the Smoluchowski equation. The general expression they derived for arbitrary noise voltage is as follows [3]

[3]Note there is a typographical error in the original paper that I correct here. The integrands of the last integration term of Eq. 9 should run from θ to 2π. Also note that I switched θ in the paper to ψ here for consistency within this dissertation.

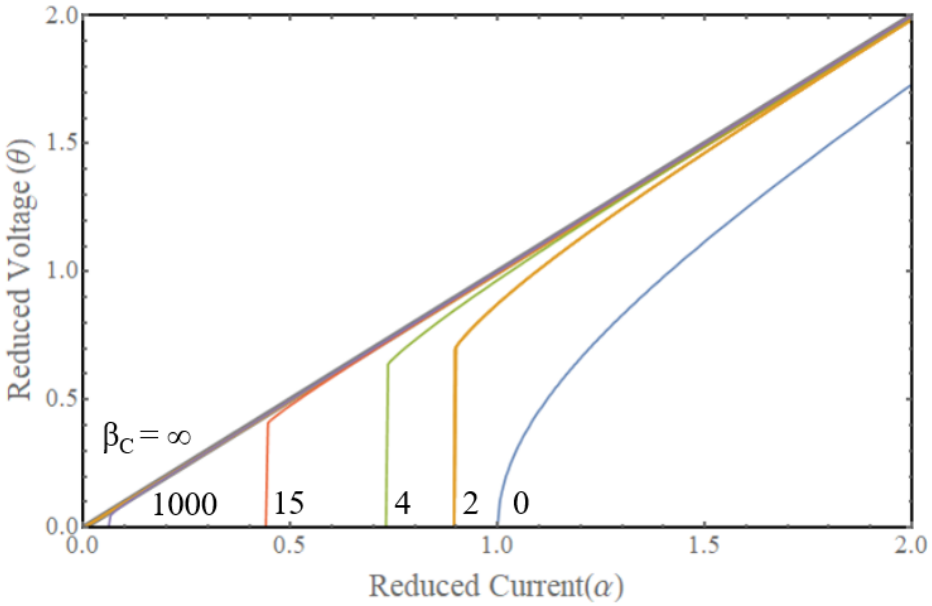

Figure 2.10: Resistively and capacitively shunted junction model for arbitrary B_C voltage-current characteristics.

$$\frac{V}{I_C R} = \frac{4\pi}{\gamma}\left\{(e^{\pi\gamma x}-1)^{-1}\left[\int_0^{2\pi} d\varphi f(\varphi)\right]\left[\int_0^{2\pi} d\varphi' \frac{1}{f(\varphi')}\right] + \int_0^{2\pi}\int_{\varphi}^{2\pi} d\varphi' \frac{f(\varphi)}{f(\varphi')}\right\}^{-1} \quad (2.44)$$

with the following definitions

$$\gamma = \frac{\hbar I_C(T)}{e k_B T}$$

$$x = I/I_C(T)$$

$$U = -\frac{1}{2}\gamma T(x\varphi + \cos\varphi)$$

$$f(\varphi) = e^{(-U(\varphi)/T)}$$

where γ is the ratio of the coupling energy to the thermal energy. Note in the limit where $\gamma \to \infty$ and $I < I_C$ Eq. 2.44 resolves the expected Eq. 2.43. From Fig. 2.11 we can see the effects of thermal noise on the I-V characteristics. It results in a rounding about the I_C

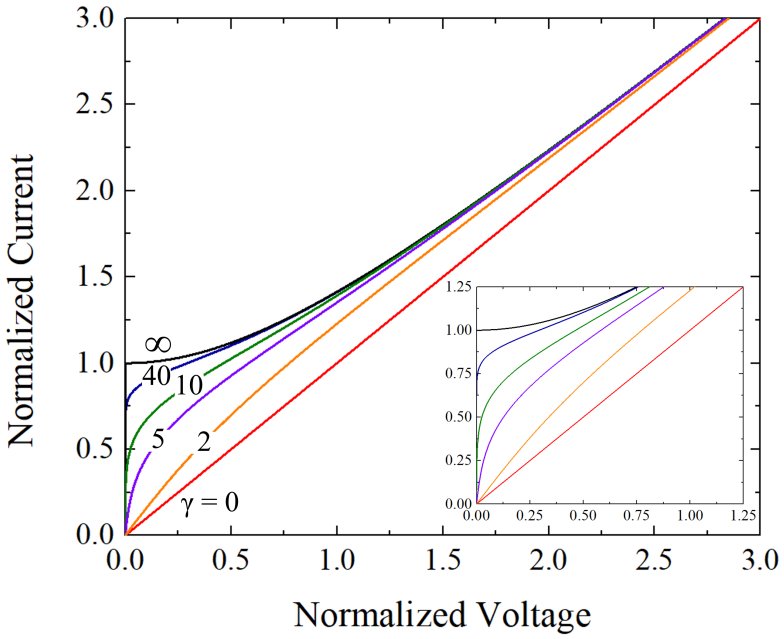

Figure 2.11: Current-voltage characteristics of a Josephson junction, including thermal noise, for various effective noise voltages. Inset is a zoom in on the region near the transition from the supercurrent to voltage state.

caused by thermally activated phase slippage. This noise obscures the resolution necessary to determine I_C, resulting in needing a higher I_C at high temperatures to accurately resolve an I-V curve. For example, at liquid nitrogen temperatures it becomes prohibitively noisy to properly measure a Josephson junction with $I_C < 10\ \mu A$.

2.5.2 Magnetic Flux Effects

So far we examined Josephson junctions in the "short" regime which is defined by the case where the phase is constant inside of the Josephson barrier with zero applied magnetic flux. We will consider a more general case in which magnetic flux threads the junction. Fig. 2.12 indicates the junction geometry with a corresponding coordinate system.

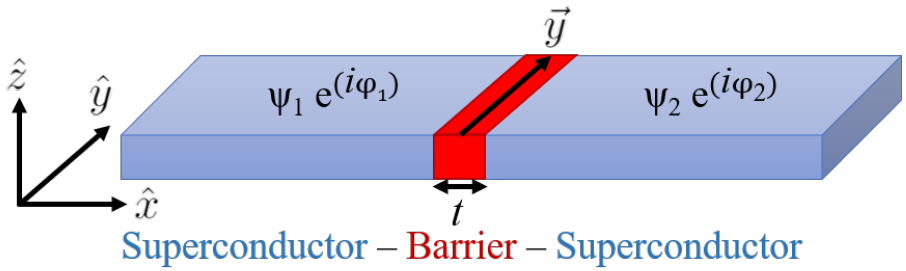

Figure 2.12: Representation of planar Josephson junction geometry with coordinate system indicated.

l is the width of the junction along the $\hat{y}$-direction. For this geometry the junction will be sensitive to a magnetic field component applied in the $\hat{z}$ direction. The gauge invariant phase difference between two points is given by

$$\nabla\varphi = \frac{2e}{\hbar}\left(\frac{m}{2e\rho}\vec{J}_s + \vec{A}\right) \tag{2.45}$$

where m is effective charge carrier mass, $\vec{J}_s$ is the supercurrent density and $\vec{A}$ is the magnetic vector potential. We can solve for the phase inside the Josephson barrier by choosing a clever contour to integrate along where the $\vec{J}_s$ terms cancel.

$$\Delta\varphi = \frac{2\pi}{\Phi_0}\oint \vec{A}\cdot d\vec{c} \tag{2.46}$$

Additionally, magnetic flux only penetrates inside the junction barrier and a length scale equal to the London penetration depth into the superconducting bulk electrodes. So if we consider a surface integral of the magnetic field component applied into the barrier (B)

$$\varphi = \frac{2\pi}{\Phi_0}(2\lambda_L + t)By + \varphi_0 \tag{2.47}$$

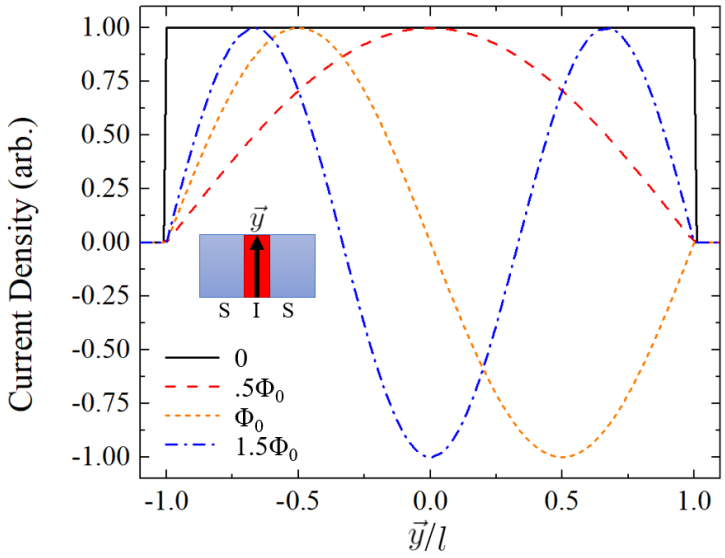

Figure 2.13: The effect of magnetic flux on current inside a Josephson junction (along $\hat{y}$). The phase shifts caused by increasing magnetic flux results in the reduction of maximum supercurrent.

where t is the barrier thickness and y is the spatial component along the junction barrier. This phase can be input into the DC Josephson equation

$$\vec{J}_s = \vec{J_C} \sin\left(\frac{2\pi}{\Phi_0}(2\lambda_L + t)By + \varphi_0\right) \tag{2.48}$$

The preceding equation demonstrates that an applied magnetic flux will spatially vary the current density in the barrier. Fig. 2.13 plots current in a sandwich-style Josephson junction for various magnetic flux strengths. This has the effect of modulating the total supercurrent in the junction. If we combine this expression with Maxwell's expression for the $\vec{\nabla} \times \vec{B}$ we can find that

$$\frac{\partial^2 \varphi}{\partial y^2} = \frac{1}{\lambda_J^2} \sin\varphi; \qquad \lambda_J = \left(\frac{\hbar}{2e\mu_0(2\lambda_L + t)J_c}\right)^{(1/2)} \tag{2.49}$$

where λ_J is defined as the length scale to which the current is screened inside a Josephson junction by the Meissner effect. It is referred to as the "Josephson penetration depth."

We can derive an expression for $I_C(\Phi)$ by integrating Eq. 2.48 over the barrier area. Additionally, to increase generality we will allow $\vec{J}_s$ to vary along same dimension of the Josephson barrier as the phase (along y-axis)

$$I(k,\varphi_0) = \int_{-l/2}^{l/2} dy \vec{J}_s(y) \sin(ky + \varphi_0); \qquad k = \frac{2\pi(2\lambda_L + t)}{\Phi_0} B \tag{2.50}$$

which is equivalent to

$$I(k,\varphi_0) = \mathrm{Im}\left\{ e^{i\varphi_0} \int_{-l/2}^{l/2} dy \vec{J}_s(y) e^{iky} \right\} \tag{2.51}$$

If we maximize with respect to φ_0 and extend the integrands out to all space, taking $\vec{J}_s = 0$ outside the Josephson barrier we arrive at the convenient form

$$I(k) = \left| \int_{-\infty}^{\infty} dy \vec{J}_s(y) e^{iky} \right| \tag{2.52}$$

which tells us that the $I_C(\Phi)$ is given by the modulus of the Fourier transform of the supercurrent density inside the Josephson barrier [52].

If we examine the simple case where the tunneling current is uniformly distributed inside the junction, generally with junction dimensions $\ll \lambda_J$, we find that

$$I_C\left(\frac{\Phi}{\Phi_0}\right) = I_C(0) \left| \frac{\sin \pi \frac{\Phi}{\Phi_0}}{\pi \frac{\Phi}{\Phi_0}} \right| \tag{2.53}$$

This is the Fraunhofer equation, plotted in Fig. 2.14, suggesting that phase interference in Josephson junctions is analogous to optical single slit diffraction. Note that the interference pattern has a periodicity of a magnetic flux quantum within the junction. Measurement of the I_C modulation is a common test for the Josephson effect.

Generally, Eq. 2.53 is a good approximation for small Josephson junctions of the sandwich-stlye geometry. However, for Josephson junctions with dimensions $\gg \lambda_J$, or the so

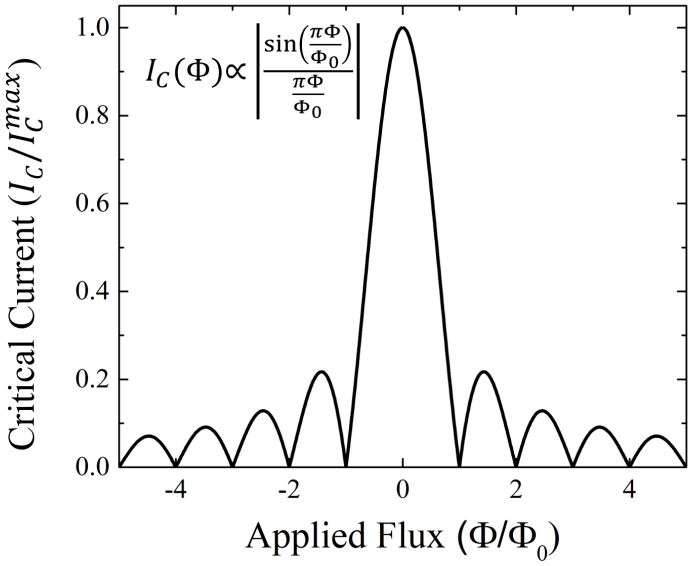

Figure 2.14: Critical current interference for applied magnetic flux in a small Josephson junction in a sandwich style geometry.

called "long" regime, the assumption that the current density is constant within the junction barrier is not valid and the $I_C(\Phi)$ tends to deviate from the Fraunhofer diffraction pattern [53]. Moreover, Josephson junctions with differing geometry may also cause a deviation in junction current in the Josephson barrier.

It is pertinent to the topics of this dissertation to give special attention to the thin-film planar Josephson junction geometry. Several theoretical and experimental efforts have treated this particular geometry [54, 55]. Junctions of this variety feature a flux focusing effect where the magnetic flux is expelled from the adjacent bulk superconducting electrodes and it is focused into the Josephson barrier. Using arguments from the London treatment of superconductivity, it is concluded that the I_C modulation periodicity in applied magnetic

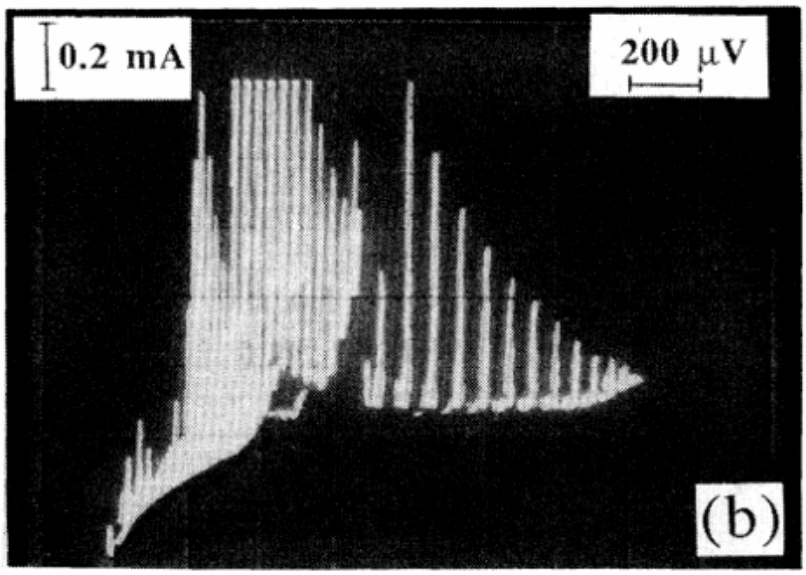

Figure 2.15: Josephson junction current-voltage characteristic while varying magnetic bias depicting Fiske modes. Reprinted figure with permission from [56] copyright 1993 by the American Physical Society.

flux scales as the following

$$\Delta B \simeq \Phi_0 \frac{1.84}{l^2} \tag{2.54}$$

recalling that l is the dimension of the Josephson junction along the $\hat{y}$-direction as given by Fig. 2.12. Consequently, in general planar junctions are more sensitive to applied magnetic fields comparing to the sandwich-style junctions.

2.5.3 Fiske Modes

Josephson junctions were shown to feature resonant modes, termed "Fiske modes," excited by the AC Josephson effect [57]. The junction itself acts as an open-ended resonator with the current density waves interacting with the electromagnetic fields resulting in step-like voltage structures. Since Fiske modes treat the junction itself as the resonator cavity the

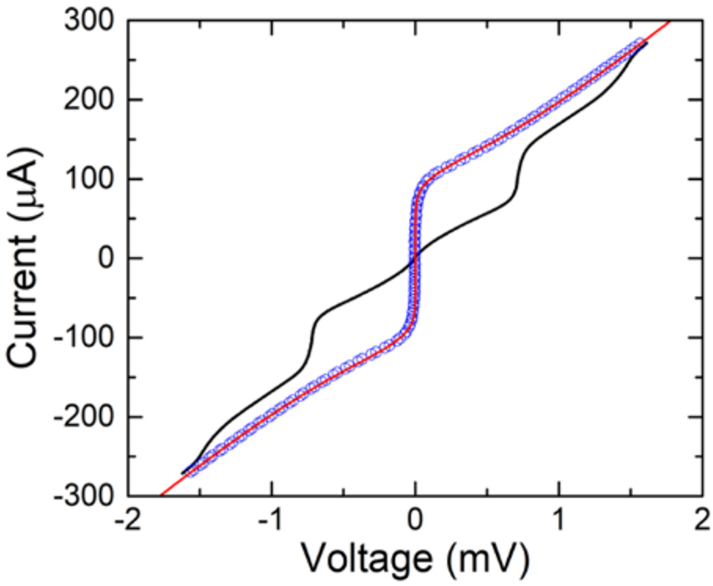

Figure 2.16: Comparison between current-voltage characteristics of a non-AC (blue circles) and AC biased (black line) series array of 20 Josephson junctions depicting quantized Shapiro steps. The array was biased with 17 GHz.

nature and appearance of these peaks depends explicitly on the geometry of the barrier itself. Furthermore, these Fiske modes depend explicitly on the magnitude of the applied flux threading the junction. The observation of the these resonant modes was strong evidence for the Josephson effect. Fig 2.15 yields current-voltage characteristics for several Fiske modes by varying the magnetic bias.

2.5.4 AC Biased Josephson Junction

Another common observable response of the Josephson effect is quantized steps that occur in the supercurrent while the junction is simultaneously DC and AC biased. See Fig. 2.16 for an example measurement of these effects. These steps occur at precise values

$$V = \frac{nhf}{2e} \tag{2.55}$$

where f is the frequency of AC bias. If we consider a generalized $V(t)$ that is applied to the junction and we combine the two Josephson equations we arrive at

$$I(t) = I_C \sin\left(\int_0^t dt' \frac{2e}{\hbar} V(t') + \varphi_0\right) \tag{2.56}$$

For a V(t) that is the sum of a constant voltage and an AC voltage with frequency (ω_s), the preceding equation becomes

$$I(t) = I_C \sum_{n=0}^{\infty} (-1)^n J_n \frac{2eV_{AC}}{h\omega_s} \sin[(\omega_J - n\omega_s)t + \varphi_0] \tag{2.57}$$

where J_n is the Bessel function of the first kind, and $\omega_J = 2eV_{DC}/\hbar$ is the constant varying Josephson phase due to a DC applied voltage. Not to be confused with Fiske modes, this effect creates quantized steps in the I-V characteristics coinciding with Eq. 2.55. Unlike Fiske modes, these steps are independent of junction geometry making them ideal for defining technical standards [10]. These steps were first predicted by Josephson and are now referred to as "Shapiro steps" after the physicist who first observed these effects [58].

2.6 Superconducting Quantum Interference Devices

Superconducting quantum interference results when we consider superconducting flux quantization with the Josephson effect. Superconducting quantum interference devices (SQUIDs) typically consist of two Josephson junctions connected in parallel in a superconducting loop, referred as a "DC SQUID." However, it is also possible to observe this interference behavior in a system that contains a single Josephson junction coupled to a superconducting loop, termed as "RF SQUIDs." These devices are highly sensitive to application of magnetic flux, and therefore, are commonly used as magnetometers. In general,

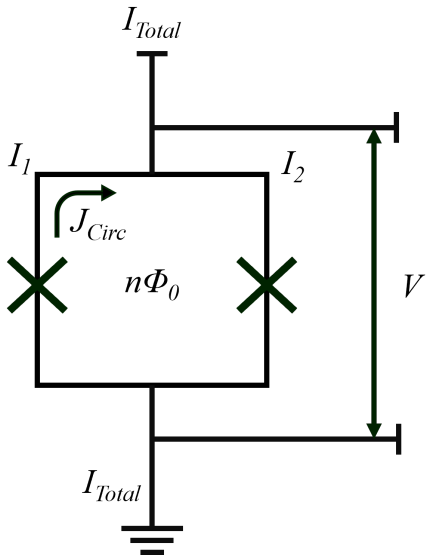

Figure 2.17: Schematic representation of a DC superconducting quantum interference device (SQUID).

DC SQUIDs are more commonly used because they feature higher sensitivities.

We will examine the DC SQUID case in more detail (see Fig. 2.17) Combining Kirchhoff's law, superconducting flux quantization and the Josephson equations we can write out the DC SQUID equations. Starting by determining the total current in the loop, with circulating current (J_{Circ})

$$I_{Total} = (I_1 - J_{Circ}) + (I_2 + J_{Circ}) = 2I_C \cos\left(\frac{\varphi_1 - \varphi_2}{2}\right) \sin\left(\frac{\varphi_1 + \varphi_2}{2}\right) \tag{2.58}$$

Now we can consider the gauge invariant phase

$$\varphi_2 - \varphi_1 = 2\pi n + \frac{2e}{\hbar} \oint \vec{A} \cdot d\vec{c} + \text{Constant} \times \oint \vec{J_{Circ}} \cdot d\vec{c} \tag{2.59}$$

we choose a contour where $J_{Circ} = 0$ and note that the integral of the magnetic potential is just the magnetic flux in the loop

$$\varphi_2 - \varphi_1 = 2\pi n + \frac{2\pi\Phi}{\Phi_0} \tag{2.60}$$

and Eq. 2.58 becomes

$$I_{Total} = 2I_C \cos\left(\frac{2\pi\Phi}{\Phi_0}\right) \sin\left(\varphi_1 + \frac{2\pi\Phi}{\Phi_0}\right) \tag{2.61}$$

This can be generalized to include circulating current by noticing that the total flux in the loop is given by $\Phi = \Phi_{ext} + LJ_{Circ}$. Consequently, we can write down total flux in loop in terms of the total current

$$\Phi = \Phi_{ext} + \frac{LI_C}{2} \cos\left(\frac{2\pi\Phi}{\Phi_0}\right) \sin\left(\varphi_1 + \frac{2\pi\Phi}{\Phi_0}\right) \tag{2.62}$$

Eq. 2.61 and 2.62 show generally that in the zero voltage state and for a given external flux we can maximize the total current to determine maximum supercurrent of the SQUID. Often SQUIDs are characterized by a normalized parameter defined as $\beta_L = 2LI_C/\Phi_0$. If we examine the trivial case where $\beta_L = 0$ and maximize the current in the SQUID we find

$$I_C^{\beta_L=0} = 2I_C \left|\cos\left(\frac{\pi\Phi_{ext}}{\Phi_0}\right)\right| \tag{2.63}$$

which is to say that the SQUID I_C has an oscillating response where the period is given by the magnetic flux quantum. This interference behavior is also analogous to an optical physics experiment. In the case of SQUID interference, it parallels Thomas Young's double slit experiment.

In practice, DC SQUIDs are amongst the most sensitive detectors of magnetic flux [11, 12]. As demonstrated in Fig. 2.18 they are typically operated in the voltage state, by current biasing the SQUID just above the I_C causing the phase to oscillate as given by Josephson's second equation. Slight changes in applied magnetic flux, even fractions of the magnetic flux quantum, cause a modulation of the voltage response that can be measured.

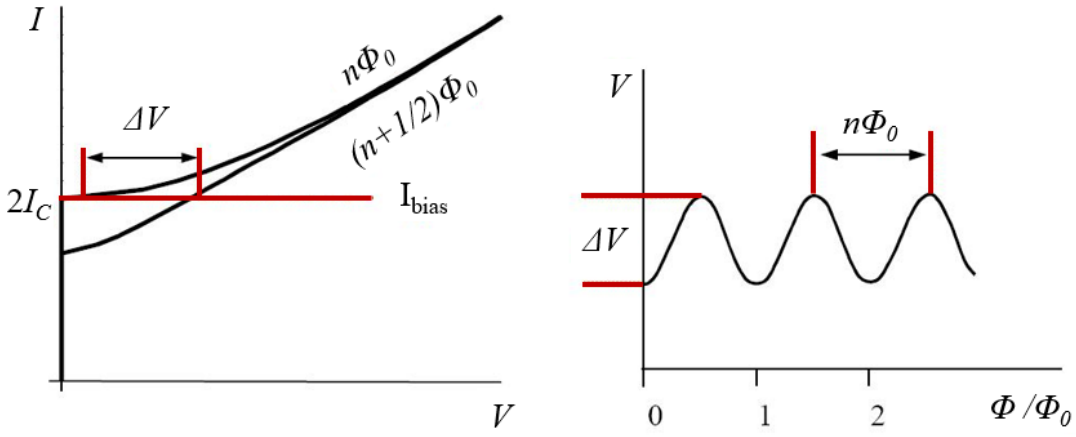

Figure 2.18: Current-voltage and voltage-magnetic flux characteristics that indicate the measurement scheme for SQUID.

2.7 Arrays of Josephson Junctions

Ultimately, despite the the many applications of the Josephson effect, the circuits themselves are difficult to measure with responses just above the noise floor. As an example, the sensitivity of SQUIDs are limited by white noise intrinsic to the Josephson junctions themselves. It is often desired in practical implementation to have devices with large, easily detectable responses. Towards this end, arrays of Josephson junctions and SQUIDs are highly investigated [59, 60, 61, 62]. The voltage response of the Josephson devices add linearly with N devices in series. Moreover, it is predicted that the noise power scales like $\sqrt{N}$, yielding a scaling of the signal-to-noise ratio to be $1/\sqrt{N}$.

We already demonstrated that Josephson junctions are transducers between voltage and frequency in Sec. 2.5.4. Ideal standards for units of measurement are often transduced to frequency due to the ease of measurement in the frequency domain. It is for that reason that series arrays of Josephson junctions are the contemporary international stan-

dard for defining the volt [10]. A single Josephson junction produces a voltage of the first Shapiro step at $\sim$10 μV, which is difficult in practice to consistently measure. Yet, that response is scaled up by three orders of magnitude if 1000 Josephson junctions were to be arrayed in series. Responses in the $\sim$mV range are much more suitable to widely available and easily operated semiconductor electronics.

Furthermore, it is also often desirable to engineer the voltage response to Josephson phase interference by applied magnetic flux. The SQUID response is highly nonlinear and symmetric regarding direction of applied magnetic flux. Significant efforts have been made to engineer this voltage response by making parallel arrays of Josephson junctions. An example based on this philosophy is the superconducting quantum inteference filter (SQIF) that arrays several SQUIDs in parallel, series or in a 2D array each with different loop dimensions in an attempt to replicate unconventional grating structures in optical physics [63]. When loop dimensions are carefully chosen there will be a sharp peak at zero applied magnetic flux bias, making the SQIF an absolute detector of magnetic flux, unlike the SQUID, which is only sensitive to relative changes.

While the implementation of Josephson arrays is promising based on the success of the Josephson voltage standard, design of arrays of Josephson junctions must be carefully considered in order to meet the technical design requirements for the specific application.

2.8 Unconventional Superconductors

The success of BCS theory is its ability to predict the behavior of intrinsic parameters of materials while in the superconductive state. However, there have been some

superconductors that deviate away from the predictions of this theory and are called "unconventional superconductors." The nature of many of these unconventional superconductors remains a contested subject and is one of the greatest ongoing questions in physics. Heavy fermion materials were one of the first unconventional superconductors to be reported on [64]. It was believed that the symmetry of the underlying attractive potential was of anisotropic state symmetry. Additionally, some experimental studies have suggested the occurrence of spin triplet state superconductivity in organic and ferromagnetic materials [65, 66]. There is also some evidence to suggest unconventional pairing mechanisms in materials such as Sr_2RuO_4 [67]. However, the most prominent class of superconductor thought to be unconventional is the cuprate materials, boasting observations of the highest T_C at ambient pressure at the time of writing [68]. It is widely accepted that cuprates also feature anisotropic pairing symmetry. It is important to remark that nothing in BCS theory would suggest against the possibility of superconductivity occurring at high temperatures. As an example, the material MgB_2 is a conventional superconductor featuring a relatively high T_C at 39 K. However, there is a concern that superconductors with high T_C lack a carrier density high enough to form a superconducting condensate by consideration of conventional theory.

2.8.1 Cuprates

In superconductivity, cuprate oxides are an important class of material, referred as such due to their inclusion of planes in the lattice of copper and oxygen. The prevalence of the observation of superconductivity in cuprate materials and a careful series of transport measurements of both the normal and superconducting state have strongly suggested the

CuO planes to be the site of superconductivity [69, 70].

It should be noted that cuprate superconductors commonly exhibit high values for their energy gaps. Recall from Sec. 2.2.3, that the dimensionless quantity for BCS is $\Delta_{BCS}(0)/k_BT_C \approx 1.76$. This quantity predicts a Δ of $\sim$12 meV for superconductors with a T_C $\sim$80 K. Additionally, attempts at estimating the carrier density have been made using commonly cited values for the unit lattice constants and the coherence values. These estimates state that cuprates have a discrepancy in the charge carrier density in comparison to BCS theory [71]. Some argue that this is proof that the nature of cuprate superconductivity is two dimensional and restricted to the CuO planes, and should rather be estimated using that assumption.

$\mathbf{YB_2C_3O_{7-\delta}}$

One of the first cuprates to feature a T_C greater than the temperature of liquid nitrogen was $YB_2C_3O_{7-\delta}$ (YBCO) [72]. This material became a widely researched material due to its relatively facile processing, stability, high supercurrent density and high T_C. YBCO is a othorhombic perovskite that has CuO chains running in the b-axis and CuO planes in the a-b plane. The unit cell is visualized in Fig. 2.19 with both the CuO chains and planes indicated by overlay. Commonly cited lattice parameters are $a = 3.82$, $b = 3.89$, and $c = 11.68$ Å [73]. It has highly anisotropic transport properties in both the normal and superconducting state [69, 70]. It features a very small coherence length on the nanometer scale [74]. Furthermore, due to the complex lattice structure, YBCO is prone to common crystal defects, such as, grain boundaries and twinned boundaries [75].

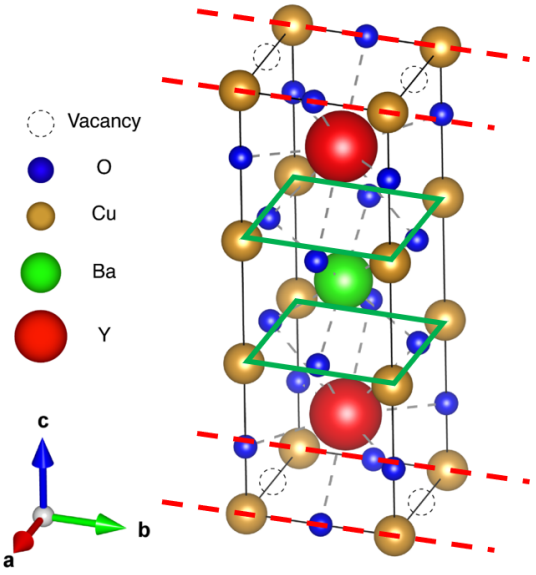

Figure 2.19: Depiction of the $YB_2C_3O_{7-\delta}$ unit cell. Note the orthorhombic nature of the crystal where $a \neq b \neq c$. The symmetry of this lattice is a subgroup of C_4v. The red dotted lines indicate CuO chains and the green solid lines indicate CuO planes.

There is significant evidence for unconventional pairing symmetry in cuprates to be discussed in detail in Sec. 2.8.2. As the subject of this dissertation's investigation into the pairing symmetry of cuprate materials, I will use YBCO to be an example of group theory analysis that may yield information on the underlying nature of the superconducting potential [76]. In order to simplify the complex nature of unconventional superconductivity, we will rely on group theory to make progress. The goal of group theory is to find the representations of the group, test and subsequently deconstruct them to their irreducible representation, and to use that information to form the invariant subspaces that represent the system. In general it is difficult to solve the exact eigenvalue and eigenfunction problems in quantum mechanics. Therefore, we can utilize group theory to simplify the eigenvalue problems and classify the eigenfunctions by the irreducible representations of their symme-

try groups related to the reduced Hamiltionian (Eq. 2.3), which models the system behavior. Note that the kinetic term of the reduced Hamiltonian is invariant to transformations, and consequently the transformation properties of the reduced Hamiltonian are decided by its other term, the potential energy. With the symmetry group of a Hamiltonian, we can attempt to form the invariant subspaces with respect to its irreducible representations, which may diagonalize the Hamiltonian without ever explicitly solving the eigenvalue problem.

To begin treatment of our system using the methods of group theory, we must determine the symmetry group of the materials lattice. A group can be identified by listing the group characters of the various representations in what is referred to as a character table. A group character is the trace of the irreducible representation. In cuprate materials, like YBCO, it is thought that much of the "action" of superconductivity takes place within the copper oxide planes due to the prevalence of the observation of superconductivity in these materials with this common structure. Therefore we consider the symmetries of a planar square lattice. We will restrict ourselves to singlet states because of the Knight shift experiments [77, 78] performed on cuprate materials provide strong evidence for that case. Therefore, the crystal point group is as follows: [79]

- $\pi/2$ rotation about $\langle 001 \rangle$ $R_{\pi/2}$
- Reflection about $\langle 100 \rangle$ $I_{x/y}$
- Reflection about $\langle 110 \rangle$ I_{axis}

Since the reflection groups are not independent, we only consider I_{axis}. By inspection it is obvious that the symmetries of a planar square lattice are characterized by four cyclic rotations of angle $\pi/2$ around the axis. Furthermore, there is a symmetry of reflection that

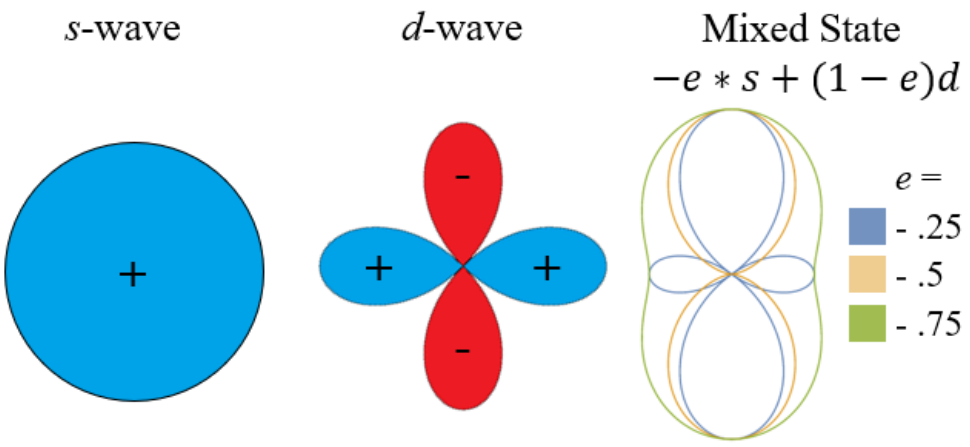

Figure 2.20: Visual representations of s, d, and admixture $-es + (1-e)d$ state symmetries for $e = .25$, $.5$ and $.75$.

C_{4v} Character Point Group				
Informal Name	Irreducible Representation	$R_{\pi/2}$	I_{axis}	Orbital Expression
s^+	A_{1g}	$+1$	$+1$	constant
s^-	A_{2g}	$+1$	-1	$xy(x^2-y^2)$
$d_{x^2-y^2}$	B_{1g}	-1	$+1$	x^2-y^2
d_{xy}	B_{2g}	-1	-1	xy

Table 2.1: Character point group of C_{4v} which reflects the symmetries of a planar square lattice.

is about a plane that contains that axis. The character table for this point group (C_{4v}) is listed in Table 2.1. Note that hereafter we will refer to the type of symmetry by referring to the angular momentum orbital quantum numbers, we will term s-wave for isotropic angular gap dependence and d-wave for anisotropic with sign changes in the angular gap dependence.

Fig. 2.19 gives a representation of the unit cell of YBCO, and it is evident that YBCO is a subgroup of the C_{4v} point group due to its nearly square CuO planar lattice. If we extend this geometry to the orthorhombic case, of practical application to YBCO, the loss in

symmetry in $I_{x/y}$ results in the possibility of mixed states. However, for such a mixed state to exist there must be a second transition (T_{C2}) where $T_{C2} < T_C$. Despite investigations in a wide range of temperatures from T_C to ≈ 10 mK no such second transition has been reported. These symmetries and their mixed states are visually represented in Fig. 2.20.

$\mathbf{Bi_2Sr_2CaCu_2O_{8+\delta}}$

Another prevalent cuprate superconductor is $Bi_2Sr_2CaCu_2O_{8+\delta}$ (BSCCO) due to some of its unique properties [31]. BSCCO forms a crystal lattice of a tetragonal nature with $a = b \approx 5.4$ and $c = 30.7$ Å[80]. Like YBCO, BSCCO generally features a T_C above liquid nitrogen temperatures and highly anisotropic normal and superconducting state transport properties. Especially along the c-axis, transport properties are highly resistive due to the weakly bonded BiO layers. These layers are insulating and feature an intrinsic Josephson effect [81]. Due to internal Van der Waals bonding of BSCCO layers, it is possible to exfoliate thin single crystal films from bulk samples. This property makes it a common material studied in the fabrication of Van der Waals heterostructures. It is also a desirable research material since exfoliated films do not suffer from the same defects common in the deposition of complex crystals. It is also generally thought of featuring d-wave pairing symmetry.

2.8.2 Historical Experiments of Cuprate Pairing Symmetry

To date many articles have reported on experiments devised to determine the pairing symmetry in cuprate superconductors which can be roughly divided into two categories: investigating sign changes in the energy gap and quantum phase interference [82, 79]. An

example of an experiment of the former category involves the measurement of temperature dependence of the penetration depth. s-wave predicted temperature dependence of the penetration depth is exponential, conversely d-wave is predicted to be a power law dependence where the exponent is related to the number of nodes. Early measurements of this kind were consistent with BCS [83, 84]; however, with the development of increasingly sophisticated measurement techniques it was suggested that the results are more consistent with unconventional pairing [85, 86, 87, 88]. Each of these four cited studies determined the penetration depth by measuring microwave cavity parameters. Despite the similarity in the measurement schemes, the dependencies reported were exponential, quadratic, linear, and two node dependent respectively. Additionally other methods were developed to determine the penetration depth, which included measurements of magnetization [83] and spin-muon-rotation [89] that also give conflicting reports. Even more curiously, is that measurements made on NdBCO of the temperature dependence of the penetration depth were consistent with s-wave [90].

Another attempt to determine the pairing symmetry was made through techniques involving angle resolved photoemission (ARPES) [91, 92]. ARPES measurements on YBCO failed to produce satisfying results, so that much of these types of experiments are mostly restricted to BSCCO. Similar to the penetration depth experiments, conflicting reports were presented [93]. Moreover, ARPES is limited in resolution and was unable to rule out the possibility of mixture states. The conclusions drawn from ARPES measurements are model dependent and the analysis remains controversial [94].

Any experiment that could probe the pairing symmetry was attempted to try to

illuminate the issue. Consequently, scattering experiments were also conducted. Neutron experiments that were sensitive to the spin susceptibility, which was related to the energy gap, were performed [95, 96, 97]. Neutron scattering suffered from low resolution and the existence of a gap above T_C suggesting a confusion between the magnetic and the superconducting gaps. Finally, Raman scattering experiments were performed which indicated the presence of electron-hole pair excitations below the energy gap, which is evidence against isotropic pairing symmetry [98, 99].

Taking collectively the results from experiments involving investigations regarding sign changes in the energy gap, the scientific community favors the evidence supporting unconventional pairing. However, controversy persists and certain elements challenge the conclusions from an analytic standing. The conclusions of the preceding cited experiments are complexly dependent on nuanced models of the system. Alternate interpretations that can self-consistently conclude between both s and d-wave have been put forward which casts doubt on the reliability of these types of experiments [100].

The other case, quantum phase interference, considers Josephson junctions with one or more superconducting electrodes with unconventional pairing. The tunneling terms of the Hamiltonian are constrained by symmetry arguments. Broadly speaking the phase sensitive experiments may be organized in three categories with the first investigating tunneling between a conventional superconductor and an unconventional one [101, 102, 103]. Symmetry constraints would forbid c-axis tunneling from a conventional pairing superconductor to a d-wave superconductor. Yet, Josephson tunneling was observed between YBCO and Pb. Critics of this result argue that the tunneling is occuring at jagged protrusions

at the interface however, reference [101] found no relation between surface morphology and I_C making tunneling along these channels unlikely. Moreover, this result only can support the presence of an s-wave component and cannot limit the amount of mixing with d-wave components.

The second quantum phase sensitive category deals with SQUID circuits comprised of a conventional superconductor and an unconventional one [104, 105, 106]. The observation of fractional flux values as well as an I_C minimum at zero magnetic field supports the d-wave pairing symmetry. Moreover, the results from reference [106] restrict complex mixing of s and d to below 5%. Finally, the last category measures the fractional flux effects but in unconventional superconducting circuits with tunneling into differing crystal orientations [107, 108, 109]. The criticism levied at these types of experiments is that the observed effects can be attributed to flux trapping [110]. Recent measurements of this kind depend on a scanning SQUID microscope measurement in order to account for all magnetic flux present in the system [111]. However, there is another criticism which argues that the observed fractional flux effects are due to uneven critical currents in the weak-links in the loops.

The controversy regarding unconventional superconducting order parameter symmetry remains a problem in contemporary physics and is still currently being investigated. Recently Caroli-de Gennes-Matricon vortex states were observed in Abrikosov vortices [112]. These localized states were predicted to occur from BCS in type-II superconductors, which are superconductors that allow penetration of magnetic fields into the bulk materials as normal metal cores with a vortex of current that sustains a magnetic flux quanta. Addi-

tionally, in recent years novel investigations are still being devised to address the unresolved mystery [113, 114]

To summarize the implications of the culmination of the data reported thus far, the evidence is technically not conflicting if one considers a mixture of both s and d-wave pairing symmetry. However, this is limited to a complex admixture of less than 5%. Although, there remain many caveats to this statement because of the complex interpretations of the data and unaccounted experimental effects. None of the discussed experiments can provide a direct measurement of the conduction band that determines the energy gap, generally thought to be the most accurate measurement scheme for determining the pairing symmetry. While attempts have been made to perform these types of tunneling experiments, technical difficulties of performing this type of experiment in cuprate materials has limited the scope of information that may be determined.

A common tool for the characterization of localized densities of states is a scanning tunneling microscope (STM). Typically, these instruments can tunnel quasi-particles from a metal or conventional superconducting tip (such as lead or tungsten) into a target material using vacuum space as a barrier. In cuprate materials, several STM studies have been performed [115, 116, 117, 113]. Additionally, tunneling Josephson junctions have been fabricated in cuprates by tunneling Pb into YBCO [118, 119]. These methods were able to characterize the densities of states in cuprate materials for the first time. However, these techniques were limited technically from producing convincing claims on the pairing symmetry in cuprate materials. Firstly, STMs are currently limited to metal or conventional superconducting tips so that the tunneling junctions do not consist of homogeneous material,

which may obscure features in the differential conductance. Additionaly, these studies are mostly limited to tunneling in the c-axis plane. It was necessary to advance techniques to a create a technology that allowed for transport in the a-b plane arbitrarily and with clean homogeneous superconducting-insulating-superconducting junctions to make progress. Such a technique was developed and the first in-plane measurements of the YBCO density of states were reported [120]. This technique inspires a new experiment to probe in-plane the dependence of the cuprate superconducting order parameter.

Chapter 3

Experimental Techniques

This chapter will discuss techniques and methods for the rapid and iterative workflow processes developed for fabrication and characterization of high-T_C superconducting devices. This research orientated system was developed particularly to be able to take concepts and realize them within a matter of days if not hours. The Oxide Nano-Electronics Laboratory (ONELAB) at University of California, Riverside is where the work contained herein was primarily conducted. ONELAB is equipped for performing all aspects of the the necessary experimental techniques the following sections discuss.

Historically, the complexity of cuprate superconductors has stymied scientific and engineering progress of high-T_C superconducting devices. Due to the industrial success of silicon-based computing, the most sophisticated fabrication techniques are working with complementary metal-oxide-semiconductor (CMOS) based systems. Some of these techniques may be adapted for conventional superconductors, such as aluminum and niobium, for which complicated multi-layer fabrication is continuously being developed both for aca-

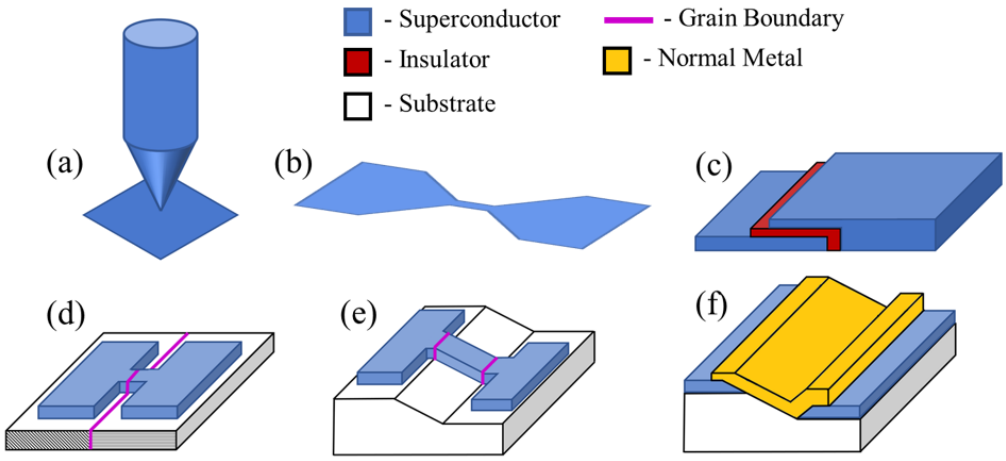

Figure 3.1: Illustrations of various geometries for Josephson junctions. (a) Point contact, (b) Dayem bridge, (c) tunnel junction, (d) bicrystal junction, (e) step-edge grain boundary, and (f) step-edge SNS junction.

demic and commercial application [121, 122]. YBCO and other cuprates feature complex unit cell lattices which makes multi-layer devices complicated due to lattice mismatch amongst the different layers. Even in single layer deposition, reduction of defects in the lattice remains a research challenge. Therefore, it became necessary to develop new fabrication techniques suited to these cuprate materials.

Several techniques have been demonstrated as a method to fabricate the weak-links necessary for Josephson barriers in superconducting materials. These barriers can exhibit metal or insulating-like behavior. Some low-T_C devices use point contacts as illustrated in Fig. 3.1a. Weak-links may also be formed by constrictions in the geometry like a thin bridge. Fig. 3.1b depicts an example of these constrictions that are referred to as a "Dayem bridge." Low-T_C Josephson junctions most often take the form of a multi-layer tunnel junction where the barrier can be fabricated with an insulting or conducting material (See Fig. 3.1c).

Due to the difficulty in achieving multi-layer fabrication in cuprate materials, several other techniques were investigated and shown to produce the Josephson effect in these materials. Some of these techniques rely on selectively introducing defects in the film during the growth. As shown in Fig 3.1d and e these defects are introduced respectively either by growing on a substrate with a twin interface of two differing orientations or by growing on substrate with a step that introduces defects at the edges. Other designs will deposit metal along the ramp and couple two planes of superconducting material across the interface (See Fig 3.1f). These style Josephson junctions are popular in fabrication of superconducting circuits in cuprate materials for their relative ease of fabrication, tunability and reproducibility [123]. However, none of these techniques, Fig 3.1d-f, produce an insulating Josephson barrier in cuprate materials with transport along the a-b plane. For applications that require a strong Josephson barrier it was necessary for a new technique to be developed for cuprate materials.

It has been demonstrated that ion irradiation incident on cuprate materials induces a metal-to-insulator transition. Moreover, this ion damage disrupts superconductivity causing both phase decoherence and pair amplitude suppression. Ion irradiation on cuprate superconductors effectively decreases T_C with increasing ion fluence eventually to absolute zero temperature meaning that the material practically no longer has a transition to the superconducting state (see Fig. 3.2) [124]. This ion irradiation causes point defects disrupting the CuO chains that results in the increased resistivity in the normal state. Also, the ion irradiation damages the CuO planes that disrupts the site of superconductivity. It is predicted that d-wave state symmetry superconductors are much more sensitive to

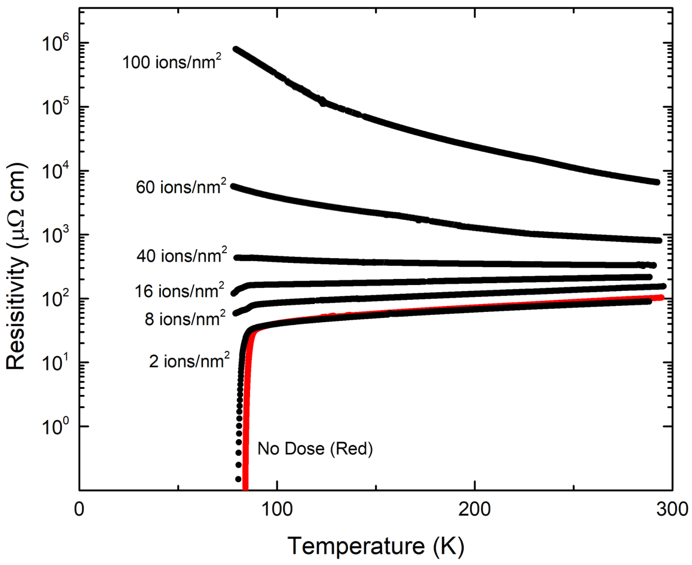

Figure 3.2: Resistivity ($\mu\Omega\times$cm) vs. temperature (K) for YBCO thin films undergoing a metal to insulating transition via irradiation with varying fluence from a 35 keV He^+ beam.

this disorder. This is due to scattering processes having spherical or s symmetry, which would destroy the superconducting state in a d-wave superconductor [125]. This inspired techniques to design and fabricate circuit elements into cuprate materials initially using lithographic techniques with broad-beam ion irradiation [126, 127]. However, to decrease the scale of the design elements, improvements to lithography or a focusing of the ion beam irradiation were necessary.

3.1 Focused Ion Beam Microscopy

Ionizing elements from a sharpened tip at high voltage was initially researched as a method to image the individual surface atoms in inverse space [128]. An example image

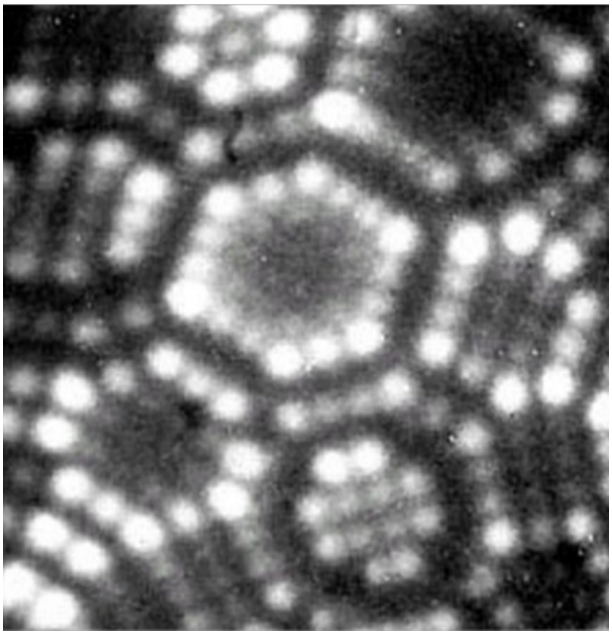

Figure 3.3: Field ion microscopy of the surface of a metallic source [128] (Image courtesy of the Penn State University Department of Physics).

is presented in Fig. 3.3. However, it was discovered that the excited ions can be accelerated and focused through an aperture and manipulated by a series of electromagnetic lenses. This technique was developed into commercial products for the purposes of microscopy, referred as focused ion beam microscopes. These focused ion beams became important tools in nanotechnology by providing researchers and engineers a way to image and manipulate samples at the nanoscale. Some applications of focused ion beams include milling [129, 130], imaging [131], resist exposure [132, 133], ion assisted deposition [134], and single ion doping and implantation [135]. The focused ion beam is the workhorse that is the foundation for the research conducted by ONELAB, and as such influences the nuances of each experimental technique in the workflow.

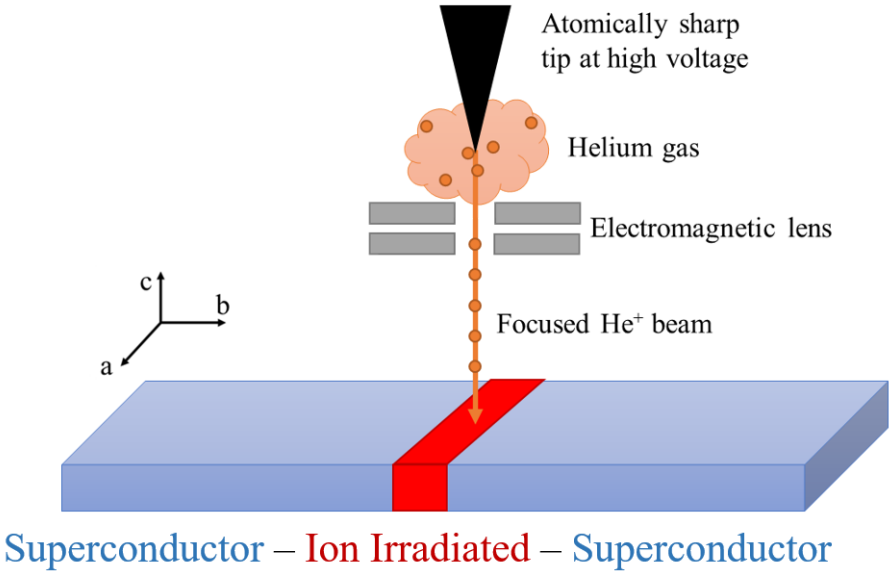

Figure 3.4: Illustrated model that depicts a He gas field ion source with its excited ion beam incident on a superconducting material causing disorder and forming a Josephson barrier.

3.1.1 Directly-written Josephson Junctions

The focused ion beam technology offers a unique capability to selectively introduce concentrated defects in cuprate superconductors and controllably tune transport properties in highly localized regions. It was already proposed that short but strong barriers were ideal for creating Josephson junctions. It was demonstrated that utilizing focused ion beam irradiation greatly simplifies the fabrication of cuprate superconducting devices [120, 2]. This process does not rely on the milling of the material. Instead it introduces defects, which greatly reduces the ion fluence necessary. Additionally, this process generates interface-less Josephson junctions with planar geometry with charge carrier transport in the *a*-*b* plane thought to be so integral to cuprate superconductivity. This technique offers an unprecedented technique to study the underlying nature of cuprate superconductors while

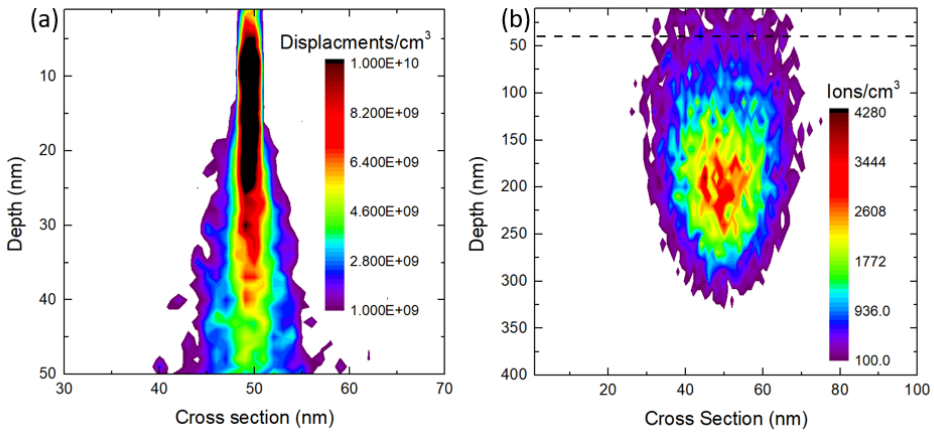

Figure 3.5: Monte Carlo simulation for an incident 35 kV helium ion beam to YBCO where (a) plots the defect density in the c-b/a planes and (b) is the halting range density in the same plane (dotted line indicates common film thickness). Simulation is performed using Stopping and Range in Matter for 10,000 incident ions.

also offering a scalable and tunable approach to device fabrication.

Focused ion beams can be produced from several species of elements with Ga, He, and Ne being amongst the most common. Accurate scattering distances and defect rates can be modeled by Monte Carlo simulation via the Stopping and Range in Matter (SRIM) or by Silvaco Athena software. Ga focused ion beams feature common liquid metal sources with typical beam spot sizes of ~50 nm. Due to the spot size, atomic mass, and beam energy of this class of focused ion beam, the qualities of the Josephson junctions produced from this source are not much improved over masked broad-beam fabricated junctions [1, 126]. Instead the qualities desired in the ion species for direct-written Josephson junctions are an ion with deep penetration, small spot size, and high energy. In this way, helium becomes a prime candidate satisfying these requirements as well as being a relatively inert element.

ALIS^{TM}, now a part of Carl Zeiss Microscopy^{TM}, developed a gas field ion source

for their helium focused ion beam in 2006 [136]. The company claims a ∼.5 nm spot size, smaller than conventional focused ion beams by a factor of two orders of magnitude. Using several methods combining both measurement and simulation, we estimated the practical spot size of the beam to be 3 ± 1 nm [137]. The work herein was performed on two tools they developed. The Carl Zeiss Orion Plus and the NanoFab. Typical beam parameters for these tools were accelerating voltages in range of 30-35 kV and currents in range of .1 to .5 pA. An example of SRIM analysis is provided in Fig. 3.5, it shows that ion damage is finely concentrated within a depth of ∼40 nm, and that the majority of the ions halt beyond this point, with an average range of about 200 nm. This suggests YBCO thin films with approximately less than 40 nm thickness are recommended and most ions would be deposited within the substrate as to limit helium doping within the film. By controllably scanning the helium ion beam across thin films of YBCO it has been shown to create Josephson junctions with behavior that is tuned by the ion fluence [120].

3.1.2 Operating a Helium Gas Field Focused Ion Beam Microscope

To a typical user of a gas field ion source microscope, there is very little difference in operation compared to more common scanning electron microscopes beyond the obvious differences in the effective mass and energy of the ions vs. electrons. Picture quality must be optimized by adjusting focus and stigmators in much the same way between the two systems. However, there are some clear differences that become readily apparent when discussing necessary regular maintenance. This section will also elaborate on beam parameters and spot area optimization. Prior to the installation of the Zeiss Orion Plus at the University of

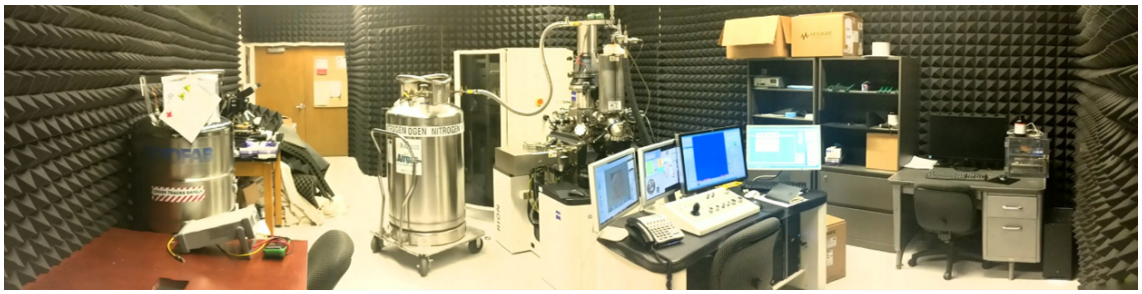

Figure 3.6: Picture of a Zeiss Orion Plus Helium Ion Microscope installed in the Univerisity of California Riverside's Physics building basement, well-insulated against acoustic noise by floor to ceiling dampening foam.

California, Riverside, extensive site surveys were conducted to ensure a proper environment for a sensitive tool. Acoustic and electromagnetic noise levels, even the degree to which the floor was level were recorded and considered. A room in the basement of the Physics building, carved into the side of a hill, was the chosen site and an ideal quiet environment. Additionally, precautions were taken, such as the construction of a closet where critical vacuum pumps could be placed near the tool but also isolated from it. Moreover the room is lined floor to ceiling with acoustic noise dampening foam. A panoramic picture of this laboratory space can be viewed in Fig. 3.6

There are two regularly reoccurring maintenance requirements that are essential for tool upkeep. Firstly, the atomically sharpened tip must be rebuilt with somewhat regularity. In a gas field ion source the tip that generates a large potential field is sharpened to the atomic level to produce the most concentrated beam possible. It was found the most stable and suitable configuration was to sharpen the tip to a 3 atom lattice. This three atom structure, referred as a "trimmer," can be viewed in Fig. 3.7. Imaging is conducted in a focused ion beam microscope by detecting excited secondary electrons by ion beam

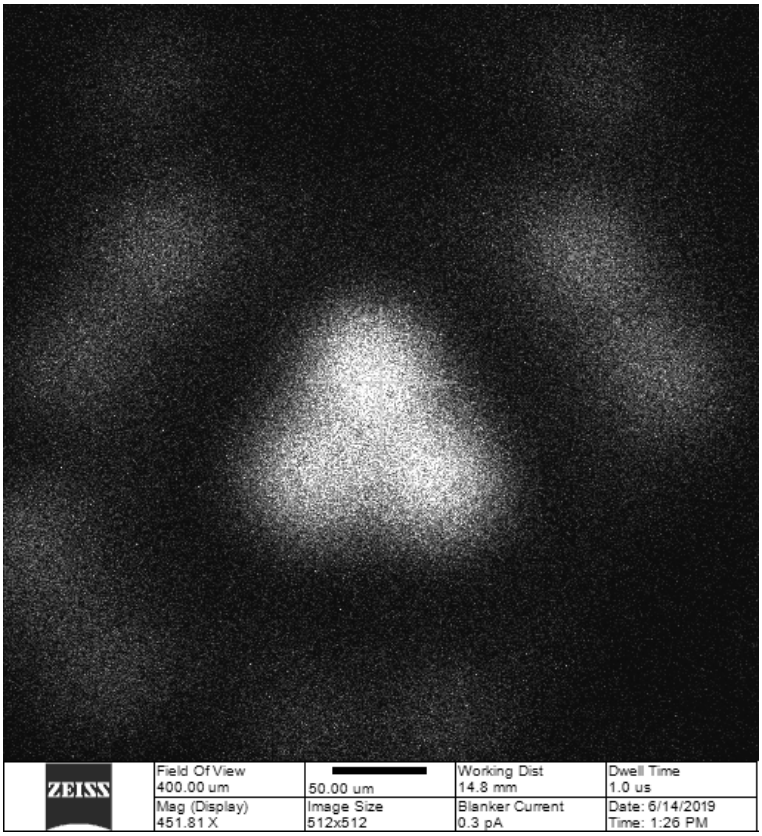

Figure 3.7: Scanning Field Ion Microscopy (SFIM) image of the gas field ion source. Trimmer (bright three circles in triangle formation) forms the apex of the tip with the underlying layers visible expanding behind it.

irradiation. It is for this reason that the most suitable materials for ion beam microscopy are highly conducting and have low impedance electrical connections to ground to replenish secondary electrons. Typically, this is accomplished by making several wirebond connections to the stub that is mounted to the grounded stage. However, if the sample does not have appropriate contacts it is possible to use silver paint to create a connection to ground. If a sample is not a good conductor it becomes significantly more challenging to properly image in a focused ion beam microscope. It may be possible to use an electron flood gun to replenish discharged secondary electrons or the sample may be coated in a fine conducting film, yet this method may disrupt surface features.

The lifetime of the trimmer can vary but average lifetime was two weeks with the longest lasting five weeks. However, deviations in source performance motivated us to reform the source for longer lived trimmers at about three weeks lifetime. Source reform initially involves a Zeiss proprietary process that I am unable to speculate on in this format. This process is restricted to five times a day to prevent overstressing of the tool, and it primes the surface of the tip for trimmer formation. Trimmer formation involves manually increasing the extraction field voltage applied to the tip stripping away the outermost layers of the crystal until a trimmer is formed. When a trimmer is formed the extraction voltage is then lowered to maximize the total current extracted from the tip. The extraction voltage that maximizes this current value is referred as the best image voltage, which determines the upper limit of acceleration voltage. Common values of the best image voltage were $\sim$30-35 kV in our systems. The voltage that accelerates the ions in the beam may not pass above the extraction voltage. While the tool may be operated with an extraction voltage

above the best image voltage, this risks the stability of the trimmer and lowers the overall current in the beam. However, higher kinetic energies of the ion beam are attainable in this way which may be useful in certain applications. Moreover, we discovered deviations in trimmer performance in the 24 hours after a trimmer reform and suggest waiting that long before using the tool for applications requiring stable trimmer behavior.

After each trimmer formation it is necessary to mechanically align the beam. For best tool performance, it is intended to select a beamlet directed off a single atom in the trimmer and align it directly down the column. This mechanical alignment initially involves physically tilting the tip such that the beamlet from the chosen atom is parallel to the column. Next, the tip is translated such that the beamlet is concentric with the column. This process ensures maximum beam current and best performance for the electromagnetic lenses within the tool column.

Secondly, the tip is kept at cryogenic temperatures by a copper coupling to an attached Dewar. It is imperative to constantly feed the tool with cyrogenic nitrogen. A small Dewar on the machine is filled twice a day with liquid nitrogen that is then condensed to the solid state which keeps the tip nominally around 80 K. Failure to transfer the cryogenic will lead to a warming above critical temperature ($\sim$100 K) within a day. Above this critical temperature the tool will safely turn off high voltages to protect the tip and it is advised to reform the trimmer after warming above these temperatures. Typically a 230 L Dewar of liquid nitrogen will maintain tool temperature for roughly 2 weeks. These two tasks should be in the care of a superuser as they require a deeper understanding of tool operation. Normal operation of the tool ought to be simplified enough for a normal user.

The nominal operation process for a user initially involves electronic beam alignment. In Scanning Field Ion Microscopy (SFIM) mode, electronic beam tilt is adjusted to maximize beam current by aligning to the chosen trimmer atom from the mechanical alignment process elaborated upon previously. Next, electronic shift is adjusted such that if a slight wobble of the lens 2 voltage value is introduced there is no shifting of the image in normal imaging mode. These two electronic beam alignment steps account for imperfect alignment from the mechanical alignment post trimmer reform. Finally, the image can be optimized by adjusting focus and stigmator lenses. As with most things, it takes time and experience to produce the most optimized beam. Spot size and shape can be roughly determined by exposing a single point of a conducting surface to the beam for roughly a second which produces a darkened area. It is important to note here that operators are reminded that imaging and single point exposures can introduce a significant amount of dose depending on intended application. It is important to be mindful of location and dose of all exposures as they may effect the irradiated sample. An example of well optimized beam spots are given in Fig. 3.8.

At this point the beam has been optimized and is now ready for whichever application the operator desires. Typically, for applications requiring the highest degree of resolution, it is important to restrict writing to within a 100×100 μm^2 square area surrounding the area where the beam parameters were optimized. If moved outside this area optimization of the beam is suggested.

While rudimentary, the Zeiss software contains some pattern writing abilities either by manually drawing of shapes or inputting a .bmp file. However, we typically utilize

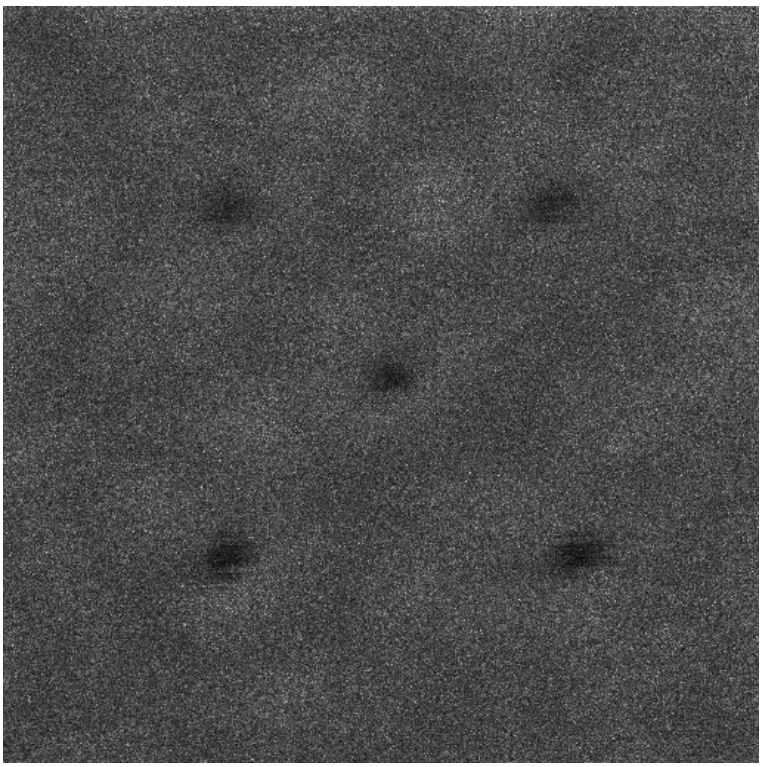

Figure 3.8: Image of five single point exposures used to estimate the spot area of the He focused ion beam. Field of view of image is 100 nm $\times$ 100 nm.

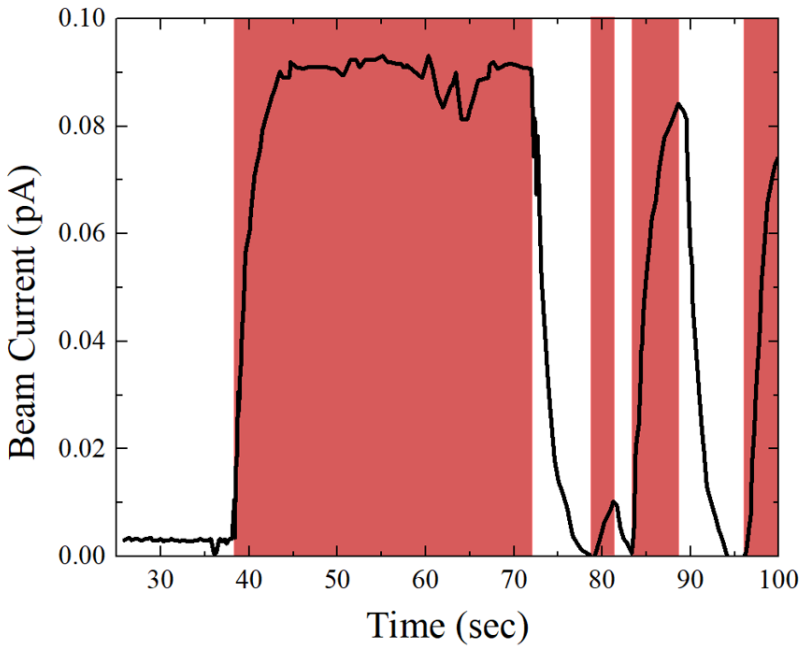

Figure 3.9: Helium ion beam current from the Zeiss Orion Plus plotted against time while alternating the beam blanker on and off. Regions highlighted in red indicate the blanker being on.

both the Fibic's NanoPatterning and Visualization Engine (NPVE) and Raith's ELPHY lithography software that features much more sophisticated pattern writing. Using these programs we can define exposure regions and dose for the nanolithography applications.

Dose for the irradiated regions would be estimated by reading out the beam current which can yield an ion fluence from the estimated spot size. The beam current can be measured by directing it into a Faraday cup and readout by a sensitive ammeter. On the Orion Plus, we had a Faraday cup mounted on the sample holder. We measured the incident beam current alternating the beam blanker on and off several times. The current was measured using a Keysight B2981A Femptoammeter, and is plotted in Fig. 3.9. From this time dependence of the beam current upon being blanked and unblanked there is a

rising and decay time on the scale of ∼8 sec. Furthermore, by integrating over these rising and falling times there is a difference of roughly 15% of total ions fluence in these regions of current transience. The typical exposure time for a Josephson junction dose with a beam current of .5 pA is <1 sec. Consequently, a large source of deviation in Josephson junction direct-writing via focused ion beam is attributed to deviations in current in the time scale of exposure. A major improvement in this technique would require a method to measure beam current simultaneous with beam exposures.

3.1.3 Large-Scale Focused Ion Beam Lithography

In comparison to other more conventional lithography techniques, focused ion beams do not benefit from the same development. Originally intended for microscopy, it wasn't until researchers had hands-on experience that other applications became more evident. Consequently, these tools are still somewhat clumsy to use and don't offer a turnkey experience to the operator that is becoming more common in the sophisticated and commercialized fabrication tools. Currently, there are only rudimentary pattern writing software developed for focused ion beams.

Most of the pattern writing and imaging herein was accomplished by using the NPVE system. This program was originally designed for milling purposes but it sufficed for direct-writing of Josephson junctions if some care was taken. NPVE was able to convert .dxf pattern files and generate a proprietary pattern file that would drive the beam and control the dose of exposure in a single writefield. In order to achieve a uniform Josephson barrier, we must ensure that the program can achieve point-to-point spacing less than the length scale of the beam spot size. Consequently, there are two technical considerations

that limited the writefield area to below 100^2 μm^2. Firstly, the beam spot area and shape was highly sensitive to deviations caused by defocusing, stigmation, and stage mechanical vibration and drift. In order to ensure consistent conditions for junction writing the stage would be stationary during writing and instead the beam would be controllably deflected to the intended region for exposure. This deflection was restricted to within a field of view with side lengths of 100 μm to ensure consistent and high-quality writing at the lowest resolutions. Additionally, a software limitation was imposed due to pixel resolution at the smallest scales could overload the hardware. Maintaining sub-nanometer point-to-point spacing for field-of-views larger than 100^2 μm^2 will overextend computer memory. Therefore, while it was possible to achieve small-scale relatively simple designs, this technique relied on manually stitching together writefields for larger more complex designs. This greatly reduced the scalability of focused ion beam written patterns. Consequently, a new control technique is necessary to achieve larger scale patterns that maintain the lowest resolution capable for focused ion beams.

Originally, designed for scanning electron microscopes RAITH extended the capabilities of their ELPHY lithography software to include focused ion beam systems. This sophisticated software was developed for complex lithographic patterning. Raith ELPHY could handle automated writing by controlling stage moves, focusing, beam handling and pattern writing via a programmable list of commands. Regardless, the process is still limited to writefields of 100 μm by 100 μm by the technical considerations. Previously, manual optimization of the beam would be necessary for each writefield. Conversely, utilizing Raith's ELPHY the operator's manual alignment would only be necessary at several global align-

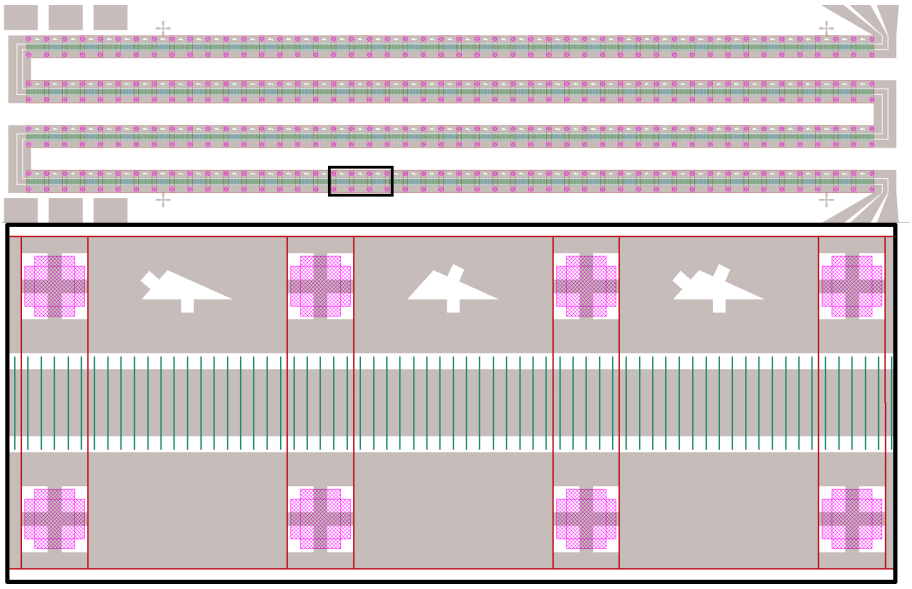

Figure 3.10: Images of the GDSII pattern file that can be input as a portion of the directions for the automated write process. Top is the whole patterned device. Bottom is a detailed view of the three writefields outlined in black on the top image. Gray indicates patterned material, the green lines are the junction write locations, hatched pink is an indicator for the automated focusing lithographic features and the red lines outline the writefields [138].

ment markers. This would map the surface plane of the sample and would be used in part to maintain the beam parameters. A set of commands can then be programmed, referred as a position list, that would tile and stitch writefields appropriately based on the pattern design. As part of the position list instructions, a GDSII file would be input that included patterns for both the sample geometry and intended regions for beam exposure. An example GDSII file is indicated on Fig. 3.10. It is now possible for the software to iterate through each writefield, autofocus on specific sample geometry, and write the intended patterns at a specified dose. This process drastically reduced the operator's manual input for large-scale design while maintaining resolution at the smallest scales, effectively reducing the need for user input from O(N) to O(1) in Big O notation, where N is the number of writefields for a given layout design. It was shown that this automated process does not drastically increase

the deviations of the design elements at the smallest scale, which is elaborated upon in Sec. 4.4. This development of automated large-scale lithography with a focused ion beam demonstrates its scalability to large and complex circuits [138].

3.2 Thin-Film Cuprate Deposition

It was already mentioned that the limitation for focused ion beams is the depth to which an excited ion may penetrate. Consequently, the devices in this dissertation are limited to single layers of YBCO thin films. These films were sourced from within ONELAB at University of California Riverside, its collaborators, or purchased commercially. Commercial purchasing of typical YBCO thin films proved to be economical and left the deposition tools more open to the active research of less common materials, such as the rare-earth cuprates [139].

Due to the difficulty of film growth in other orientations, c-axis, that is normal to the substrate, is the common growth orientation in YBCO thin films. This has the additional benefit of putting the axes with the best transport properties in the sample plane. Optimally doped YBCO may feature T_C up to 93 K; however, in thin films the surface morphology is rougher and typically results in more defects leading to lower T_C observed between 84 and 90 K.

3.2.1 Substrates

Substrates are the underlying material upon which the films are deposited. There are several factors to consider when selecting the substrate for an experiment. In order

Substrate	Structure	Mismatch	Dielectric Constant	Notes
R-plane Al_2O_3	hexagonal $a = b = 4.76$ Å $c = 13$ Å	6%	9.4-11.6	reacts with film
CeO_2 Buffered Al_2O_3	cubic $a = b = c = 5.41$ Å	.7%	9.4-11.6	stress cracking
LSAT	cubic $a = b = c = 7.74$ Å	0%	23	expensive
$LaAlO_3$	rhombohedral $a = b = 3.79$ Å $c = 13.11$ Å	2%	20.5-27	twinning

Table 3.1: Notable substrates for YBCO film growth and their properties.

to reduce the strain and defects in the grown films there must be little lattice mismatch between the substrate and film material. Furthermore, it is desirable for both materials to have similar thermal expansion coefficients to avoid stresses that may lead to cracking when temperature changes are induced. Moreover, to minimize losses and optimize performance at RF frequencies, it is preferable to utilize materials with small dielectric constants and loss tangents. Additionally, for certain substrates "bubble-like" structures have formed under ion irradiation. For example, in Si-based substrates, ion irradiation damages bonds that lead to deformations on the substrate surface that could induce additional stress or cracks in the thin film [140]. For YBCO there is no clear all around best substrate for every application, instead it is better to choose specific substrates for a given purpose.

A list of common substrates utilized with YBCO thin films are listed in Table. 3.1. A notable substrate is LSAT developed by Bell laboratories specifically for lattice matching. It is a 30/70 mole % solid solution of $LaAlO_3$ and $SrAlTaO_6$. By altering the percentage of the two molecules it can be matched to a wide variety of high-T_C superconducting ma-

terials. However, this material suffers from a spatial varying dielectric constant, reducing its performance at microwave frequencies. Another pertinent substrate is R-plane sapphire (Al_2O_3) which is relatively inexpensive and also features a low dielectric constant making it excellent in high frequency applications. However, sapphire reacts with YBCO forming an undesirable oxide interfacial layer. A common solution to this problem is the deposition of a thin buffer layer of CeO_2 before growth of the thin film. This buffer layer has a relatively low lattice mismatch at .7% and prevents the YBCO-sapphire reaction. This has become the standard substrate for YBCO thin films < 350 nm, since thicker films crack from the strain. Other substrates that perform well are prohibitively expensive in some cases. Consequently, for the majority of the work in this thesis, CeO_2 buffered sapphire are the substrates used in the samples. They can be economically-sourced commercially and they ensure that future incorporation into RF devices is simplified. The unit cell of sapphire is a hexagonal structure, where $a = b$ 4.76 and $c = 12.97$ Å. The lattice structure may be diced along the R-plane so that the surface resembles a rectangular lattice. A thin buffer layer ($\sim$10 nm) CeO_2 may be grown on the sapphire that features a cubic unit cell structure with lattice structure a=b=$c = 5.41$ Å. This is a lattice match to the a-b plane of YBCO, orientating the c-axis normal to the substrate.

3.2.2 Film Growth

There are several methods suitable to growing thin films of cuprate superconductors. A common method is by laser ablation, also referred as pulsed laser deposition (PLD). PLD is relatively inexpensive and less complicated comparing to other methods. Also, it is performed with higher background pressures. However, it is limited to small wafers ($\sim$1

cm^2). Smaller sample yields lead to greater deviations between samples as more growth runs are necessary. In the PLD process a laser incident on a stoichiometric target causes ablation of the material. This forms a plume of plasma mixed with one or more carefully introduced background gases. A substrate mounted nearby on a heater will collect material from this plume forming crystals.

Another common method is via thermal co-evaporation. Most of the discussed devices in this dissertation were commercially purchased by Ceraco GmbH who specialized in this methodology for the deposition of YBCO thin films [141]. This method requires more strict background pressures with chambers capable of achieving vacuum below 10^{-5} Torr. Individual components of the material to be formed are placed in metallic crucibles through which passing currents cause resistive heating that can be used to control the rates of evaporation. Simultaneous evaporation and control of the rates of vaporization of these elements can tune the desired stoichiometry of the vapor cloud. In YBCO the controlled introduction of oxygen to the growth process is one of the most important components to grow optimally doped films and could have significant effects on transport properties and T_C. The thermal co-evaporation process is complicated in YBCO since the necessary background pressure for oxygen limits the mean free path of the vapor plume and impedes crystal growth. Special compartments are designed inside the chamber such that a portion of the wafer can experience the optimum oxygen pressure. The wafer is thus rotated between the two environments. While more complicated, this process results in larger, more consistent samples. In this dissertation, most YBCO samples were fabricated on 2 inch diameter CeO_2 buffered R-plane sapphire with 35 nm of YBCO grown via thermal co-evaporation

and capped with 200 nm of gold deposited *in-situ* for electrical contact. They featured a T_C of ∼84 K and critical current denisty J_C of 3.5 MA/cm^2 at 77 K.

Finally, one last deposition method is pertinent to the samples that will be discussed in later chapters. Oxygen ion beam assisted deposition is another method that was utilized in ONELAB as a way to fabricate experimental rare-earth cuprates conducted by my colleague Stephen McCoy and it is elaborated on in his thesis [139]. This methodology addresses challenges of the introduction of optimum oxygen pressures that complicates the thermal co-evaporation method. In this method, a target of the desired material is bombarded by argon ions that sputters the material into a plume concentrated by a series of strong magnets onto a heated and rotating substrate. For ion-assisted deposition a secondary ion beam, in this case forms an oxygen plasma that floods the growth chamber allowing for optimized oxygen doping while improving surface morphology. While these ion-assisted sputtering systems are hard to maintain and are relatively more complicated in process, they offer superior control over the deposition.

Due to the complexity of the unit cells of cuprate superconductors and lattice mismatches with the substrates, growths of thin films are subjected to high strain that will introduce defects in the lattice. Consequently, thin-films of cuprate materials grown via deposition on substrates are not often characterized as single crystals. Typically, the films grow in spiral patches referred to as grains. The orientations of these grains may be correlated, but remains a research question depending on deposition method and substrate choice. A scanning electron microscope (SEM) image of the surface of a film grown with exaggerated grain boundaries deposited via ion beam assisted deposition of YBCO on

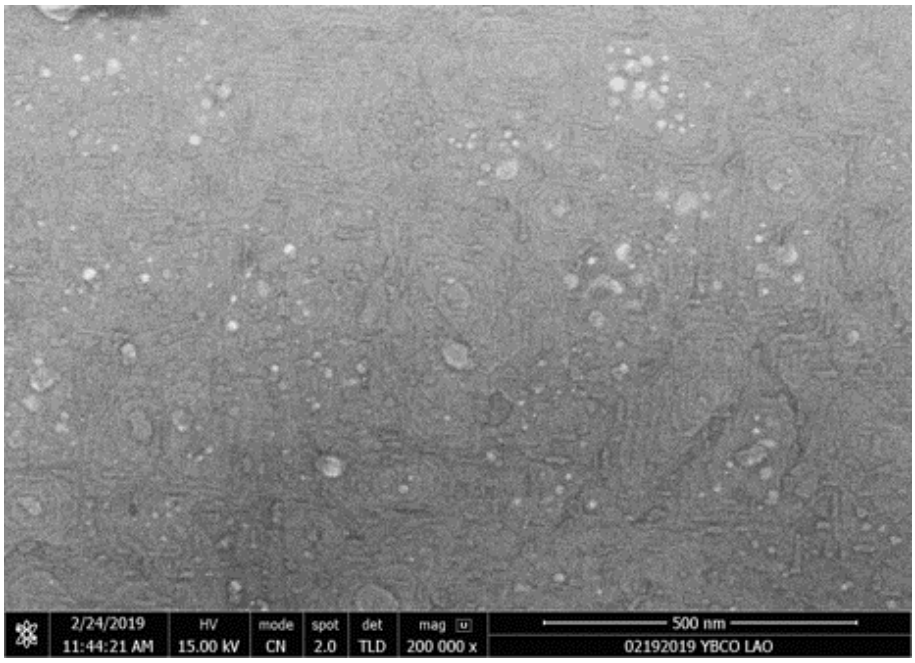

Figure 3.11: Scanning electron microscope image of the surface of a YBCO film grown on a LAO substrate. Spiral grain growths are clearly visible, each roughly on the scale of a 1000 nm^2.

$LaAlO_3$ (LAO) is presented in Fig. 3.11. Individual grain growths are visible, each roughly $\sim$1000 nm^2. Furthermore, grown thin films can exhibit twinned boundaries across which the crystal lattice is mirrored with a symmetric misorientaion. Another sample of YBCO grown on LAO is imaged via SEM in Fig. 3.12 that demonstrates an exaggerated example of the presence of twinned boundaries. Due to the formation of these two types of defects it is not trivial to determine crystal orientation, which can be critical in the case of an anisotropic pairing symmetry.

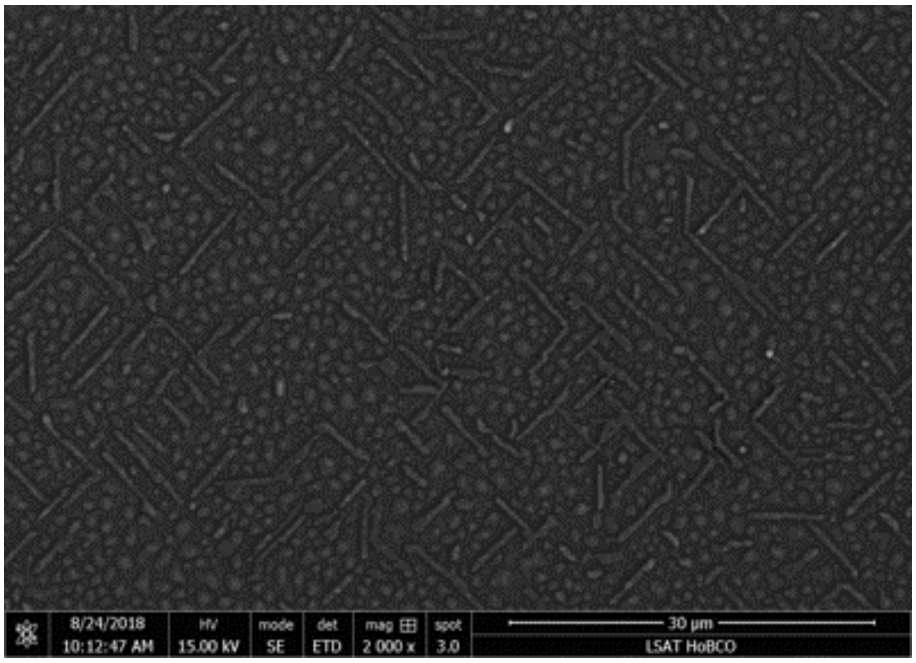

Figure 3.12: Scanning electron microscope image of the surface of a YBCO film grown on a LAO substrate. Twinned boundaries are clearly visible.

3.3 Cuprate Lithography

While focused ion beam microscopy can perform lithographic functions at the nanoscale, it is not optimized for larger scale design layouts. For micrometer length scales and up, it is much more efficient to utilize conventional photolithographic techniques. The following section will outline the process by which the thin films will be processed to lithographically define larger scale bulk electrode paths. Fig. 3.13 is a graphical representation that represents each step in the fabrication process and may be used as a outline for the following sections.

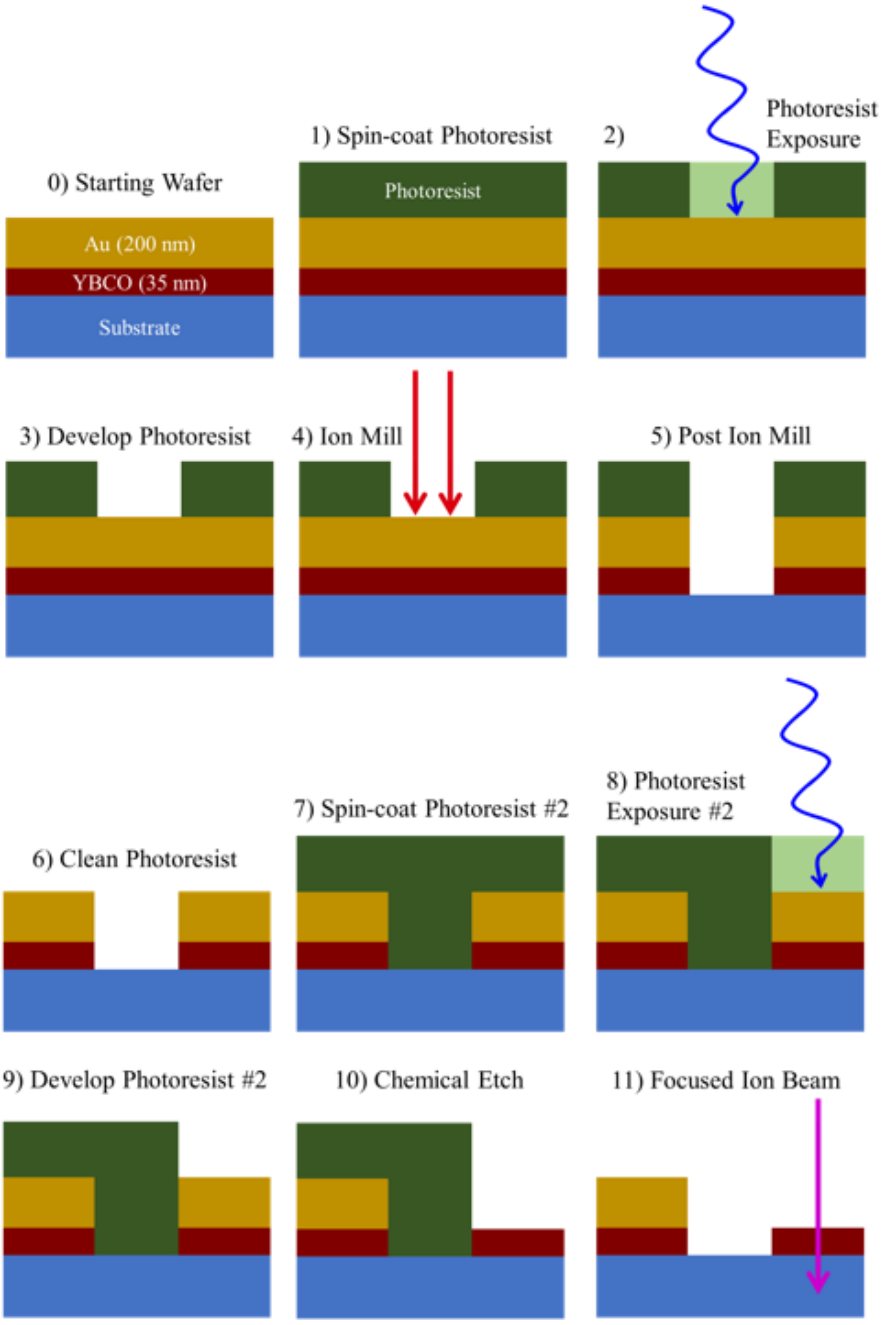

Figure 3.13: Representation of each step in the cuprate lithographic process.

3.3.1 Pattern Layout

The lithography workflow begins with an idea that must be transferred to a layout design. This process is the starting point but requires intimate knowledge of the whole process in order for a layout design to succeed. It is important to consider the technical limitations of the fabrication tools and measurement scheme to achieve a successful layout.

To ease the difficultly associated with the technical aspects of drawing, a computer assisted drawing (CAD) program is utilized. CAD programs can be complicated tools featuring the ability to accept custom coding snippets and perform finite and lumped-element simulation or as simple as the Microsoft Paint program. Typically, the challenge of these programs is not the drawing itself but the knowledge of what tools are available and how to access them. For the purposes of this dissertation, the programs of L-Edit and Clewin were utilized. L-Edit is a much more capable program but is clunky to use for simple designs. Whereas, Clewin is quick and easy but lacks some important features. Clewin is a proprietary CAD program associated with the photolithography tool to be elaborated in Sec. 3.3.2.

Several pattern layouts were developed for experiments herein using these CAD programs. These layouts would contain the bulk lithography geometry defined for both the YBCO and Au films and the associated focused ion beam irradiated regions defined in their own distinct layers. Plotting everything together in the same layout file is helpful for visualizing the process. It is suggested to contain alignment marker elements designed into the bulk electrode geometry for both direction finding with the focused ion beam microscope at the micrometer scale and to assist focusing which is necessary within 200 μm

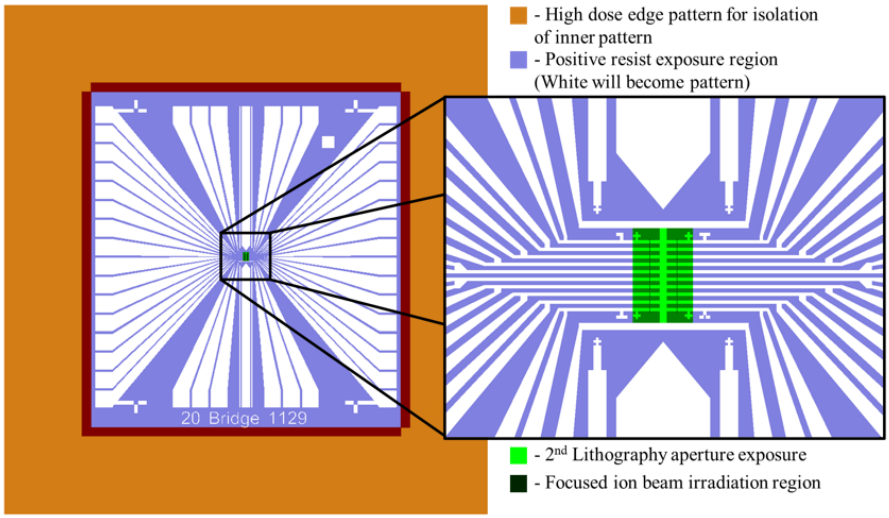

Figure 3.14: Example of a successful layout design in GDSII format.

of the intended writefields. Furthermore, the L-Edit program is necessary to use to define zero-width lines to be recognized on the focused ion beam lithography software. With Clewin, for instance, they are still recognized as areas. This is important for achieving the thinnest possible irradiation regions, which is integral for fabrication of high-quality Josephson junctions. These are some examples of where experience with the fabrication process aids in the layout process. The layout design in Fig. 3.14 is referred as the "20 Bridge" pattern and it is used to perform dose tests for single Josephson junctions post trimmer reforms to test the working state of the He ion microscope.

The 20 bridge pattern is an example of a practical layout design that is robust and has been extensively tested and iteratively improved upon. It features symmetry breaking design elements to help track sample orientation. It also features several structures in the writefield for ease of focusing the ion beam. Note also that most of the film is left intact

after the ion milling process (Step 4 from Fig. 3.13). If too much film is milled away, the possibility of diffusing oxygen atoms from the YBCO film to the substrate is increased, which will degrade superconductivity. Finally, note that the sample has large contact pads for ease of wirebonding and each device is multiply connected so that four probe terminal measurements are possible even in the event that any single terminal is defective.

3.3.2 Photolithography

Iterative updates to the design is a necessary portion of research. In photolithography, iterative approaches can be costly in time and money if one relies on third-party fabrication of masks. One of the essential tools to the ONELAB workflow was a maskless photolithography tool. The Microtech LaserWriter LW405 can accept common CAD pattern layout files, such as GDSII, and direct-write via a GaN solid state laser with a 405 nm exposure wavelength. While not ideal for the mass production of wafers, it is a massive boon in the research environment where small-scale runs of many differing designs is common. It is relatively simple to train new users and did not take much experience to become competent.[1]

This tool was installed in a class II clean room, with yellow light to limit unwanted exposure for photoresist. Samples to be written by the LaserWriter are first diced into 5×5 mm^2 square samples. Then they are spin-coated with Fuji OCG 825 photoresist for 45 secs at 5000 rpm. After spin-coating, the samples are placed on a hotplate and baked at 90° C for 120 seconds, which evaporates the photoresist solvent. Samples are mounted into

[1]From personal experience, this is the first tool to be taught to new graduate students and even undergraduate students could be trusted with running it.

the Microtech LaserWriter. It is important to focus the laser source on the sample. Then the design can be aligned and written with a dose of 325 mJ/cm^2 by a beam that scans across the sample while the stage is moved underneath. With this process it is possible to consistently achieve design elements with a minimum feature size of 4 μm. With significant care and possibly several attempts, with this tool and setup it has been demonstrated to achieve design layouts with minimum element sizes of 1 μm. Due to the small size of the chips, the photoresist thickness is uneven across the surface and tends to be thickest at the edges. It is advised to place all design elements within a 4.25 by 4.25 mm^2 square area that is centered on the sample. Additionally, it is suggested to use a high dose ($\sim$400 mJ/cm^2) exposure in the area within 1.5 mm from the edge to isolate the layout pattern, which can be viewed in Fig. 3.14 as the orange layer.

After photolithographic exposure, samples are exposed to OCG 934 developer for 30 seconds removing the photoresist that was exposed by the laser, which is referred as positive photoresist. The developer reaction can be halted by dousing the sample in de-ionized water and lightly blown dry with compressed nitrogen. The remaining photoresist can be inspected under a microscope for integrity of the design. If necessary it is possible to re-expose the sample to the developer for 5-10 second increments for underdeveloped samples. If there are significant defects it is possible to wash the photoresist off completely with acetone and gentle use of an ultrasound agitator. The process may be restarted from the spin-coating step. The chemicals in this process are chosen specifically since they do not react in a manner destructive to the superconducting state in cuprate materials.

3.3.3 Argon Ion Milling

An argon ion mill is utilized to dry etch the exposed regions after the first photolithography step. This broad-beam of energized and heavy ions can controllably sputter the surface, effectively milling it down.[2] A tungsten tip brought to high voltage ionizes surrounding argon atoms creating a plasma that can be focused by an electromagnetic field generated by a surrounding conducting grid. This is the Kaufmann ion source and is similar in function to the ion beam utilized in the film deposition, discussed in Sec. 3.2.2.

The sample was mounted in a custom vacuum system containing the Ion Tech, Inc. ion source, pumped via a CTI-Cryogenics cyro-pump to 10^{-7} Torr and both the chamber and mounting plate were cooled by chilled water. Argon was leaked into the system to maintain 1.7×10^{-4} Torr. With the beam turned on, the ions are accelerated at 500 V and a 320 mA ion current is maintained. This process mills the YBCO at a rate of 3 Å/sec and Au at 6 Å/sec. After the photoresist is cleaned off the sample, the bulk electrodes should be isolated.

3.3.4 Chemical Etching

The bulk electrodes of the sample comprise of a thin film of cuprate material capped with 200 nm of gold. Based on SRIM simulation, a He focused ion beam at 30 kV will not sufficiently penetrate the gold capping layer. Consequently, apertures must be opened so that the YBCO is exposed prior to focused ion beam irradiation in the regions to be written. Since the gold layer will be used for electrical contact, the gold needs to be selectively removed in regions to be ion irradiated. Therefore, a second photolithography

[2]It is a fun fact that originally these broad-beam ion mills were developed to be deep space thrusters.

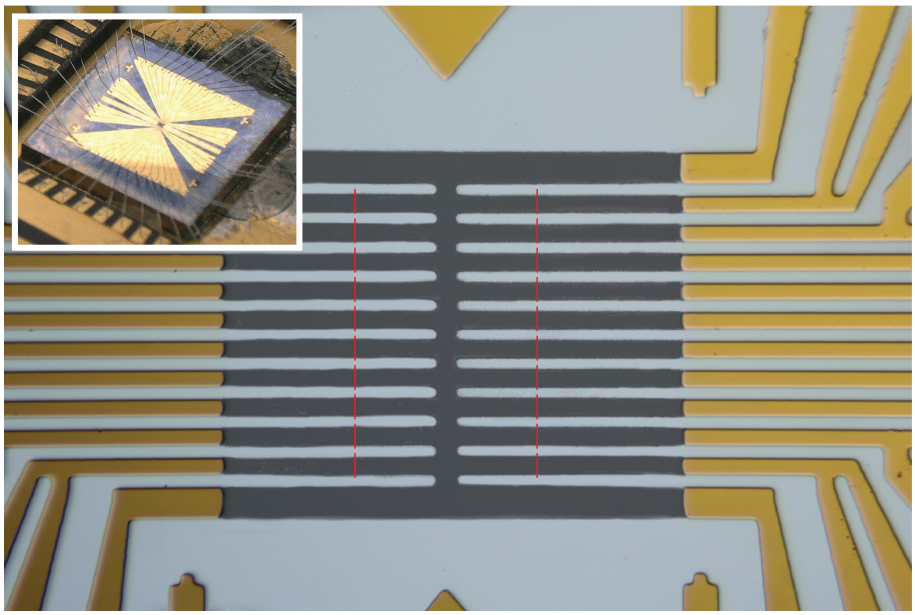

Figure 3.15: Example of a fabricated sample with each step outlined in Ch. 3. Red lines indicate irradiation regions that indicate Josephson barriers. Inset is sample mounted in and wirebonded to the package carrier.

step is conducted, that leaves regions to be irradiated exposed, while the remaining sample is covered in photoresist. While a second ion milling step can be used to selectively remove the gold layer. Ion milling in this way can be challenging and may result in the milling of the cuprate layer. Chemical etching is a faster method that is a common technique in electronics processing. It can be carried out in a similar process to photoresist development. A potassium iodide solution will etch gold with at a rate of 500 nm/min. This etchant does not react significantly with YBCO, nor does it significantly effect its superconducting state on the time scale to remove the gold capping layer. After cleaning off the photoresist the sample is prepared for focused ion beam irradiation.

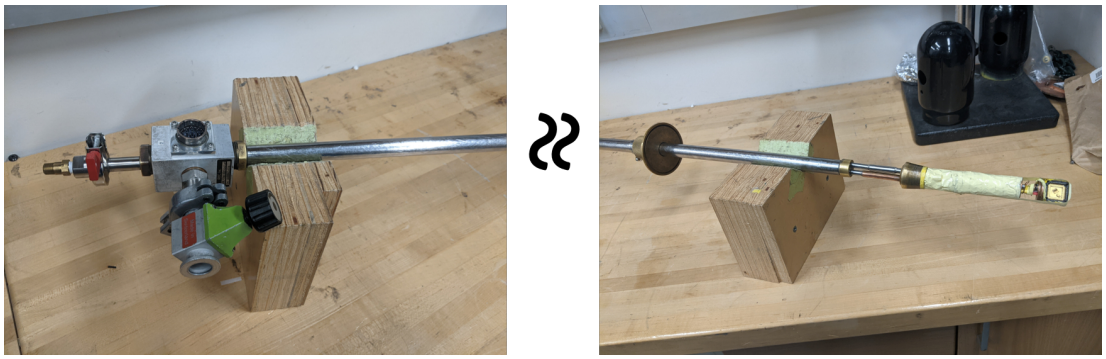

Figure 3.16: Images of the liquid helium storage Dewar insert used for low-temperature characterization.

3.4 Characterization via Transport Measurement

Transport measurements of material charge carriers can yield significant information on the nature and behavior of the underlying physics. These techniques have been in development since the dawn of electronics. Characterization techniques have significantly advanced with the advent of complex digital semiconductor measurement tools and multi-purpose characterization devices, such as physical property measurement systems (PPMSs). However, these digital electronics suffer from high voltage noise. Superconducting devices have small responses that are highly sensitive to noise, and in many cases expertise in low-noise DC measurements using analog measurement tools is necessary to properly characterize cuprate superconducting devices.

An example of a finished 20 Bridge sample fabricated with the workflow process outlined in Ch. 3 is presented in Fig. 3.15. The fabricated samples are first mounted in a 44-pin J-Lead chip carrier. On the same die, a Lakeshore DT-670 silicon diode is mounted via 2-part epoxy. Electrical connections between the sample and package are made via aluminum wire bonds by a West Bond, Inc. 7476D manual wedge bonder. This package

is mounted in a corresponding square socket in a custom built low-temperature cryogenic insert. This socket is mounted at the tip of the insert on a copper finger, and 44 wires for DC electrical connection are ran to two accessible circular MIL spec bulkhead connectors at the top to breakout the connections to the sample. A third connector is connected to an external magnetic coil mounted on the socket that biases the magnetic field of the device with a transfer function of .0087 T/A at cool temperatures. Additionally, there is a valve port to evacuate the insert, a pressure release valve and a connection for a vacuum gauge. This top portion is connected to the tip by a long stainless steel tubing with 3/4 inch diameter. A quick-disconnect fitting is welded to a Ladish flange, commonly used on liquid helium storage Dewars. The insert probe could be inserted into the Dewar and sealed shut while maintaining easy height adjustment via the quick disconnect fitting. By controlling the height of the insert above the liquid helium surface the temperature could be carefully controlled. The insert probe with mounted package can be viewed in Fig. 3.16.

A brass and *mu*-metal cylindrical can encases the tip of the insert where the sample carrier socket is mounted. It is sealed by a gallium wire press fit between a brass flange and the can. The insert is evacuated via a Pfeiffer turbomolecular pump to 10^{-6} Torr, then backfilled with 500 mTorr of helium gas to act as a temperature exchange. To cool the insert, it is first cooled to temperatures below 90 K in a Dewar of liquid nitrogen, before being transferred to a liquid helium storage Dewar. Inside the liquid helium Dewar temperatures between 100 and 4.2 K are attainable by adjusting the insert height. With careful and slow temperature adjustment and nitrogen pre-cooling, a single 100 L liquid helium Dewar could last in excess of 1 to 2 months depending on frequency of use.

To achieve an ideal measurement environment for characterization of highly sensitive Josephson devices, the samples are cooled by liquid helium in a room-sized Faraday cage built by ETS-Lindgren to shield against radio frequency noise. This electromagnetically shielded room contains only battery-powered electronics. Additionally, the insert can contains *mu*-metal shielding intended to screen background magnetic fields. Despite this however, an estimated residual field of -12.3 $\pm$ 4.3 μT remained within the can during measurement. This residual magnetic field could lead to trapped vortexes of supercurrent each containing a magnetic flux quanta within a Josephson junction that has the effect of breaking the symmetry of current flow within the junction. To further limit noise sources from higher frequencies a π-filter is affixed to the circular MIL spec connectors before being broken out by panels of BNC connections. This filter was manufactured by Amphenol Aerospace and features 50 dB attenuation at 15 MHz increasing to 80 dB attenuation for signals greater than 50 MHz. Signals are exchanged across the shielded room barrier by isolated BNC bulkheads and are fed into an analog-to-digital converter where they could be organized, plotted and saved by a custom developed Labview program.

3.4.1 Current-Voltage

Characterization through measurement of current-voltage characteristics is an important tool[3] for determination of sample behavior. It is the starting point for nearly all other measurements to be discussed in this section, and my default measurement state during all troubleshooting. Additionally, it can be used to fully characterize Josephson junction behavior.

[3]If not THE most important.

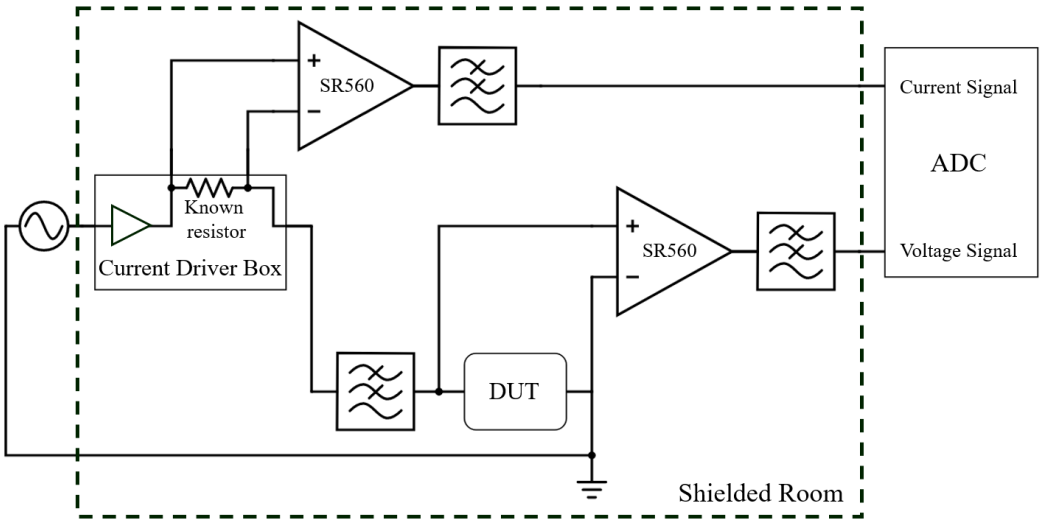

Figure 3.17: Diagrammatic representation of the current-voltage measurement scheme.

The basis of this technique requires four individual electrical contacts connected in series to the device under test (DUT). The four-point probe method is essential for accurate measurement since it eliminates interfacial, contact and wire resistances for electrical connections in series with the DUT and measurement hardware. Careful planning in the layout design and execution of wirebonding is necessary to accomplish this requirement. The four terminal method allows for the precise application of a current bias and measurement of that current and voltage applied to the DUT. The ability to accurately apply current bias in superconducting material is fundamental for characterization since there is zero voltage drop across the material in the superconducting state.

A circuit diagram of the current-voltage measurement setup is outlined in Fig. 3.17. A 1 Hz sinusoidal input signal of variable voltage peak-to-peak is output via a Keysight 33500B Series waveform generator. This waveform generator is powered by line voltage and

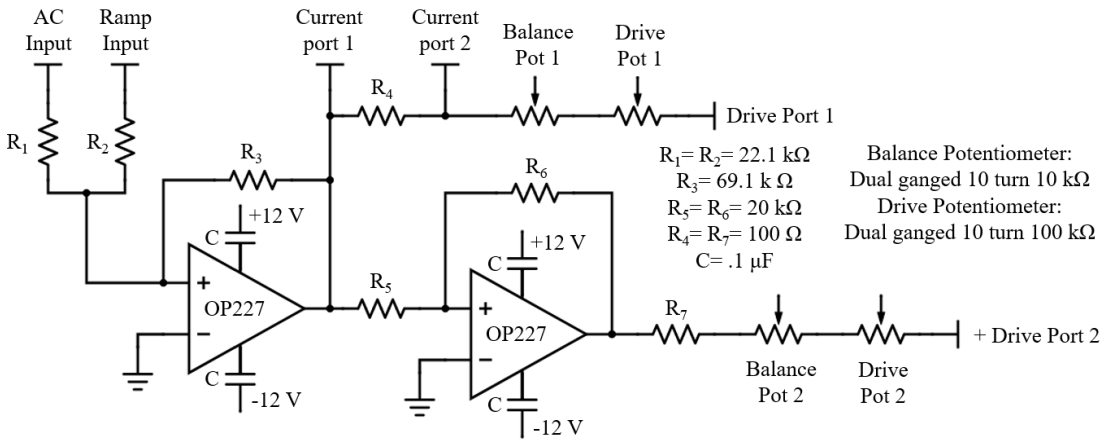

Figure 3.18: Circuit diagram for custom battery-powered current driver box.

consequently is kept on a rack located outside the shielded room, to isolate the DUT from 60 Hz noise. Its output signal port is in the high-impedance mode so that it matches the input to an amplifier in which it is connected in series with through an isolated bulkhead into the shielded room. It is connected to an amplifier input in a custom battery-powered circuit designed to current bias a DUT. The circuit schematic can be viewed in Fig. 3.18. The circuit is designed to isolate the noisy signal and replicate it before driving the voltage across a current-limiting potentiometer, a precise resistor with a known resistance, and a current-balancing set of two potentiometers. Each of these resistances are in series with the DUT and therefore measuring the voltage across the known resistor (in this case 100 Ω) yields the DUT current bias. The output drives the current across the DUT through connections to the BNC breakout box that interfaces with the liquid helium storage dewar insert. The maximum output of the custom current driver box was limited by the total voltage difference that drove the internal amplifiers, which was nominally ±12 V.

The voltage across the known resistor is input into a battery-powered Stanford Research Systems SR560 low-noise voltage preamplifier located inside the shielded room. The voltage across the DUT is input to a second preamplifier. It should be noted here that on SR560s the maximum input voltages is 3 V. This is sometimes confusing since inputting voltages greater than this value will not trigger an overload LED. Instead, the only way to diagnose this failure state is the saturation of signal. Due to this limitation, in our measurement configuration, the custom current driver box could only output a maximum of 500 μA. In addition to the circular π-filters mounted on the probe, the signals were again processed by internal filters in the preamplifiers in a low pass configuration with a cutoff at 1 kHz with a 12 dB/oct rolloff. The outputs of the two preamplifiers are then directed back out through the shielded room bulkhead feedthroughs to a National Instruments NI9215 analog-to-digital converter where the data is organized, plotted and saved via a custom Labview program. The program collects 10,000 data points for each period of the drive signal. The data is then saved via an ASCII file format to be plotted in ORIGIN or manipulated and analyzed further in a choice programming platform.[4]

An example of a common technique for current-voltage measurements is adjusting the drive signal frequency. By changing the frequency to faster or slower frequencies it is possible to characterize the presence of capacitative and inductive elements that may manifest in the current-voltage characteristics as hysteresis. Furthermore, critical current in films can be determined by increasing the current bias until the film produces a voltage. However, this method risks potentially burning the film as the switch to the resistive state

[4]My personal recommendation is Mathematica and it seems to me to be very underrated comparing to Python or Matlab.

can lead to a dramatic increase in dissipated power in the DUT. It is suggested to slowly ramp up a triangle wave on the function generator with a fast frequency to limit current exposure in the voltage state. It is also possible to estimate the excess current in the characteristics of a weak-link by extrapolating the normal state resistance back to the zero voltage intercept. In order for this estimation to be an accurate determination of the excess current, make sure to current bias the weak-link far enough such that the normal state curve appears linear (typically $I_{Bias} = 3I_C$).

3.4.2 Resistivity-Temperature

Resistivity-temperature measurements are another essential tool for the characterization of material qualities. They can be used to differentiate between conducting and insulating material. Moreover, they can determine superconducting T_C and estimate the density of material defects. Also, they can be used to determine presence of Josephson barriers in the superconducting state.

While there are several methods to measure resistance, the principle of the measurement relies on four probe terminals, just like the current-voltage characteristics in the previous section. Note that resisitivity (ρ) is a material property that can be determined by measuring resistance and accounting for the geometric terms. Recall that for Ohmic materials:

$$R = \rho \frac{\text{Length}}{\text{Cross Sectional Area}} \tag{3.1}$$

Typically, resistance must first be measured prior to calculating resistivity, which is the fundamental property.

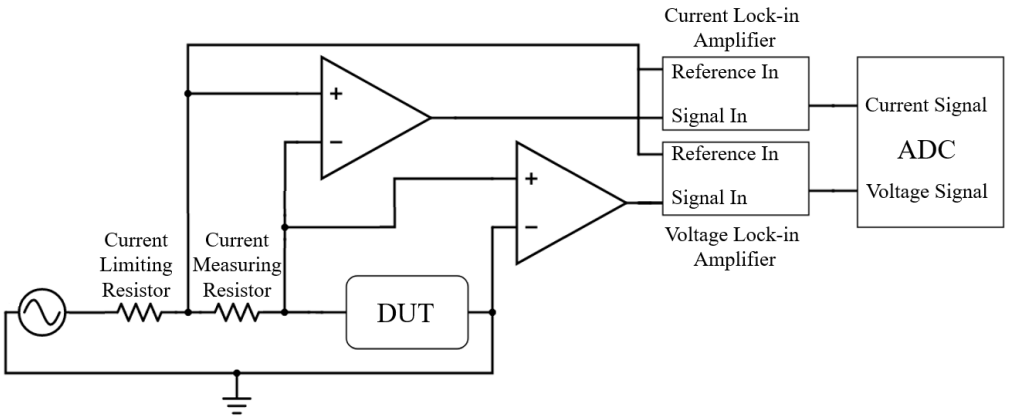

Figure 3.19: Diagrammatic representation of the resistivity-temperature measurement scheme.

For an abritrary thin film geometry if the four small electrical contacts are close to the sample edges, the van der Pauw method can be used to estimate the resistivity from the resistance [142]. Assuming a flat uniformly thick film (thickness t) that is isotropic and homogeneous:

$$\rho = \frac{\pi R t}{\ln 2} \tag{3.2}$$

While this formula is generally a good estimation, it should be noted that cuprates violate one of the assumptions, that is an isotropic response. YBCO, for instance, was already shown to feature anisotropic transport properties in Sec. 2.8.1.

A diagrammatic representation of the resistivity-temperature measurement scheme is portrayed in Fig. 3.19. A waveform generator is connected in series to a current-limiting resistor. The value of this resistance may be determined by estimating the total resistance in the DUT and associated electrical contacts and choosing a value that is several orders of magnitude over that. In this way the current input into the circuit is dominated by

the current-limiting resistor. A resistor with a comparatively small but known resistance, such that it may be neglected, is connected in series with the current-limiting resistor. The voltage drop across this resistor may determine the current in the circuit. Finally, the DUT is connected in series to this current-measuring resistor. The voltage across the current-measuring resistor and the DUT are input to preamplifiers and filtered with low-pass filters with settings that pass the drive signal. The outputs of the preamplifiers are input into lock-in amplifiers. The lock-in amplifiers most commonly used herein was the Stanford Research Systems SR2124 Dual-Phase Analog Lock-In Amplifer used on the voltage side and the Signal Recovery 7265 DSP Lock-In Amplifier for the current-signal voltage. These lock-in amplifiers take a reference signal from the function generator of the drive signal and "lock" to it. Signals with other frequencies are discarded. The outputs of the lock-in amplifier are input into an analog-to-digital converter that intefaces with a custom Labview program which collects, plots and saves the data. To accurately measure a signal, a lock-in amplifier requires integrating across several periods of the drive signal. Therefore, for an integration time, referred as a "time constant," to be less than the time varying resistance of a sample cooling via liquid nitrogen from room temperature we need an integration time of $\sim$300 msec. Typically, this value informs the frequency of the drive signal. A common value is 23 Hz since it has several periods in the integration time and it is a prime number, which means we can limit noise from harmonic modes. It is not strictly necessary for current to be directly measured when using an appropriately valued current-limiting resistor since a good estimation for current could be determined by the input voltage and the resistor value alone. This technique can be an accurate estimation for the resistivity if the DUT does not

change resistance values significantly in comparison to the current-limiting resistor.

The lock-in electronics can measure both the real and unreal components of the signal by comparing the reference signal phase to the input signal. The X and Y components of the phasor diagram notation may be output by a lock-in amplifier. When measuring resistivity we neglect capacitance and inductance in the system to simplify the mathematics. Generally, this is a good approximation for cuprate materials measured by this scheme. However, measurements with Y values that are a significant fraction of X should be discarded since it suggests a significant capacitance or inductance in the system that violates our assumptions. This sometimes results if the interfacial electrical contacts connecting to the DUT are not making clean connections. Due to the filtering capabilities of lock-in amplifiers, less care is necessary to avoid noise in comparison to the current-voltage measurements. A shielded room is no longer necessary and line-powered electronics may be utilized. Consequently, this measurement scheme is more suited for benchtop setup.

The temperature is readout via a Cryo-con model 54 temperature controller. This controller may interface to either temperature calibrated resistors or diodes and relay a temperature value back to the Labview program. Similarly, this controller makes precise 4 terminal measurements of the resistivity of the temperature sensing element mounted in the insert physically close to the DUT.

It should be noted that resistivity-temperature characteristics may also be measured by taking current-voltage measurements for changing temperatures and then using a linear fitting regime from an analytic processing program. This method was found necessary in highly-resistive insulating materials due to a capacitative-like charging effect, which

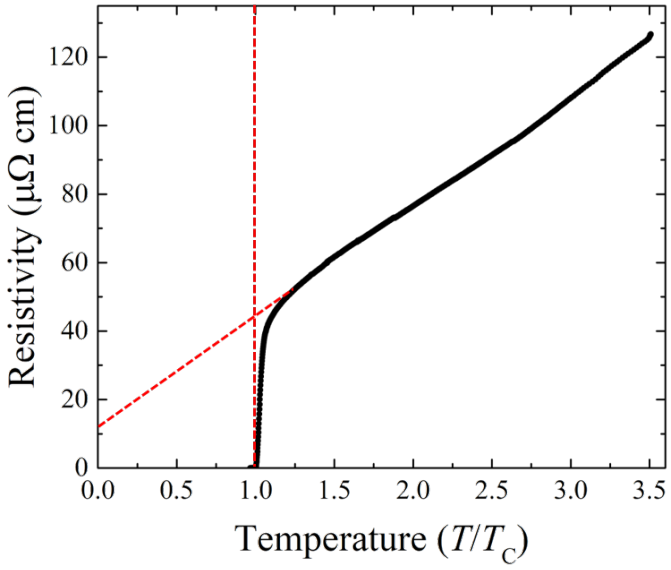

Figure 3.20: Example resistivity ($\mu\Omega$ cm) vs. temperature (normalized to $T_C = 84$ K) of a YBCO thin film. Red dotted vertical line indicates T_C and slanted red dotted line is extrapolated linear fitting to indicate residual defects at zero kelvin.

could be diminished if the drive frequency was set below 1 Hz. In order to increase the number of data points, the lock-in integration time was ignored with this method and a data point could be saved for each period of the drive signal.

Material properties can be inspected by resistivity vs. temperature figures. With decreasing temperature, a material in which the resistivity value decreases is defined as a conductor and vice versa is referred as an insulator. Meanwhile, the temperature and width of the superconducting transition can yield important film properties and even information on the strength of the underlying superconducting pairing potential. For a defect-less conductor the resistance should go to zero at absolute zero temperature. Therefore, an estimation of the defect density in the film may be approximated by extrapolating the conductor

resistivity to zero Kelvin. Finally, observation of finite resistance below the superconducting transition of a Josephson junction may yield information about the nature of the Josephson barrier. An example of a resisitivity-temperature characteristic of a YBCO thin film is given in Fig. 3.20 and indicates some of these characterization techniques discussed.

3.4.3 Voltage-Applied Magnetic Field

Superconducting materials and by extension Josephson devices are magnetically sensitive materials. For instance, there is some critical magnetic field strength that breaks Cooper pairs and induces a transition back to the normal state. Typically to measure the sample behavior to an applied magnetic field, the measurement scheme is set up initially for a current-voltage characteristic. An additional function generator is connected in series with a current-measuring resistor and wire coil that will magnetically bias the sample. The voltage across the current-measuring resistor will be amplified and directed to the analog-to-digital converter in the exact scheme previously described to measure the DUT current bias. In this fashion we will know the current in the coil and from a transfer function we can estimate the magnetic field applied.

Similar to the method to determine the film I_C, the magnetic field can be slowly increased until a voltage results when the applied field strength is above the critical field and starts breaking Cooper pairs. More commonly, voltage-magnetic field characteristics are taken to characterize the magnetic field response to Josephson devices. For devices like Josephson junctions and SQUIDs, the I_C modulation by the interference of the superconducting phase induces a voltage response depicted in Fig. 2.18. Generally, the Josephson device is DC current biased to just above the I_C and the voltage response is recorded while

sweeping the magnetic field at 1 Hz.

In our setup we had a small coil mounted around the package carrier socket inside the liquid helium insert that was used to magnetically bias the device. In this setup our drive signal was limited to 20 V peak-to-peak, which translated to a magnetic field bias range of ± 500 μT.

3.4.4 Critical Current-Applied Magnetic Field

The setup for measuring the I_C-applied magnetic field is the same as the previous section (3.4.3). However, this time the Josephson device current bias will be varied at a fast frequency while the magnetic field is slowly oscillated. For example, if the Josephson current drive signal is 10 Hz and the magnetic coil drive signal is .01 Hz. We can resolve 1,000 current-voltage characteristics each at some nearly instantaneous magnetic field strength for one period of the magnetic field oscillation. This set of current-voltage characteristics are then fit with a RSJ model in an analytic program to extract an I_C value at some magnetic field strength that is averaged over the time period it took to capture that current-voltage curve (in our example .1 sec).

This method is a more fundamental technique to measure the I_C modulation in comparison to the voltage-applied magnetic field characteristics since it directly measures the modulation of the critical current. This is also an accurate way to measure the overall critical current and the excess current. It is often not valid to rely on just current-voltage characteristics to determine device I_C, since a presence of residual fields can suppress the I_C in comparison to the I_C in absolute zero magnetic field. Critical current-applied magnetic flux characteristics of a Josephson junction would resemble Fig. 2.14, which depicts

a Fraunhofer diffraction pattern typical for small sandwich style Josephson junction I_C modulation.

3.4.5 Differential Conductivity-Voltage

Differential conductivity-voltage characteristics yield a direct measurement of the density of states of a material. In superconductors, BCS predicts an energy gap where quasi-particles are paired and condense into the superconducting ground state. At zero voltage, there is a highly degenerate set of states, which is characterized by the Josephson equations. Above the energy gap there is quasi-particle tunneling, by directly measuring the differential conductivity of a junction with a high-quality insulating barrier it is possible to accurately characterize these two phenomena at energy scales with several orders of magnitude difference.

Once again, the initial setup resembles the current-voltage characteristic method. Instead a slowly oscillating drive signal (.05 Hz) has a small fast oscillating signal added to it (some prime number $\sim$2000 Hz). Now the voltages across the current-measuring resistor and the DUT are split across four SR560 preamplifiers. Two signals from each respective source are directed to preamplifiers that have low-pass filters (300 Hz with 12 dB/oct rolloff) which only measure the slowly oscillating signals, so that the current-voltage characteristics are simultaneously recorded. The other two signals are sent to preamplifiers with bandpass filters with a high-pass filter at 1 kHz and low-pass of 10 kHz each with 6 dB/oct rolloff. This selects the high-frequency signal while rejecting the slow oscillation signal. The outputs are each input into two different lock-in amplifiers. Since the fast oscillating signal frequency is much greater than the drive signal the outputs of the respective lock-in amplifier yields

the instantaneous differential current and voltage respectively. The four signals from the two preamplifiers and the two lock-in amplifiers are input to the analog-to-digital converter to be processed by a Labview program. The ratio of the the differential current with the differential voltage yields the differential conductivity which then can be plotted against the drive signal voltage. The schematic representation of this system is shown in Fig. 3.21.

3.4.6 Noise

Spectroscopic noise measurements are necessary for engineers to characterize the minimum limits to which a sensor can detect. Furthermore, they can be informative to physicists to characterize the nature of the noise sources in a system. In an engineering application it is often most practical to operate the device in nominal conditions then pass the output signal to a signal analyzer that will perform a Fourier transform and decompose the magnitude of the noise sources to the frequency space. For example, a SQUID is often locked via a flux-locked loop electronics and the noise is measured from the output of that device. Alternatively, for physics purposes it might be necessary to bias the device into the working state with purely battery operated, analog electronics to limit possible noise sources to characterize just the DUT itself.

In either case, the DUT is prepared into a working state specific to the nature of the device and its output is directed to a Hewlett Packard 3562A Dynamic Signal Analyzer, which performs the spectroscopic decomposition. The data is then sent to the computer via a GPIB connection and organized via a custom Labview program.

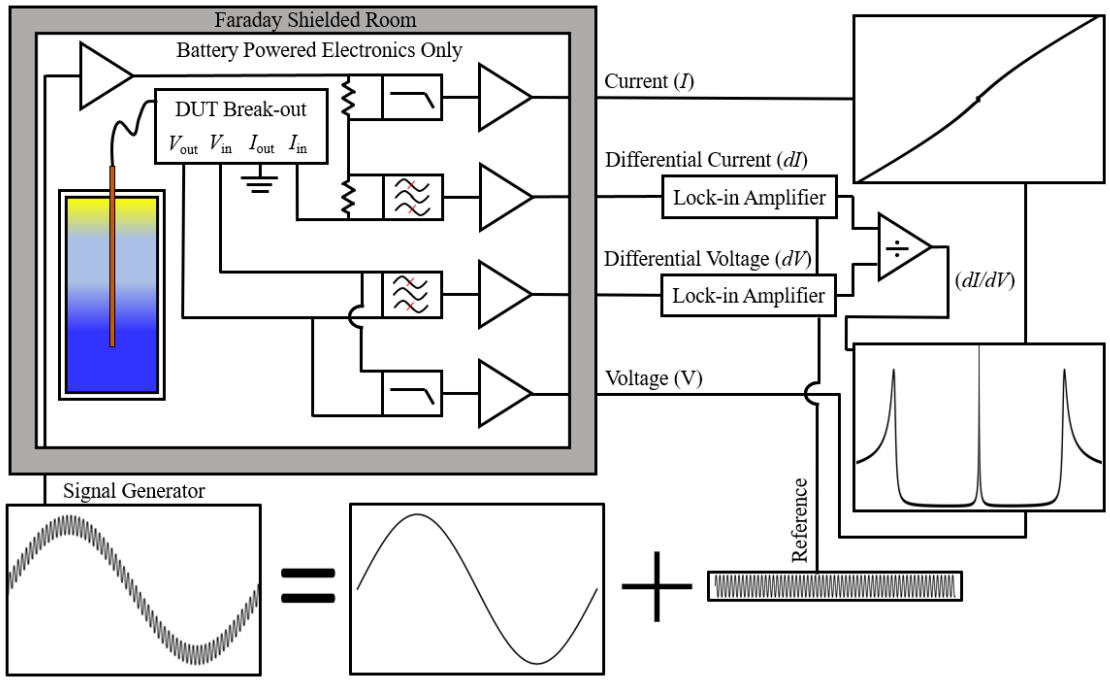

Figure 3.21: Schematic of the differential conductivity-voltage experimental setup. The measurement takes place within a Faraday shielded room (referenced by gray rectangle) containing only battery-powered electronics to reduced noise. The chip is loaded on a dip-probe insert (orange rectangle) and cooled in a liquid helium Dewar (blue/yellow gradient rectangle). A signal consisting of a low frequency oscillation modulated with a high frequency oscillation is generated and passed to a custom amplifier circuit and then to the sample through a breakout box that can connect to the insert and organize the input and output signals. Output signals are directed through a series of filters and amplifiers and, measurement depending, a lock-in amplifier and consequently passed to an analog-to-digital converter for analysis completed on a computer. BCS theoretical representations of the I-V and dI/dV characteristics are plotted on the right with their associated signals.

3.4.7 Two-Tone Spectroscopy

Two-tone spectroscopy is a method that can be used to characterize the linearity of the output of a device. Josephson devices are inherently non-linear to applied magnetic field. It is useful for sensing purposes for the output to be linear to simplify the transfer function. Consequently, the linearity of the device can be characterized by utilizing trigonometric identities for the product of two mixed oscillating signals.

$$\cos\theta\cos\varphi = \frac{1}{2}[\cos(\theta-\varphi)+\cos(\theta+\varphi)] \tag{3.3}$$

When mixing two signals in a device with a non-linear behavior we would then suspect two peaks in the spectroscopic readout at the sum and difference of the frequencies of the two applied signals. This test could be applied to a detector element by treating it like a mixer. If the side bands appear at the predicted sum and difference frequencies in the spectroscopic decomposition it suggests a non-linear readout. The spectroscopy can be performed as outlined in the previous section.

Chapter 4

Josephson Devices via Helium Focused Ion Beam

With the development of directly-written Josephson junctions, it is important to establish its application to prior-art designs of Josephson devices. There is motivation to demonstrate the ease of the fabrication technique, as well as, its ability to operate at comparatively high temperatures. Additionally, it is important to develop novel devices that take advantage of the technique. In this chapter, several prior-art and novel Josephson devices are demonstrated via focused helium ion beam microscopy.

4.1 Single Directly-Written Josephson Junctions

4.1.1 Metal-Insulating Transition of the Josephson Barrier

The strength of directly-writing Josephson junctions in cuprates via focused helium ion beam microscopy is that the Josephson junction parameters are very tunable. For

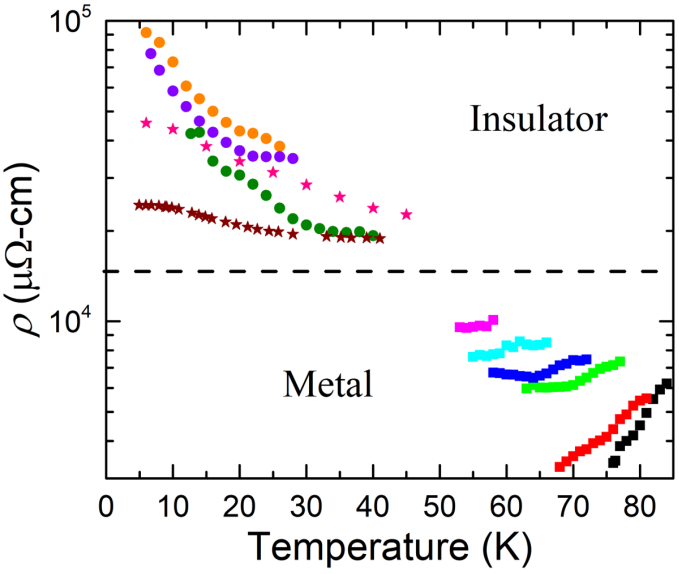

Figure 4.1: Josephson barrier resistivity (ρ ($\mu\Omega$ cm)) vs. temperature (K) for doses 1, 1.5, 2.0, 2.5, 3.0, 3.5, 4.0, 6.5, 7.0, 7.5, and 8.0 $\times 10^{16}$ ions/cm^2. The dotted line indicates the metal to insulator transition.

example, the strength of the Josephson barrier may be controlled with ion dose. To compare Josephson junctions with varying doses, a 20 Bridge sample was fabricated and Josephson barriers were written with doses from 1×10^{16} to 8×10^{16} ions/cm^2.

A series of I-V characteristics were taken for each Josephson junction while varying temperature. The characteristics were fit with the RSJ model to extract the normal state resistances and converted to resistivity by assuming the lithographically defined dimension of the film (4 μm), the barrier length (3 nm), and film thickness (35 nm). The Josephson barrier resistivity ($\mu\Omega$ cm) is plotted against temperature (K) in Fig. 4.1. Below the dose of 4.0×10^{16} ions/cm^2 we observe the characteristic behavior of metallic materials, and above it insulating behavior is observed. However, around 4.0×10^{16} ions/cm^2, near the

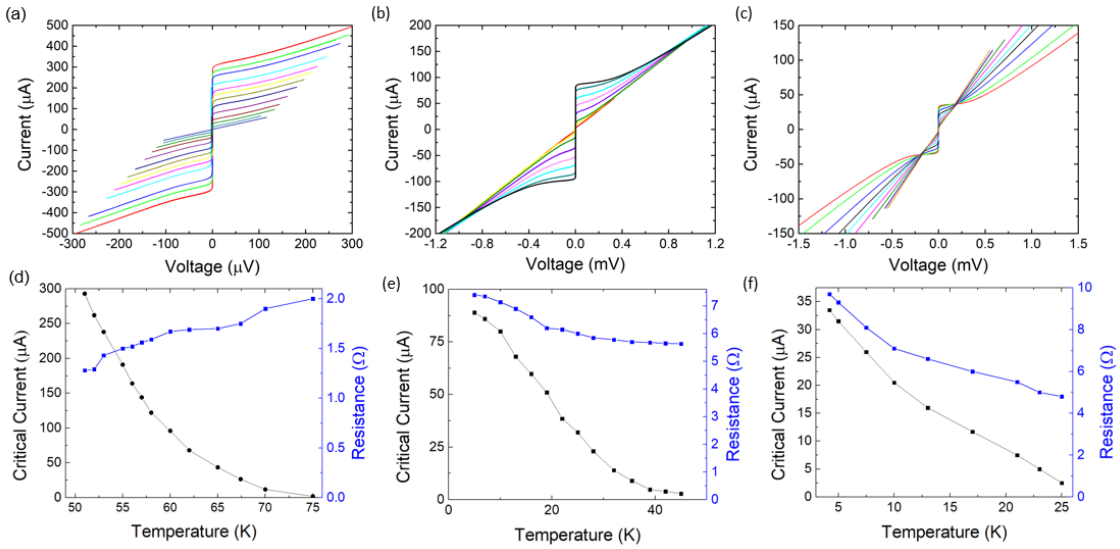

Figure 4.2: Current-voltage characteristics for (a) SNS (b) near metal-insulator transition (c) SIS directly-written Josephson junctions. Temperature dependence of I_C and R for (d) SNS, (e) near transition, and (f) SIS.

metal-insulator transition, we observe Josephson barriers with resistivities that are nearly temperature independent. Select I-V characteristics for an SIS, SNS and barrier near the metal-to-insulator transition are plotted for various temperatures in Fig. 4.2. The Josephson junction that features resistivity near the metal-insulator transition (4.0×10^{16} ions/cm^2 dose) is nearly temperature independent over a 40 K range.

Hence, by varying the ion fluence to the barrier it is possible to tune the behavior of the Josephson junction. Note that this dose influences the typical I_C and R values of the Josephson junction. Additionally, the dose effects the optimum working temperatures. Typically, SNS direct-written Josephson junctions operate at or above $T_C/2$, while SIS tend to work below $T_C/2$. It is observed that SNS junctions tend to have more excess current than SIS-type junctions, which agrees with the model from Ref. [47]. In this way, ion fluence is an important parameter that can be tuned for optimization for a particular application.

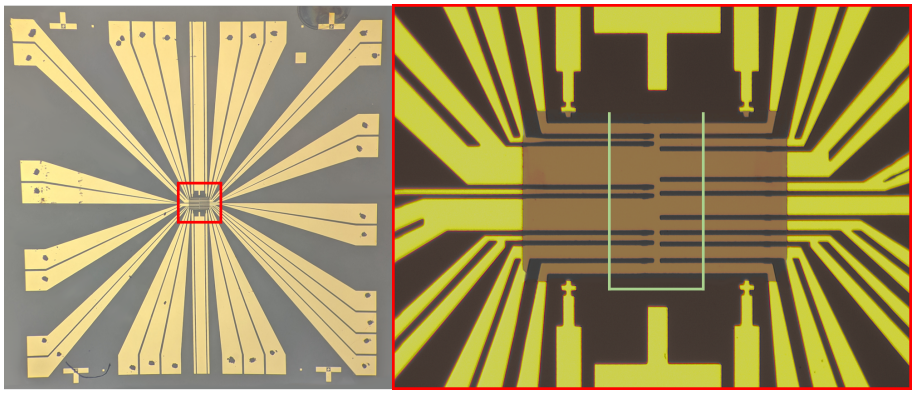

Figure 4.3: Optical image of the geometry for the sample investigating flux-focusing in planar Josephson junctions. Right is a zoom in on the focused ion beam writefield. Green line indicates the scan line for the irradiated region.

4.1.2 Flux-Focusing

There are restrictions in film thickness, determined by the penetration depth of the ion beam, and junction barrier length, by the desire to localize the Josephson barrier to the smallest length scale to ensure high-quality Josephson junctions. Consequently, the only dimension that may be readily tuned is in the $\hat{y}$-direction, based on geometry of the Josephson junction from Fig. 2.12. A design layout inspired by the 20 Bridge was developed with varying l, from 3 μm to 30 μm, to explore the flux-focusing effect in direct-written planar Josephson junctions (See Fig. 4.3). The sample layout allowed for the writing of each Josephson junction simultaneously. Additional samples were fabricated with junctions featuring l values up to 80 μm to test for upper limits of planar Josephson junction geometry.

The samples were irradiated with typical SNS junction doses and cooled to ~41 K for characterization. R and I_C values were estimated via RSJ model fits. I_C was determined from the maximum modulation of I_C-B characteristics. These parameters are plotted against l in Fig. 4.4. The junction resistance scales as expected. However, the I_C

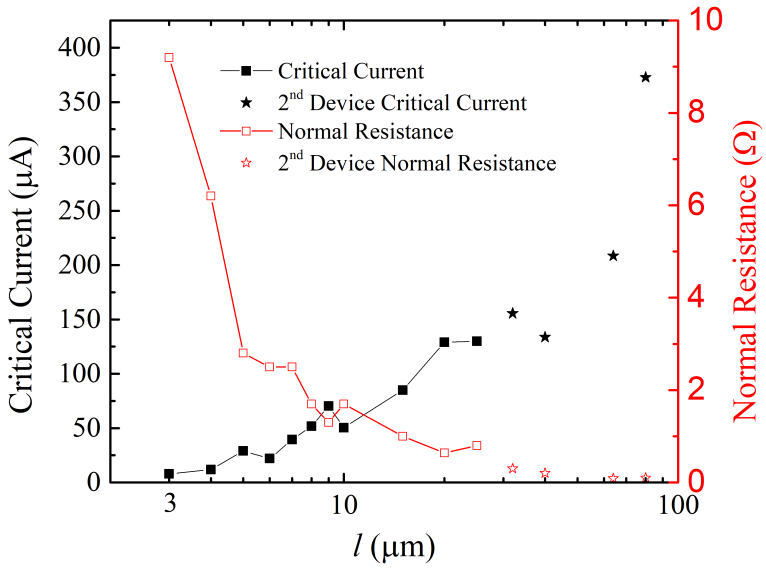

Figure 4.4: Single planar Josephson junction parameters critical current (left axis) and resistance (right axis) vs. width. Square and star shaped data points are from the same respective sample.

current is expected to saturate for $l > 4\lambda_J$, as all the supercurrent is screened to the edges. This saturation of the supercurrent is not measured up to a value of 80 μm. In YBCO planar junctions, it is estimated that λ_J is approximately 4 μm. It is expected that the scale of this experiment should have captured the transition from the short to the long regime. I_C-B characteristics of each junction were also taken. Care was taken to avoid flux trapping by first warming above T_C before slowly cooling to the measurement temperature for each junction. While the sample was magnetically shielded with a mu-metal can, there was an estimated -12.3 $\pm$ 4.3 μT residual field.

Examples of junction I_C-B for junctions with l equal to 9 and 20 μm are plotted in Fig. 4.5. To estimate the current density inside the junction, Fourier analysis was utilized.

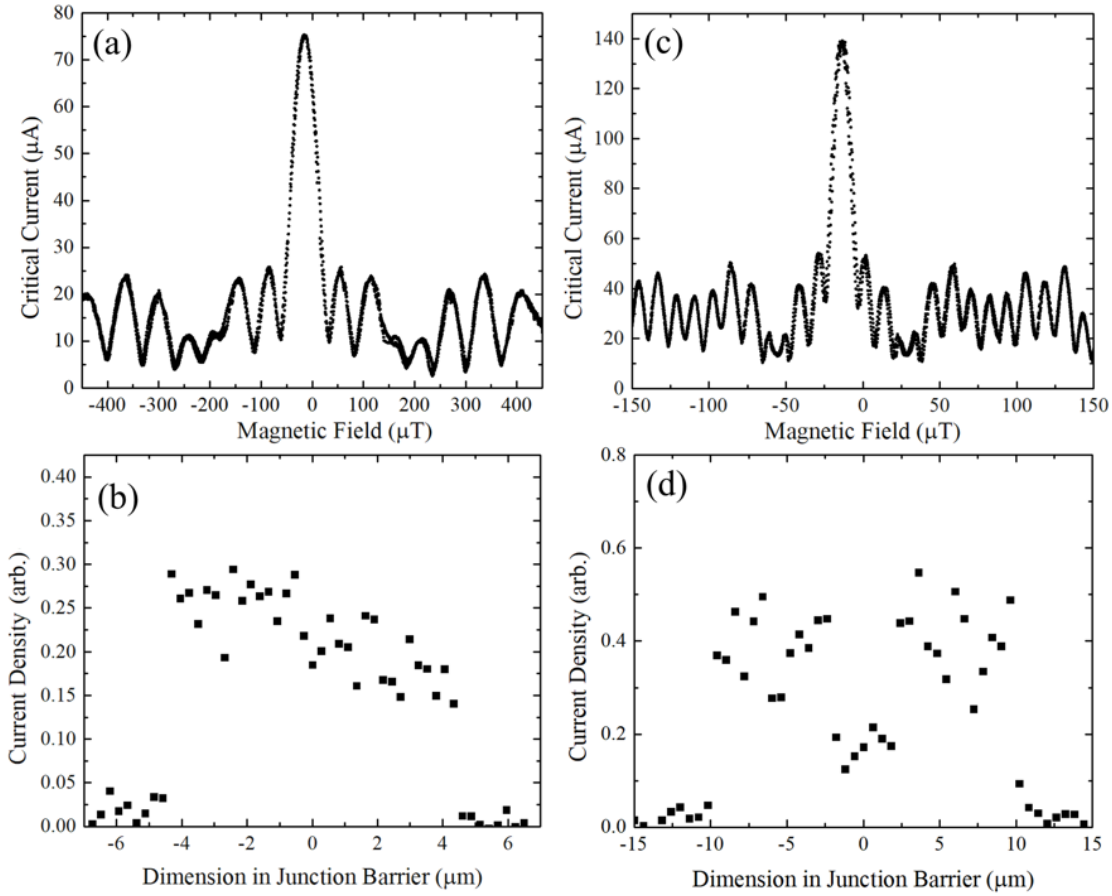

Figure 4.5: Example of critical current-applied magnetic field characteristics (a and c) and corresponding Fourier transforms (b and d), which estimate current density in the Josephson barrier. (a) and (b) indicate characteristics for Josephson junctions with l equal to 9 μm. (c) and (d) are for the 20 μm junction.

Since both phase and sign data is lost in the capture of the critical current modulation by an applied magnetic field, we attempted to utilize a phase retrieval algorithm to recover some information, known as the Gerchberg-Saxton algorithm. In this method, a target comprising of the estimated current distribution in the junction is first Fourier transformed to estimate the phase component. This phase times the measured I_C modulation may be inverse Fourier transformed to estimate a new current density in the junction. This process can be iterated upon thousands of times to produce an estimated current density in the junction calculated by the measured I_C modulation and a phase retrieved by the algorithm.

Using the symmetry arguments and the Meissner effect, it is argued for planar junctions in the long regime the current is screened from the center of the junction and current is concentrated at the edges. We provide the Fourier transform of this predicted current distribution compared against a uniform distribution in Fig. 4.6. These current distributions capture the same effects we observe in Fig. 4.5a and c. When the current becomes screened from the center it creates a secondary modulation of the sideband peaks. Additionally, for an uneven current distribution the Fourier transform captures the raising of the minima associated with the zero-bias peak. Finally, the inclusion of current in the center of the junction makes the sideband peaks more pronounced and could explain why the I_C does not saturate in the long regime. These targets are used to estimate the distribution of the current densities plotted in Fig. 4.5c and d. These figures indicate that the current is screened to the edges of the 20 μm junction but not the 9 μm one. However, there is some current density predicted inside the screened region of the 20 μm junction. Furthermore, there appears to be some deviation in current density magnitude across the 9 μm junction,

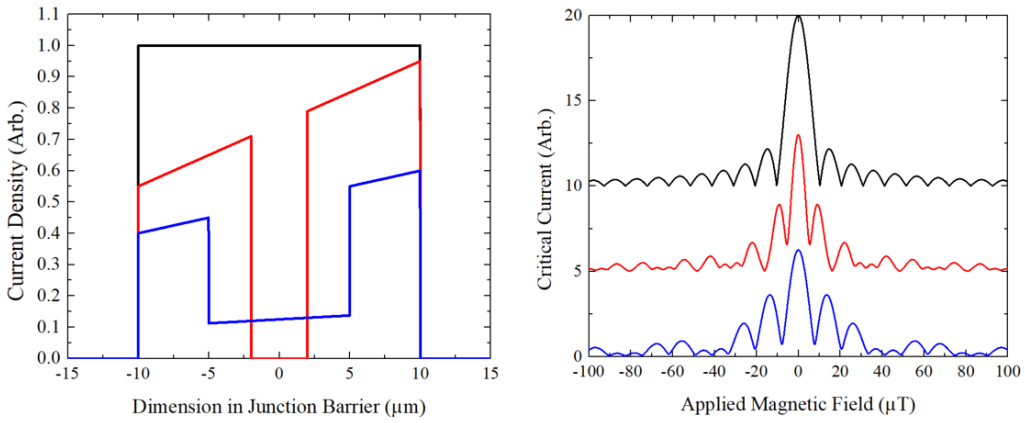

Figure 4.6: Predicted current density distribution in the Josephson barrier and their Fourier transforms. In the I_C-B characteristics, each is offset by 5 for clarity.

but not significantly in the 20 μm one. Note that this analysis is limited by the number of periods in the I_C-B characteristics and due to the loss of phase and sign data. Hence the analysis was limited to junctions with higher widths where it was possible to resolve enough periods given the limitations in our measuring system.

From the I_C-B characteristics the diffraction period was estimated by extracting the magnetic field between localized minima and averaging them together. Furthermore, treating each junction like a magnetometer, the transfer function, termed sensitivity, was estimated for each. The sensitivity is estimated by taking the linear fit of the maximally sloped portion of the zero-field peak in the I_C-B characteristic that maximizes the region in which the fit is greater than .999 Pearson correlation coefficient and then multiplying it by R. The Josephson junction diffraction modulation period and sensitivity are plotted against l in Fig. 4.7. In this figure, the diffraction period is compared to the predication from Ref. [54].

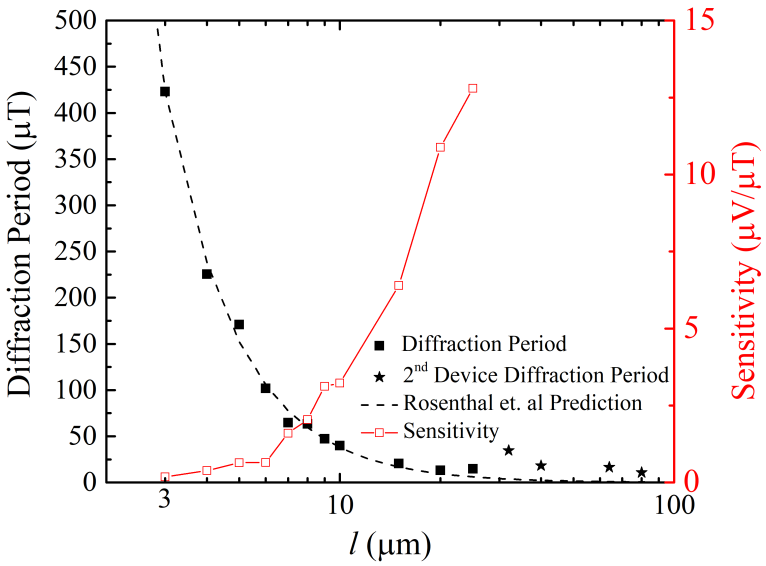

Figure 4.7: Dependence of magnetic field modulation (left axis) and sensitivity (right axis) vs. Josephson junction width. Theory flux-focusing dependence is given by dotted line.

In the original sample, with electrodes with l up to 30 μm, the junction on the 30 μm electrode did not exhibit I_C modulation. An additional sample was fabricated testing electrodes with $l > 30$ μm and up to 80 μm to test whether there was an upper limit. In this test we were able to confirm the Josephson effect via I_C modulation in junctions with l up to 80 μm. Despite R scaling as expected, the I_C did not saturate as theory predicts. This could be a result of trapped flux or microshorts in the system. Whatever, the cause, this behavior was reproducible across two samples and practically provides another tunable knob for controlling the I_C and R values of the Josephson junction.

Additionally, we observed irregularities in the interference pattern. It deviated significantly from the traditional Fraunhofer pattern. A significant portion of this may be explained by differences in geometry. However, we also observed a beating like behavior of

the localized maxima of the side band peaks. There are several effects in superconductivity that can explain this phenomenon, making it difficult to disentangle and isolate the specific cause. This may be primarily explained by nonuniform currents inside the barrier due to the screening of the current to the edges of the sample by the Meissner effect. But, also, is due to the effect that prevented the saturation of the I_C at high l, which could be the result of deviation in the Josephson barrier. Moreover, deviation from the Fraunhofer diffraction pattern could be result of self-field effects common in Josephson junctions in the long regime.

4.1.3 HBCO

The yttrium in the YBCO lattice structure is easily substituted by rare earth elements. This substitution with a heavier element is thought to induce strains in the lattice that may effect the superconducting state [143, 144, 145]. Here we investigate substitution of the yttrium element with holmium to form $HoBa_2Cu_3O_{7-\delta}$ (HBCO) thin films via reactive sputtering elaborated in Sec. 3.2.2. It is predicted that the large ionic radius of holmium will tightly bind the lattice and lead to a more homogeneous crystalline film. Here we will demonstrate directly-written Josephson junctions in a HBCO thin film deposited by my colleague Stephen McCoy [139].

A 55-nm thick film of HBCO was grown on LSAT and featured a T_C of 88 K and a critical current density of 3 MA/cm^2 at 77 K. The film was patterned into a layout with 2 μm wide electrodes and junctions were directly-written via focused helium ion beam with doses equivalent to YBCO. The transport properties of an example Josephson junction can be viewed in Fig. 4.8. The example Josephson junction features an I_CR value of 150 μV.

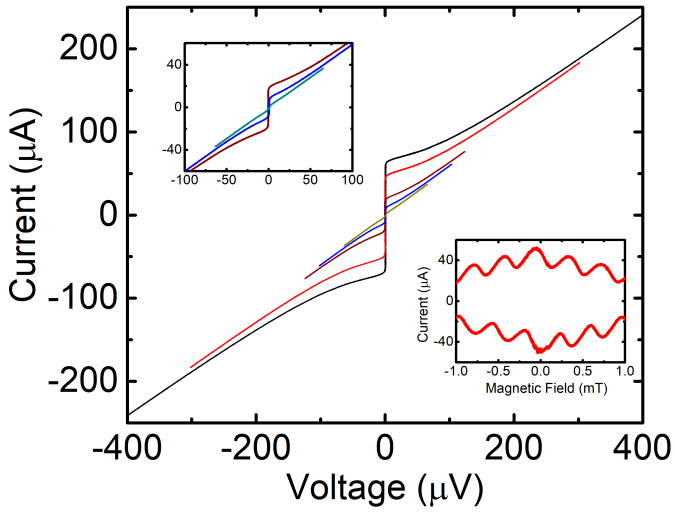

Figure 4.8: Transport properties of a HBCO Josephson junction. Greater image is current-voltage characteristics from 54 to 31 K. Lower inset is critical current-magnetic field depicting the Josephson interference pattern. Upper inset is zoom in of the current-voltage characteristics on the higher temperature range.

HBCO is an important alternative cuprate superconductor that we have demonstrated is also compatible with lithography via focused helium ion beam microscopy. It features a higher transition temperature comparing to YBCO and may be a promising candidate for Josephson circuits. Importantly, it offers another candidate for investigation into the order parameter in cuprate superconductors.

4.1.4 BSCCO

The prospect of coupling naturally occurring *c*-axis orientated intrinsic Josephson junctions with *a*-*b* planar junctions in BSCCO for multi-dimensional Josephson circuits is a strong motivation for investigation via helium ion microscopy. Moreover, BSCCO, as a van der Waals material, may be mechanically exfoliated producing single crystal samples that do

not suffer from the same defects that occur in grown thin film cuprates. My colleague Yan-Ting Wang developed a process for producing samples of exfoliated single crystal BSCCO and depositing electrode contacts with minimal interfacial resistance [146].

The exfoliated samples featured a T_C of 82 K. Additionally, it was possible to directly measure the intrinsic Josephson junctions with this technique. Fig. 4.9 includes characterization for an example of one of these samples. These exfoliated samples were $\sim$50 nm in thickness and are ideal for characterization via focused ion beam microscopy. Fig. 4.9a demonstrates the typical geometry of a directly-written BSCCO Josephson junction. The junction width (l) is set by two lines written with an insulting dose that prevents electrical transport across. The junction is written between and parallel to those insulating lines. In general, the BSCCO was more sensitive to applied ion fluence but did not differ significantly from that of YBCO behavior to applied ion dose.

Several samples were fabricated and irradiated with varying doses and the metal-insulation transition in the Josephson barrier is observed. Fig. 4.10 demonstrates current-voltage characteristic dependence on temperature for various doses of junction irradiation that feature each phase of the metal-insulator transition. The SNS junction was written into a 80-nm sample with 6×10^{16} ions/cm^2. The junction width was defined via helium ion microscopy to be 8 μm. The normal state resistance is less than 1 Ω and from the I-V characteristics appears to have significant excess current. The junction near the metal-insulator transition features normal state resistances between 12 and 15 Ω over a temperature range of 35 K. The SIS junction was fabricated on a 55-nm thick sample to have an l of 4 μm with an ion dose of 7×10^{16} ions/cm^2. At 4.2 K this Josephson junction features an $I_C R$

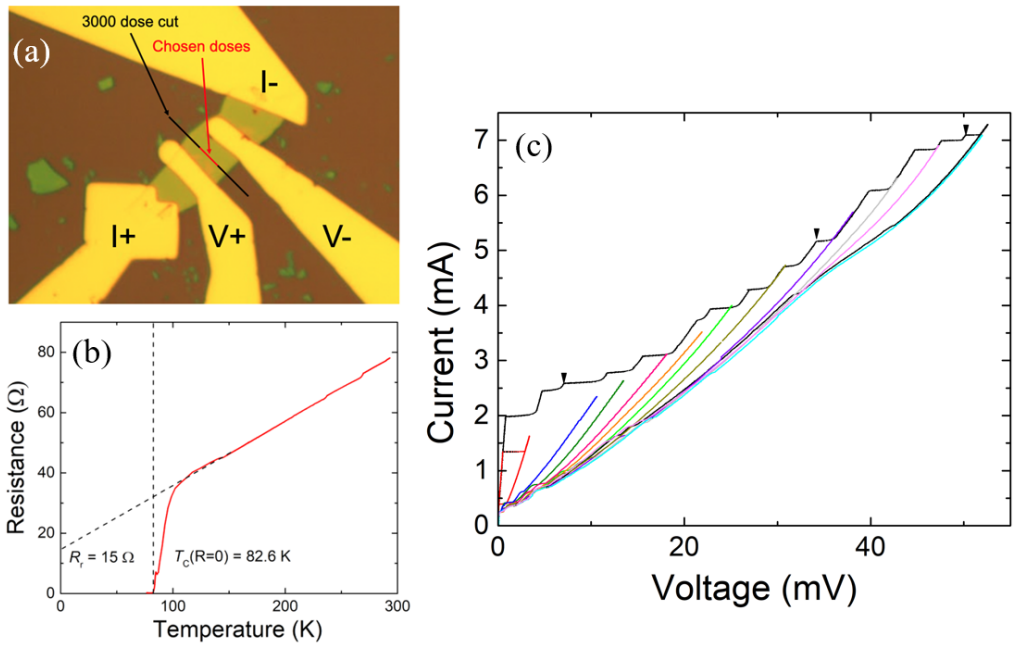

Figure 4.9: Example of an exfoliated single crystal BSCCO sample with 4 low interfacial resistance contacts. (a) Optical image with indicated insulating (black line) and Josephson junction (red line) regions for helium ion fluence irradiation. (b) is the resistance-temperature dependence of this sample. (c) are intrinsic Josephson junction current-voltage characteristics in the unwritten BSCCO sample. Black triangles indicate hysteretic curves that were not captured [146].

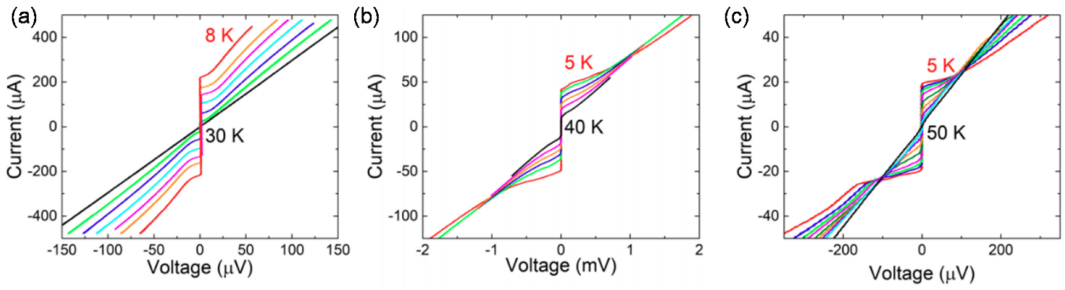

Figure 4.10: Current-voltage characteristics of exfoliated BSCCO for several doses that demonstrate the metal-insulator transition in direct-written Josephson barriers. Barriers that behave (a) as a metal, (b) near the transition, and (c) as an insulator.

product of 160 μV.

In order to test for the Josephson effect in the directly-written junctions and differentiate them from the intrinsic ones, a magnetic field was applied normal to the c-axis. The critical current-applied magnetic field characteristics are shown in Fig. 4.11. Through analysis of the period of the I_C modulation we were able to compare the effective junction area with the actual junction geometry. These values were in agreement and suggest that the direct-write method is appropriate for BSCCO, as well. Using flux-focusing methodology for planar style junctions, the effective l of the SNS junction is predicted to be 9 to 11 μm and the SIS junction effective l is estimated to be 3-4 μm. As expected there is a significant decrease in the amount of excess current observed as the Josephson barrier transitions to an insulator.

4.1.5 Tunable Josephson Junctions

In addition to varying the dose of ion fluence to define the Josephson barrier, the direct-write technique can make novel geometries to tune the parameters of the Josephson

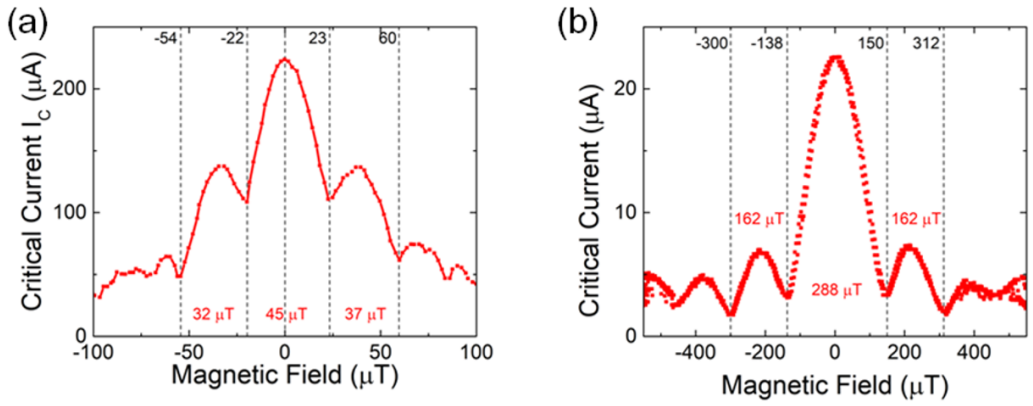

Figure 4.11: Critical Current-applied magnetic field characteristics of exfoliated BSCCO for (a) SNS and (b) SIS junctions.

junction. Resistor and capacitor geometries can be directly-written in parallel with the junction to modify its properties.

For example, it may be desirable to lower the normal state resistance of a junction while maintaining an insulating barrier for impedance matching. It is possible to direct-write a resistor in parallel with the junction as indicated by the geometry in Fig. 4.12a. The effective resistance (R_{eff}) of such a device is given by the following:

$$\frac{1}{R_{eff}} = \left(\frac{1}{R} + \frac{1}{R_{\square}(L/W)} \right) \tag{4.1}$$

where $R_{\square}$ is the sheet resistance of the yellow region that is ion irradiated and L and W are defined as given by Fig. 4.12a. In this case it is desirable to choose a dose for ion fluence of the parallel resistor near the metal-insulator transition to ensure that the response is temperature independent. Utilizing the data from Fig. 3.2, it is estimated that the $R_{\square}$ would be 86 Ω for a target dose between 16 and 40 ions/nm^2.

An example I-V of this type of Josephson junction is presented in Fig. 4.13. A Josephson junction with $l = 1$ μm was written with a typical SIS dose with a $L = 50$ nm

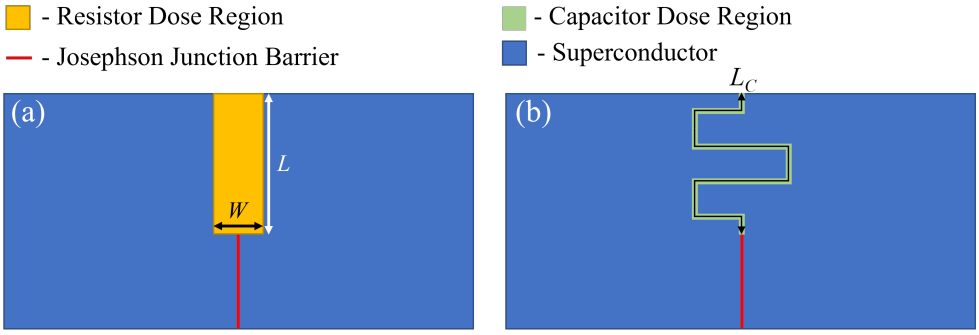

Figure 4.12: Representation of the directly-written Josephson junction and parallel resistor and capacitor geometry for tuning junction parameters. Red line indicates Josephson barrier. Yellow box indicates resistor dosed region. Green line indicates directly-written interdigital capacitor. Blue region indicates superconducting bulk electrode. (a) shows resistor geometry and (b) shows interdigital capacitor geometry both in parallel to the junction.

and $W = 3$ μm resistor directly-written in parallel. While this junction seems to feature low excess current, characteristic of devices with strong Josephson barriers, it features a resistivity of about an order of magnitude less than the typical SIS junctions of the same l. However, there is asymmetry in the I-V characteristics which may indicate the presence of trapped flux or could be a result of the adjacent resistor which may cause a deviation in the current density of the junction. More investigation is necessary. However, if this is a consistent issue, it may be fixed by defining the junction width with an insulating line.

It is also suggested that this method could be extended to define the capacitance of the Josephson junction by direct-writing interdigital capacitors in parallel with an insulating dose of ion irradiation. The geometry of such a device is presented in Fig. 4.12b. The effective capacitance of that device is estimated by the following:

$$C_{eff} = C_J + \frac{\varepsilon t}{d} L_C \tag{4.2}$$

where C_J is the junction capacitance, ε is the dielectric constant of YBCO, t is film thickness,

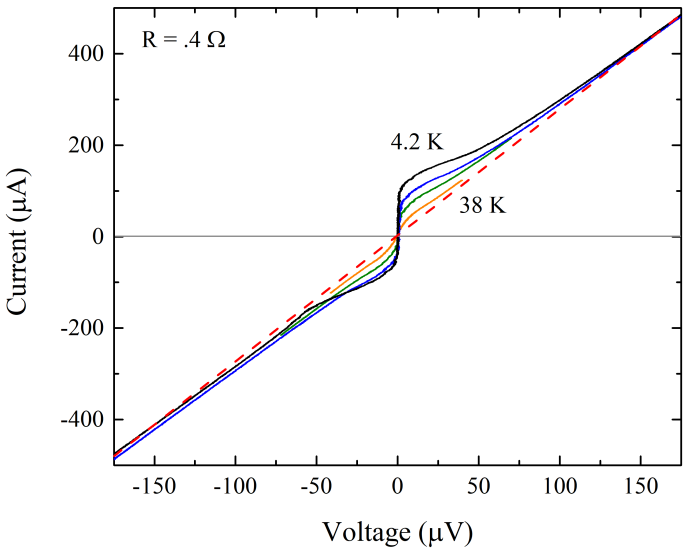

Figure 4.13: Current-voltage characteristics of a SIS directly-written Josephson junction with a directly-written resistor in parallel.

and d is given by the effective area of the spot size of the focused ion beam. And L_C is the effective length of the direct-written capactor as indicated in Fig. 4.12b.

Tuning these parameters via these methods is independent of all other Josephson junction properties. This suggests isolated control of these important parameters is possible, making this technique important for engineering Josephson circuits. As an example, it may be beneficial to have such isolated control of the junction capacitance for the fabrication of directly-written transmons for the direct tuning of the capacitance and E_J parameters.

4.2 SQUIDs

4.2.1 Nano-Slit

We can take advantage of the focused helium ion beam technique to miniaturize the size of SQUIDs. Instead of using lithography to define the SQUID loop, it is possible to use a direct-write of high ion fluence to define the SQUID loop. The geometry of this DC washer-style SQUID is in Fig. 4.14. This type of SQUID has been termed as a "nano-slit SQUID" because one dimension of the loop has been scaled to the nanoscale. A single line of insulating dose (6×10^{17} ions/cm^2) that is 20 μm long is written to define the SQUID loop. Two Josephson junctions are written in parallel with a typical SIS dose, 8×10^{16} ions/cm^2, and are defined to be $l = 2$ μm via two insulating lines. In this configuration, if we assume the two dimensional penetration depth ($\lambda_\perp$) to be 1.1 μm, the effective area of the SQUID loop is $2\lambda_\perp \times 20$ μm. This SQUID is coupled to a flux concentrator with an area of 30×30 μm^2.

The SQUID was characterized at liquid helium temperatures. The I-V characteristics can be viewed in Fig. 4.15a. The SQUID featured an $I_C R$ of 715 μV ($I_C = 65$ μA and $R = 11$ Ω). The characteristics resemble the RSJ model and indicate little presence of excess current. Voltage-applied magnetic field characteristics are displayed in Fig. 4.15b and c. The device was DC current biased at 68 μA. It is possible to view the junction and SQUID oscillations due to their respective intereference. The first junction minima occurs near 100 μT which predicts a junction width of 6 μm by the same analysis from Sec. 4.1.2. This may deviate from the expected 2 μm due to an additional flux focusing effect from the

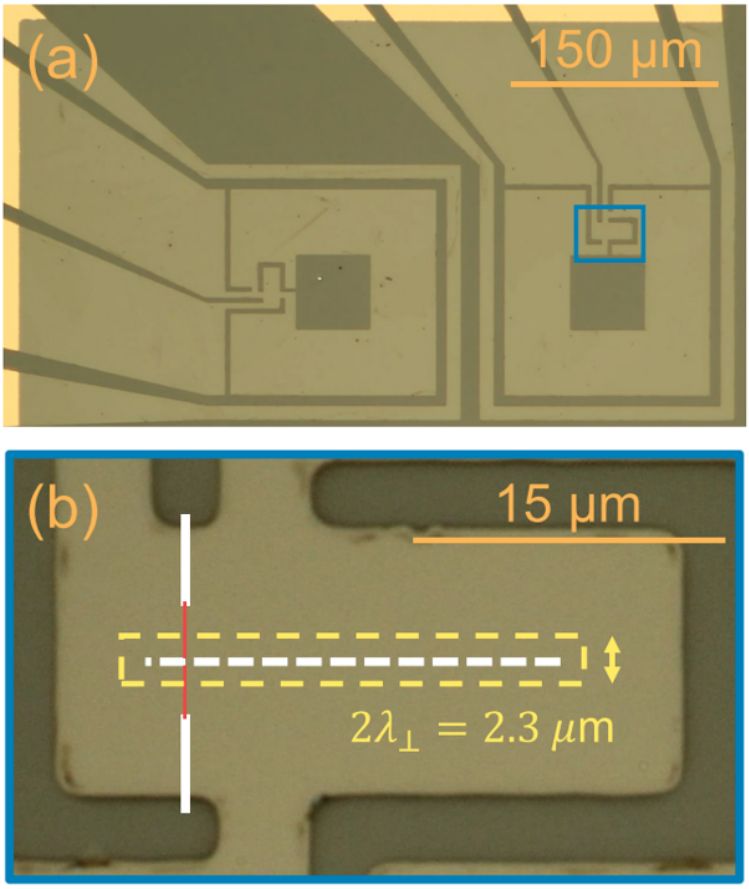

Figure 4.14: Optical image of a directly-written DC washer SQUID with the junction and loop geometry overlaid. (a) shows the entirety of two devices. (b) is a zoom in on the nano-slit SQUID. Red lines indicate Josephson junctions and their size is determined by two insulating regions indicated by solid white lines. The white dotted line indicates the insulting region that is the SQUID loop. The area the magnetic flux can penetrate is represented by the yellow dotted line [147].

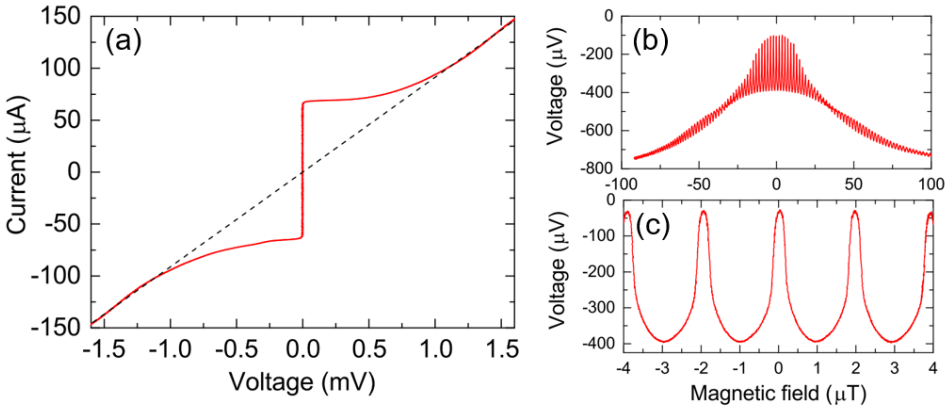

Figure 4.15: Transport measurements of the directly-written DC washer SQUID. (a) Current-voltage characteristics. (b) Voltage-magnetic field characteristics at a range to show both the junction and SQUID intereference modulations. (c) Voltage-magnetic field characteristics at a range to highlight the SQUID oscillations about the zero-bias peak [147].

geometry of the bulk electrodes. An additional modulation of the SQUID oscillations are observed, which maybe explained by the modulation of its own individual area.

The SQUID interference oscillations feature a modulation amplitude of ∼350 μV, corresponding to $1/2I_C R$. This suggests that $\beta_L \sim 1$, which corresponds to an inductance of 32 pH. The period is 2 μT/Φ_0 and the maximum dV/dB value is $\sim$ 2800 μV/μT.

Finally, the noise characteristics of this device were measured with a static applied field of .25 μT while the device was current biased into the normal state. The output spectrum is compared against the background noise in Fig. 4.16.

The important work from this section was conducted primarily by my colleague Ethan Cho [2]. It exhibits the versatility of the focused helium ion beam technique by demonstrating one of the most ubiquitous Josephson superconducting devices. It also demonstrates that these devices are well-behaved by conventional Josephson circuit theory.

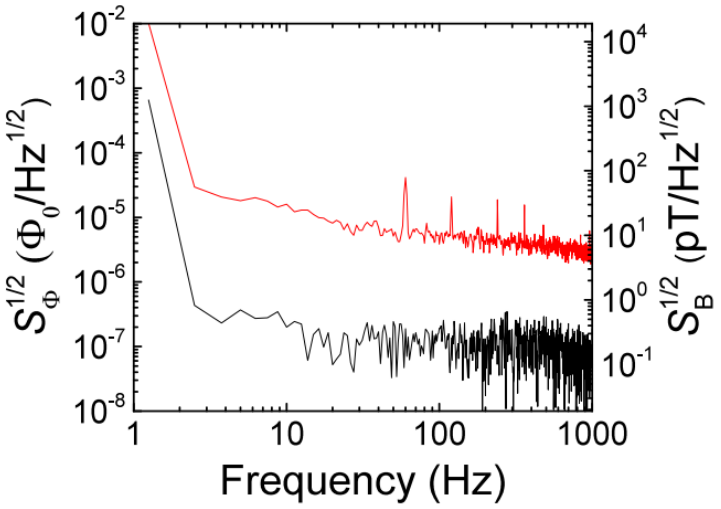

Figure 4.16: Noise Spectrum of the DC washer SQUID compared against the background noise without flux-locked loop electronics. Red line indicates SQUID noise spectrum, while the black curve yields the background baseline of the measurement scheme [147].

4.2.2 Nano

The natural progression from the preceding section is to progressively scale down the dimensions of the SQUID to a "nanoSQUID." This work was primarily conducted by my colleague Hao Li [148]. The geometry of the device is presented in Fig. 4.17. Junctions were written with l equal to 300 nm with typical SIS doses. Progressively smaller loop areas were patterned with a minimum size of 10 $\times$ 10 nm^2. A current I_M isolated by an insulating line was coupled to the SQUID as a control for the magnetic flux bias.

The SQUIDs were characterized at 4.2 K. Current-voltage and voltage-applied magnetic fields of the SQUIDs with loops with side dimensions of 10 and 50 nm are displayed in Fig. 4.18. These devices feature a very large voltage response to an applied magnetic field. The SQUID oscillation of these devices were so decoupled that a relatively large applied magnetic field was necessary to capture several periods. By analysis of the periodicity,

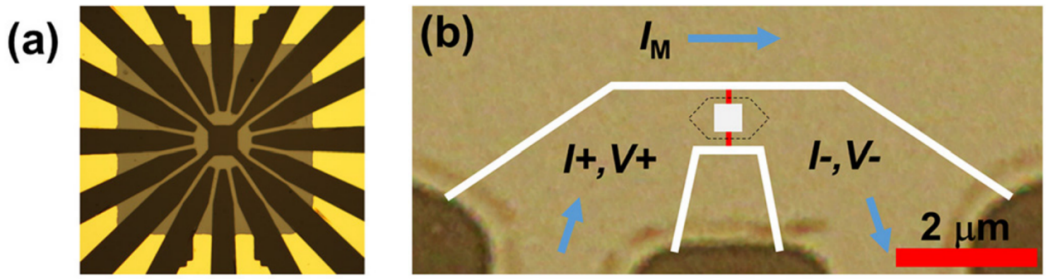

Figure 4.17: (a) Optical image of nanoSQUID bulk electrode geometry and (b) indicated directly-written SQUID lithography. Solid white indicates regions that are irradiated into the insulating state. Red indicates the Josephson junctions. Black dotted lines indicates area that the magnetic flux penetrates. Blue areas indicate transport measurement scheme of the device. A current (I_M) may be induced within nanometers of the device along a control line isolated by a single insulating line [148].

it was estimated that these SQUIDs have an effective area of .53 μm^2, which is in good agreement with the proposed magnetic flux penetration area as defined in Fig. 4.17b. Additionally, these devices featured a very large voltage response inspiring use as a 3-terminal transimpedance amplifier. The I_M current could be coupled to the nanoSQUID as a flux with a transfer function of $\sim$ 8.6 mA/mT, resulting in a transimpedance of about .1 Ω (See Fig. 4.19). In this state, only power is dissapated in the junctions while they are in the normal state. It is estimated that only 9 nW are dissipated by the bias current.

This was very inspiring work demonstrating the ability to scale down the dimensions of directly-written devices by using the focused helium ion beam irradiation to perform lithography for the entire device geometry. Furthermore, it has application as an energy efficient amplifier. Additional work was performed that characterized the performance of series arrays of nanoSQUIDs to improve the voltage response hoping to demonstrate a superconducting circuit with several volts response.

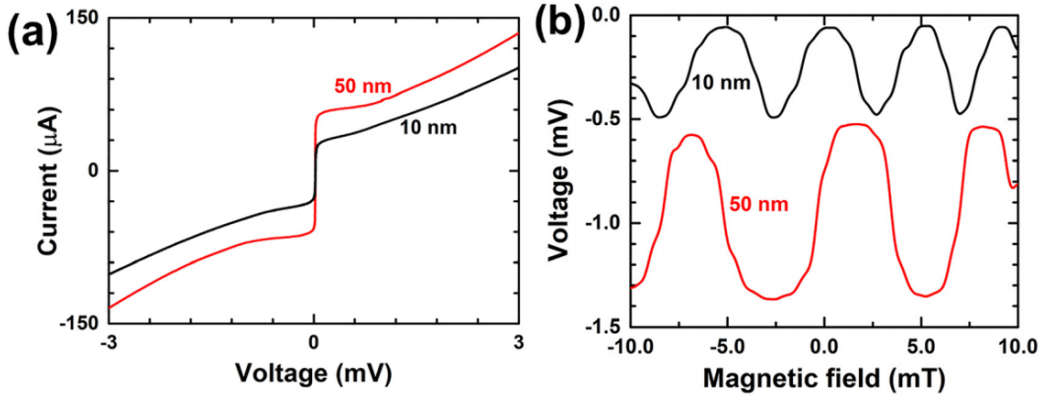

Figure 4.18: Transport measurements of two directly-written NanoSQUIDs. (a) Current-voltage measurement and (b) voltage-applied magnetic field. Black curve indicates loop with 10 nm side dimension while red indicates the 50 nm one [148].

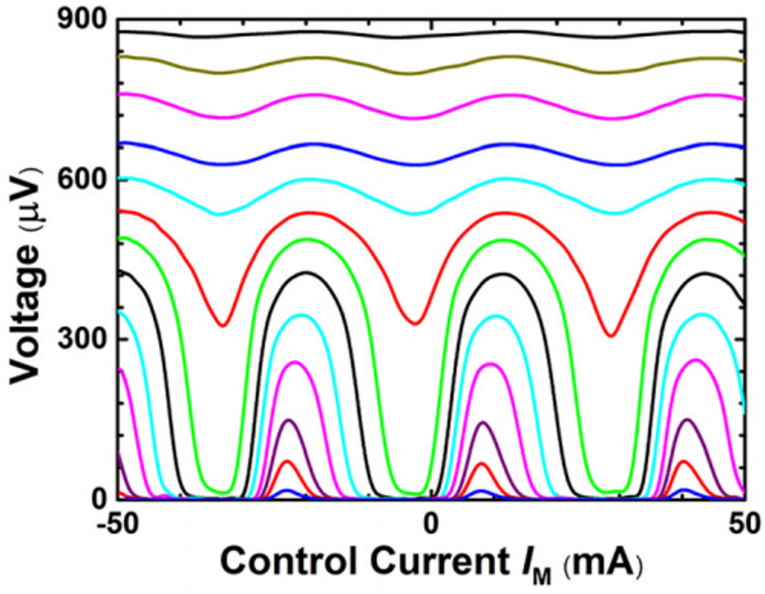

Figure 4.19: Transport measurements of directly-written NanoSQUIDs driven by the coupling current I_M. This is for the NanoSQUID with side dimension of 400 nm with DC bias currents from 8 μA to 17.5 μA [148].

4.2.3 Gradiometer

A gradiometer is a detector of the spatial gradients of magnetic flux. The generalized geometry of such a device includes two flux concentrator loops seperated by a dimension referred as the baseline. These loops are coupled to a SQUID that is sensitive to the relative difference of the total magnetic flux threading each of the two magnetic flux concentrators. The geometry the bulk superconducting electrodes for two gradiometers is displayed in Fig. 4.20a. A nanoslit SQUID would be directly-written between the intersection of the two circular concentrator loops, such that it was sensitive to the flux threading each circle. On-chip magnetic field control lines were designed concentric with these concentrator loops and designed to maximize mutual inductance. A finite-element simulation was done to estimate the coupling inductance between the concentrator loops and the on-chip control lines and is displayed in Fig. 4.20b. It is estimated that the concentrator loop has a mutual inductance of 540 pH to the concentric control line and a 232 pH mutual inductance to the opposite control line.

The devices were characterized at 60 K and their current-voltage characteristics can be viewed in Fig. 4.21. The junctions were written with typical SNS doses. Their voltage modulation to an applied current in the control line is presented in Fig. 4.22. The voltage modulation was a small percentage of the $I_C R$, which could hint that there is significant excess current and that the β_L is not close to ideal in this SQUID. From analysis of the voltage modulation period it is estimated that the effective mutual inductance that causes a relative magnetic flux gradient by the control loop to the flux concentrators in the

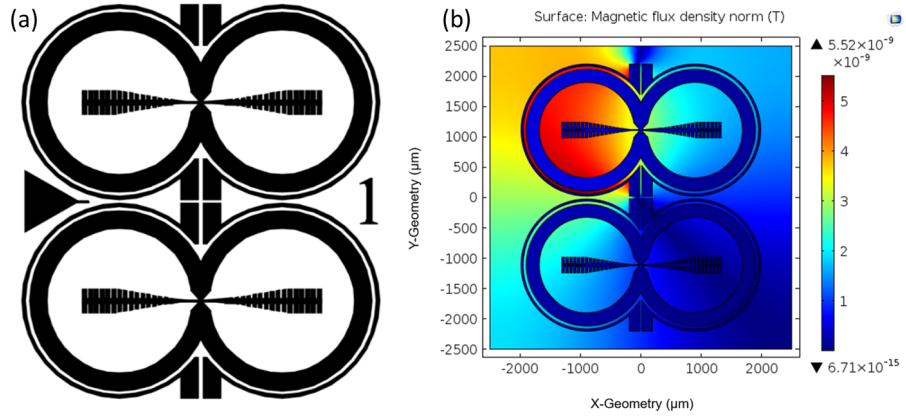

Figure 4.20: (a) A design layout image of the superconducting electrodes of the directly-written SQUID gradiometer. (b) Finite-element simulation of the mutual inductance to an on-chip magnetic control line, with current applied to the upper left control line.

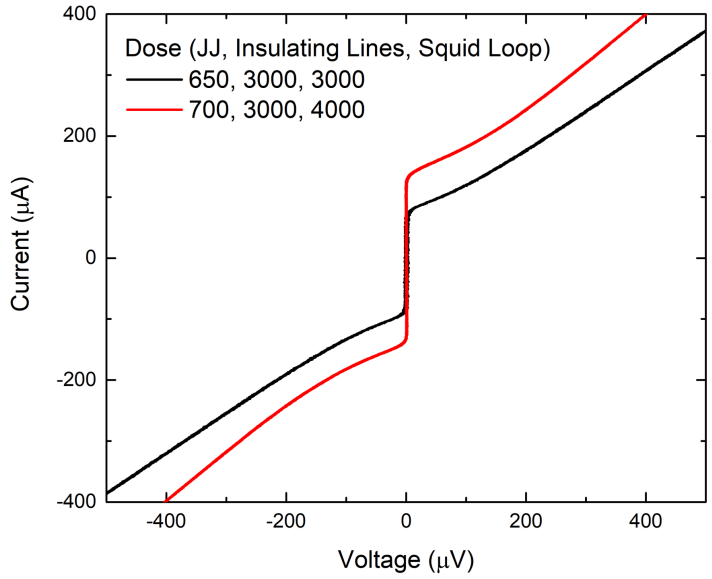

Figure 4.21: Current-voltage characteristics of two SQUID gradiometers at 60 K. Red curve is for junctions with 700 ions/nm dose and black curve for 650 ions/nm. Doses are indicated by line dose (ions/nm).

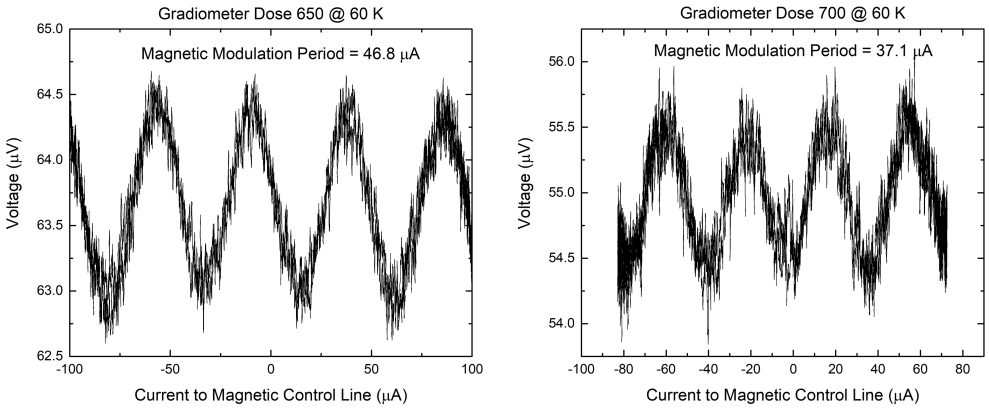

Figure 4.22: Voltage-magnetic control current bias characteristics of the directly-written SQUID gradiometers. Left is 650 ion/nm and right figure is for 700 ion/nm dose.

gradiometer is ∼50 pH.

4.3 Single Flux Quantum Devices

Digital electronics can be achieved in Josephson circuits using magnetic flux quanta as the basis for information, referred to as single flux quantum circuits (SFQ) [149]. Power dissipation in these circuits only occurs when there are phase slips in the Josephson junctions, and therefore they are highly energy efficient. Furthermore, they can be operated up to the energy gap of the superconductor, suggesting an equivalent operating frequency greater than 100 GHz. These circuits have many potential applications, including: memory, mixers, digital sensing readout, switches for routing, and high-speed, high-efficiency computing [150, 151].

In this section, we demonstrate a set-reset flip flop using fundamental SFQ circuit components in YBCO using the direct-write technique. We are motivated by the prospect

of higher operating temperatures and the potential to achieve higher speed operation due to the large energy gap values observed in cuprate superconductors. This work was primarily conducted by my colleague Han Cai [152].

The SFQ set-reset flip-flop circuit schematic is presented in Fig 4.23a. On the left the circuit consists of a DC to SFQ converter that launches a SFQ through a Josephson transmission line (JTL). The JTL transmits the SFQ pulse to a storage loop. This is the "Set" circuit. An equivalent circuit is mirrored and coupled to the same storage loop on the right, making up the "Reset" circuit. A DC SQUID is inductively coupled to the storage for state readout. The circuit was fabricated on a single layer of YBCO by direct-writing via focused ion beam irradiation. The optical image of the device geometry is presented in Fig. 4.23b.

The device was cooled to $\sim$20 K for characterization. The JTL was current biased at 75 μA. "Set" and "Reset" pulses were produced by an arbitrary waveform generator. The state of the storage loop was measured by biasing the DC SQUID into the voltage state with the magnetic flux tuned via direct current injection to a magnetically sensitive region in the V-B. The device output can be viewed in Fig. 4.24. It was observed that a input "Set" pulse induced a voltage modulation of 50 μV, which was then canceled out by the "Reset" pulse.

There was a second step present in the SQUID voltage pulse suggesting the presence of multiple SFQ in the storage loop. This could be result of a storage loop with a β_L greater than 2. Another possibility could be the result of the direct coupling of the input current to the readout SQUID. However, this mutual inductance should be very small and

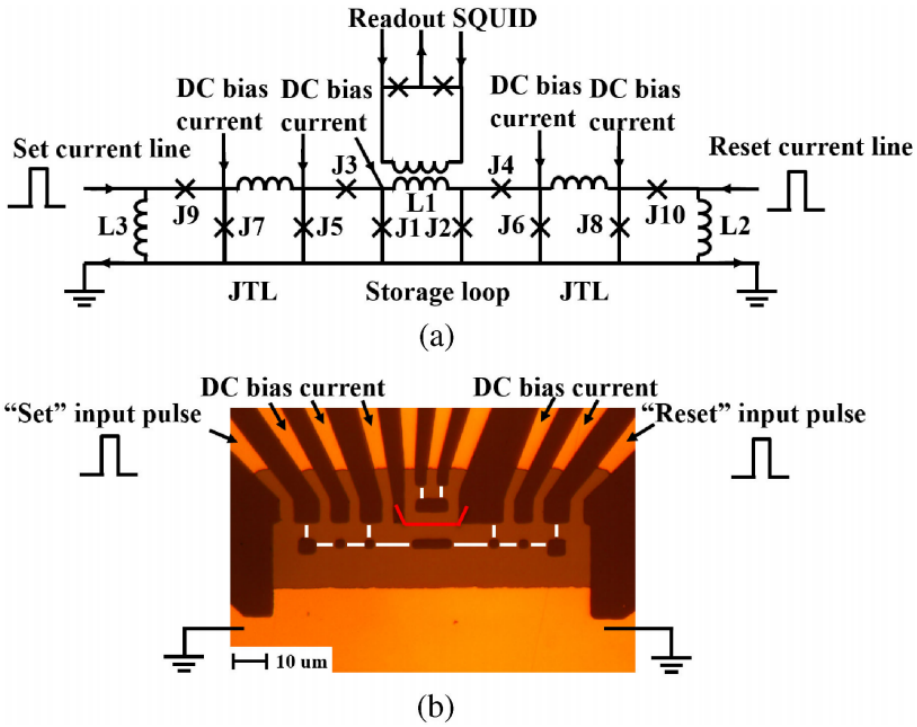

Figure 4.23: (a) Schematic representation of single flux quantum set-reset flip flop circuit. (b) Optical image of device geometry with overlaid direct-write ion irradiation pattern. The white lines indicate regions where Josephson junctions were directly-written and the red line indicates a heavy insulating dose that isolated the SQUID from the storage loop [152].

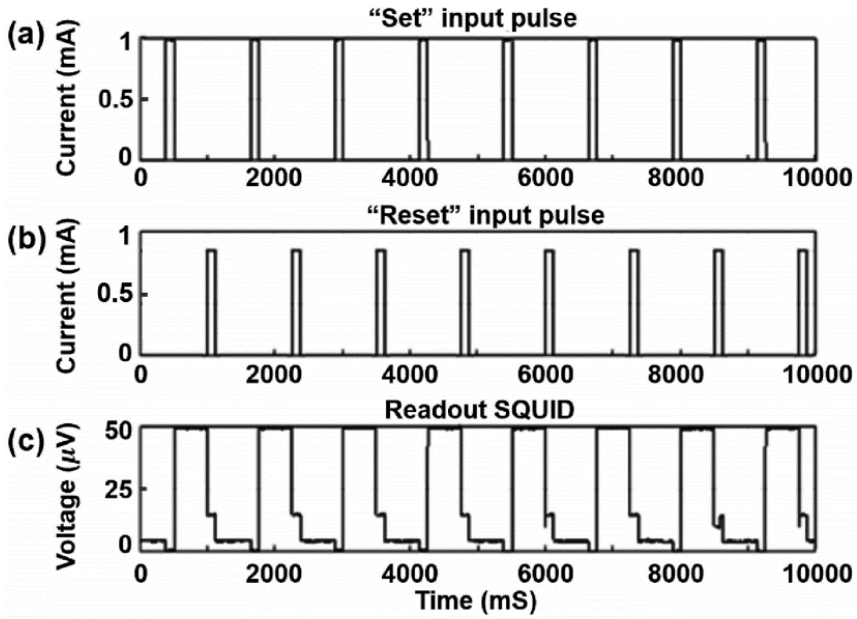

Figure 4.24: Demonstration of the single flux quantum set-reset flip-flop circuit. Each graph is in the time domain depicting (a) the input "Set" pulse, (b) the input "reset" pulse, and (c) readout SQUID voltage [152].

therefore inconsequential to the SQUID readout. Finally, another consideration is the direct coupling of the input current to the storage loop that bypasses the JTL. However, this was rejected since coupling in this manner was directly measured and found to require in excess of 4 mA to produce an SFQ in the storage loop.

This demonstration of a fundamental SFQ circuit via focused helium ion beam is important as an indication of the versatility of the direct-write technique and its capability towards increasingly complex applications. One of the ways this type of direct-written circuit may be improved is through better understanding of the underlying cause of deviation in directly-written Josephson junction parameters. Robust Josephson circuits rely on consistent fabrication of Josephson junctions, which further motivated the work in the

following sections.

4.4 Josephson Junction Arrays

The motivation to fabricate series arrays of Josephson junctions is to create wide bandwidth and high dynamic range magnetometers that may operate unshielded and without complicated lock-in electronics [153]. SQUIDs are the most common Josephson device for sensitive flux detection due to their high sensitivity to an applied magnetic flux. However, the dynamic range of SQUID magnetometers is limited by the non-linear response that is periodic with Φ_0 (on the order of 10 nT/Φ_0). Consequently, SQUIDs require additional electronics for operation in unshielded environments, referred as flux-locked loops, in order to linearize the output so that it is useful as a detector of relative changes in a magnetic field. However, these electronics limit the device bandwidth. It was mentioned in Sec. 2.7 that arrays of series and parallel junctions may be used to engineer the voltage response of the interference patterns, but this approach has drawbacks and significantly complicates fabrication. In comparison, single Josephson junctions have much larger periodicities, on the scale of $\sim$100 μT/Φ_0, so that slow electronics are unnecessary to linearize the output. While this comes at the expense of lower sensitivity, it is possible to increase it by chaining together Josephson junctions in a series array. In this section, the performance of series arrays of directly-written Josephson junctions as magnetometers will be demonstrated.

4.4.1 Flux-Focusing

The planar geometry of directly-written Josephson junctions is integral to its function as a magnetometer by effectively increasing its sensitivity to an applied magnetic field as outlined in Sec. 4.1.2. Additionally, it is essential in a magnetometer that is based on series arrays of Josephson junctions for each junction to be normal to, and hence sensitive to, the the same applied magnetic flux. With focused helium ion beam microscopy, it is possible to direct-write Josephson barriers without restraint. The geometry of a series array of directly-written Josephson junctions is portrayed in Fig. 4.25. While the geometry of the arrayed Josephson junctions are set by considerations from Sec. 4.1, there is a parameter of the array geometry that needs to be optimized. The inter-junction spacing is the distance between adjacent Josephson junctions. Similar to the single planar junction case, there is a flux-focusing in the array as the Meissner effect expels magnetic flux from the bulk superconducting electrode that connects adjacent junctions. An additional consideration is that for junctions with inter-junction spacing less than the penetration depth, they no longer act independently of one another. This condition sets the lower bound for inter-junction spacing for a series array of Josephson junctions intended for sensitive magnetic flux detection. It is predicted that due to the array flux-focusing effect that the magnetic flux sensitivity of a series array of planar Josephson junctions will increase as the inter-junction spacing increases until the effect saturates when the inter-junction spacing is greater than the width of the superconducting electrode.

The flux-focusing behavior in series arrays of Josephson junctions was investigated by fabricating several arrays comprised of 20, 30-μm wide Josephson junctions in series

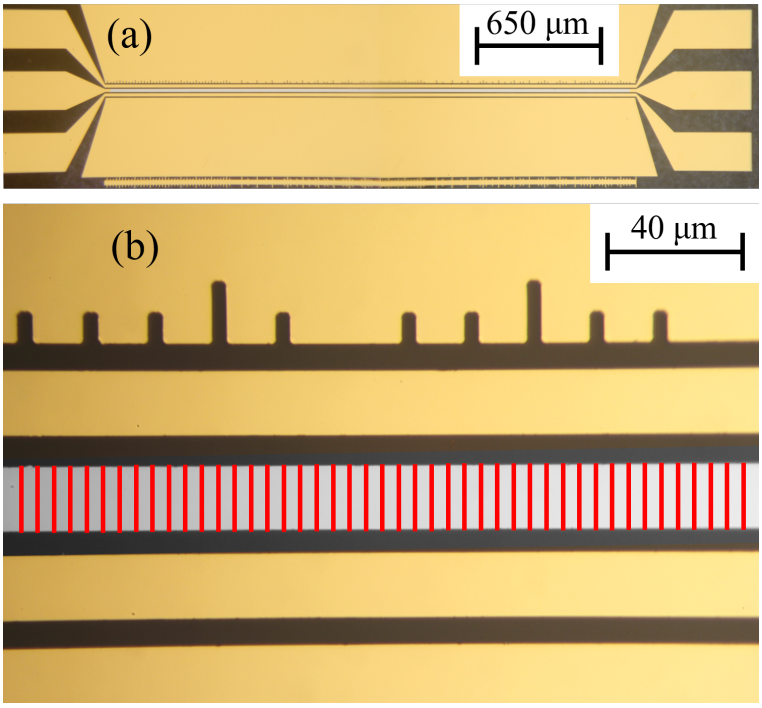

Figure 4.25: Image of series array of planar Josephson junctions intended as a transducer for magnetic fields to voltage. (a) Full view of layout design consisting of two on-chip control lines for magnetic bias parallel to the bulk superconductor electrode for fabrication of Josephson junctions. (b) Detailed view of area where junctions are written. Grey indicates aperture to YBCO. Red lines indicate location where Josephson junctions are written. Lithographically defined tick marks are for focused ion beam alignment [154].

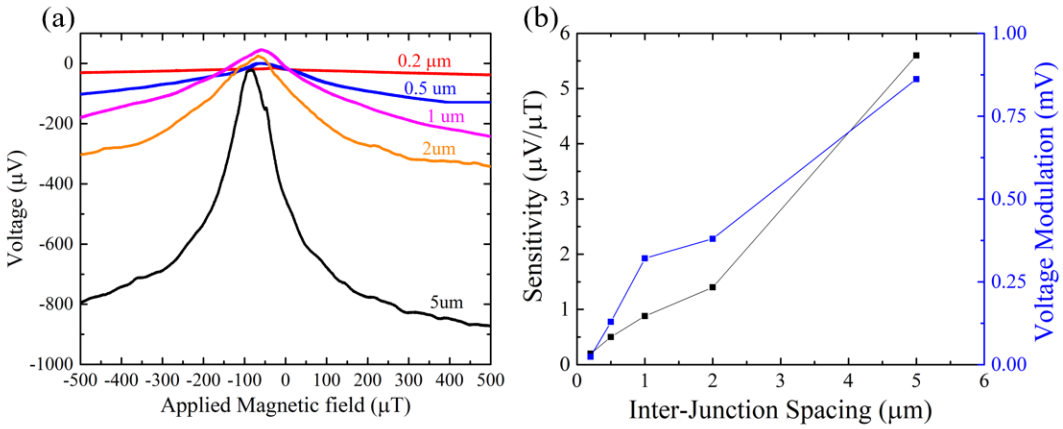

Figure 4.26: Characteristics of magnetic flux-focusing effect in series arrays of planar Josephson junctions. (a) Voltage-magnetic field characteristics, (b) sensitivity, (left) and voltage modulation (right) vs. the inter-junction spacing.

with inter-junction spacings of .2, .5, 1, 2, and 5 μm. All other parameters were keep constant. The arrays were written with an ion fluence of 4×10^{16} ions/cm^2 and featured SNS-like temperature trends from the current-voltage characteristics. Each device was characterized at 60 K. The voltage-applied magnetic field of these devices are presented in Fig. 4.26a. An increase in overall voltage modulation is observed as the inter-junction spacing is increased. Voltage modulation was extracted by taking the difference between the global minima and maxima in the voltage-applied magnetic field characteristics. This increase in voltage modulation relates directly to an increase in the sensitivity. In this section, sensitivity is defined by applying a linear fit to the voltage-applied magnetic field characteristics in the maximized region where the fits featured Pearson's correlation values greater than .999. Voltage modulation and sensitivity are plotted against the inter-junction spacing in Fig. 4.26b. It is suggested that this increase in voltage modulation is resultant of the summing of more concentrated zero-bias peaks due to flux-focused arrays in comparison

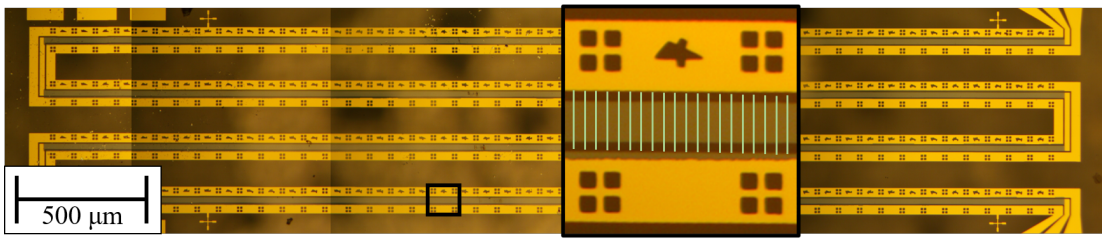

Figure 4.27: Optical image of the layout design geometry for the automated fabrication of the series arrays of planar Josephson junctions. Intended to interface with the automatic focusing and driving features of the Raith ELPHY software. Inset is zoom in on single writefield indicated where Josephson barriers are written as indicated by the green lines [138].

to the more dispersed peaks that would result in arrays with small inter-junction spacing.

4.4.2 Series Arrays of Planar Josephson Junctions as Magnetometers

Arrays of planar Josephson junctions were fabricated to estimate the scaling effects of these devices, as well as, to characterize their performance as a sensitive detector of magnetic flux. The geometry of the design is indicated in Fig. 4.27. Initially, arrays of several hundred Josephson junctions were painstakingly fabricated by manually writing individual writefields. It was determined from these devices in order to produce a device that was comparable to the sensitivity of a SQUID, the number of Josephson junctions in series would need to be increased by an order of magnitude. This motivated the work for large-scale lithography via helium ion microscopy, which is elaborated on in Sec. 3.1.3. This automated technique allowed for fabrication of arrays with thousands of directly-written Josephson junctions. The fabrication parameters of these devices are summarized in Table 4.1.

The samples A10, A20, B350, and were cooled to 77 K for characterization. De-

Identifier	l (μm)	Dose (ions/cm^2)	Δ_J (μm)	N
A10	10	4×10^{16}	2	600
A20	20	4×10^{16}	2	600
B350	20	7×10^{16}	5	400
B400	20	8×10^{16}	5	400
B1	20	5×10^{16}	5	2640
B2	20	6×10^{16}	5	2640

Table 4.1: Fabrication parameters for the series arrays of Josephson junctions for sensitive detection of magnetic flux. In text specific arrays are referred to by their device identifier. Δ_J is the inter-junction spacing, and N is the number of junctions. Devices with identifiers that start with A were fabricated on a Zeiss Orion Nanofab, whereas B devices were fabricated on a Zeiss Orion Plus.

Identifier	T (K)	Mean I_C (μA) (σ)	R (Ω)	S (mV/mT)	O (μT)	N at 10 Hz (pT Hz$^{-1/2}$)	D (dB)
A10	77	198 (26%)	91	8.4	330	-	-
A20	77	597 (23%)	37	8.5	240	-	-
B350	77	269 (26%)	12	16.7	146	572	108
B400	77	158 (41%)	16	24	199	368	115
B1	60	302 (34%)	246	400	27	512	102
B2	40	259 (30%)	537	1700	10	227	93

Table 4.2: Characteristics of each series array of planar Josephson junctions. T is the temperature at which the device was characterized. I_C is the mean value of fitted parameters I_{Ck}, σ is the fitting I_C deviation, R is the array normal state resistance, S is the sensitivity, O is the operating range, N is the noise, and D is the dynamic range.

vices B1 and B2 were characterized at a temperature where their sensitivity to an applied magnetic field was maximized. Fig. 4.28 depicts a typical voltage-applied magnetic field characteristic for these devices. The dotted black lines and red linear fit indicate the operating region where the device exhibits a suitable response for unlocked detection of magnetic field. Typical operation of these devices would be by current biasing the device in a manner depicted by the inset of Fig. 4.28 and biasing the magnetic field to the center of the operating range indicated by the black dotted lines. The device performance characteristics are summarized in Table 4.2.

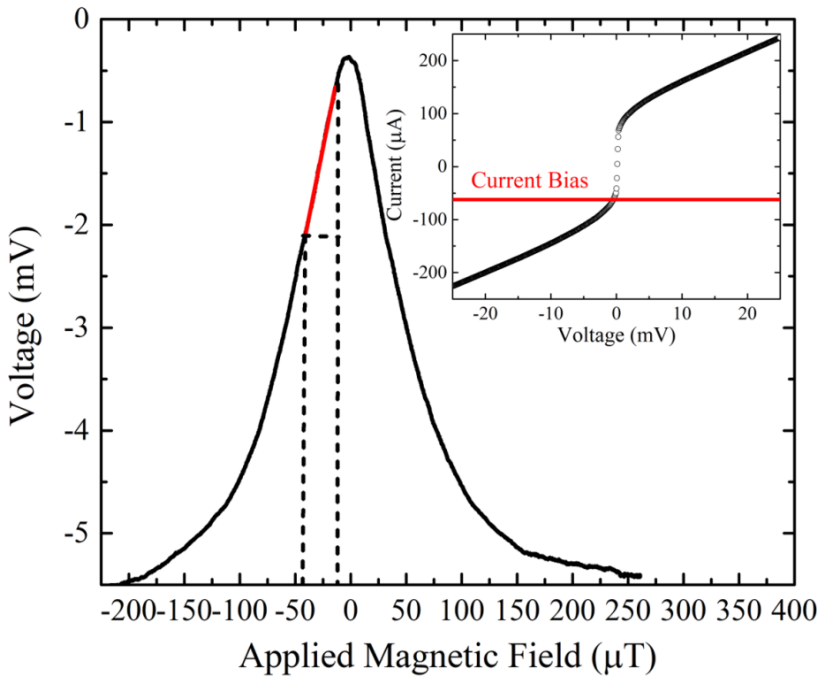

Figure 4.28: Typical voltage-applied magnetic field characteristics of a series array of planar Josephson junctions. Black dotted lines indicate an operating range in which the voltage response is approximately linear. Red line is linear fit to data. The inset depicts the corresponding current-voltage characteristics with the current bias point indicated.

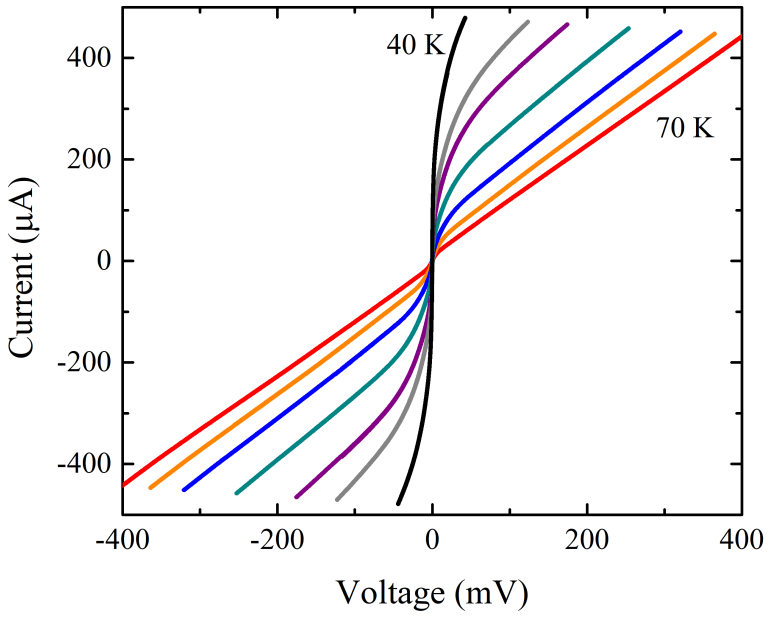

Figure 4.29: Example of temperature dependence of current-voltage characteristic of series arrays of planar Josephson junctions for device B2 for temperatures 70, 65, 60, 55, 50, 47 and 40 K.

From the current-voltage characteristics it was observed that all devices featured SNS-like dependences (See Fig. 4.29). A series RSJ array model is used to extract the device characteristics.

$$V = R\sum_{k=1}^{N}\sqrt{I^2 - I_{Ck}^2} \tag{4.3}$$

where I_{Ck} is a set of fitting parameters that characterize the N junctions in the array. The deviations of mean I_C from the fitting scheme are listed in Table. 4.2. The mean I_C deviations likely represent overestimations in the actual Josephson junction parameter deviation because the model ignores excess currents and thermal noise, both which produce similar effects as deviation in the I_C. Furthermore, the predicted deviations for devices with

small I_C were grossly overestimated, likely due to a failure of the fitting algorithm. As such they can be considered as the maximum possible deviation. A comparison of the fits and data is presented in Fig. 4.30. It is important to note that there is not a significant increase in the Josephson junction parameter deviation between automatic and manual fabrication techniques. Consequently, we have shown that the automatic fabrication method elaborated in Sec. 3.1.3 is robust and scales to a great number of junctions.

The temperature dependence of voltage-applied magnetic field for device B2 can be viewed in Fig. 4.31. Device B2 features a sensitivity of 1.7 V/mT. To accurately quantify linearity of the voltage response, the two-tone method was utilized, which can be seen in Fig. 4.32. The device was magnetically biased and current biased into its optimum working region, then two magnetic signals at 15 kHz and 16 kHz were applied to the sample. At high input signal magnitude the side band peaks at 1 kHz and 31 kHz are clearly observed. Additionally, we observe peaks at 30 and 32 kHz which are attributed to the sum of higher order mixing terms and harmonic modes from the arbitrary waveform generator. We define a linear response by the absence of a significant primary side band peak, or that the side band peak is less than 6 dB compared to the noise floor. For device B2, this value was found to be 10.6 μT. Similar spectroscopy was performed to determine the noise level of the device. A comparison between devices B1, B2 and the background noise can be viewed in Fig. 4.33. To ensure the spectra of the device was being measured, the inset of Fig. 4.33 shows the device being turned "on" by showing its dependence on the magnetic field bias.

Series arrays of directly-written Josephson junctions in YBCO have been demon-

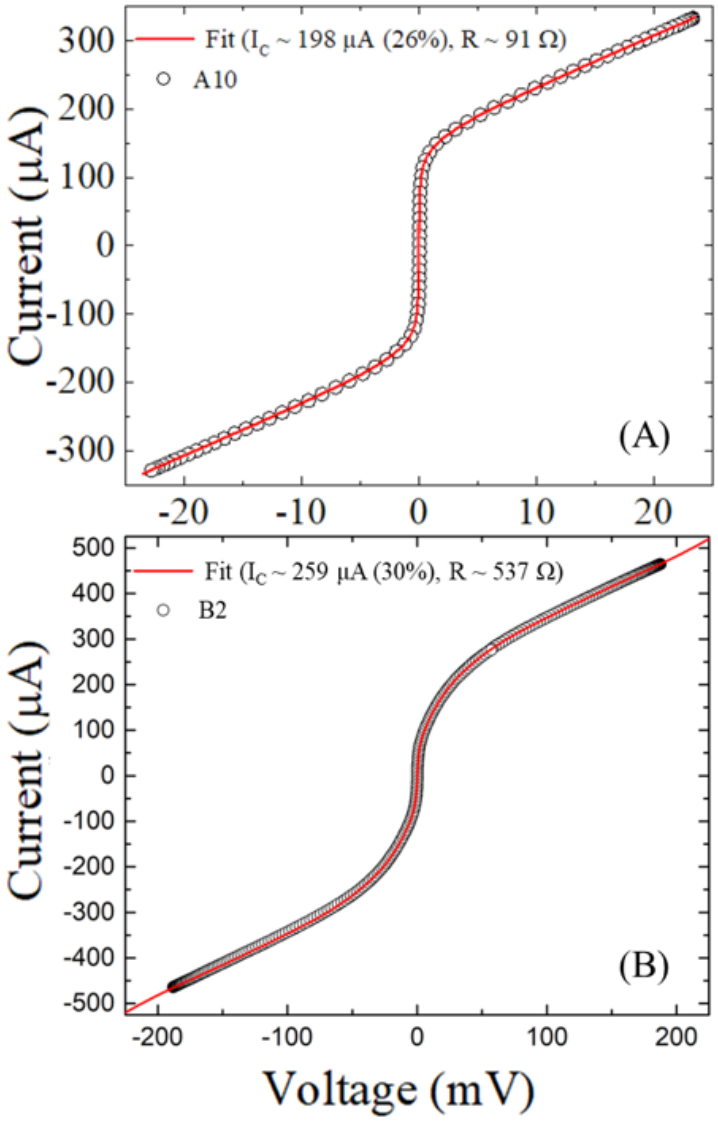

Figure 4.30: Examples of current-voltage characteristic of series arrays of planar Josephson junctions fit with a RSJ array model. (A) is device A10 and manually written while (B) is device B2 and automatically written [138].

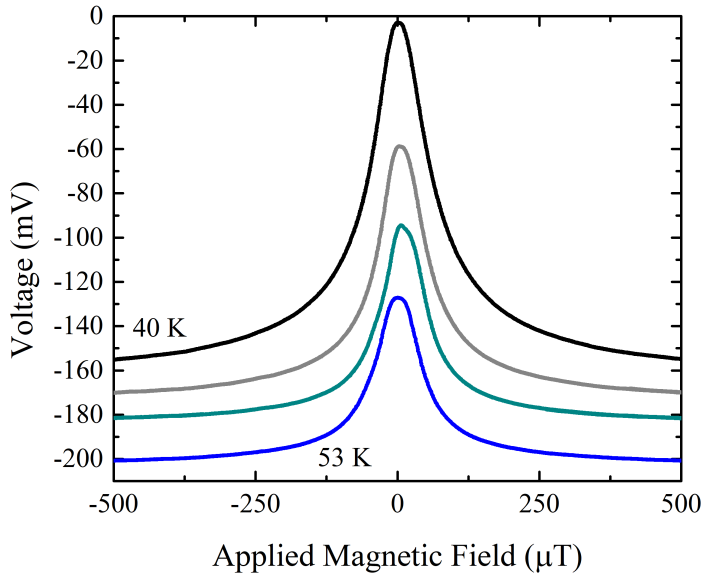

Figure 4.31: Example of voltage-applied magnetic field characteristic of series arrays of planar Josephson junctions for device B2 for temperatures 53, 50, 46, and 40 K.

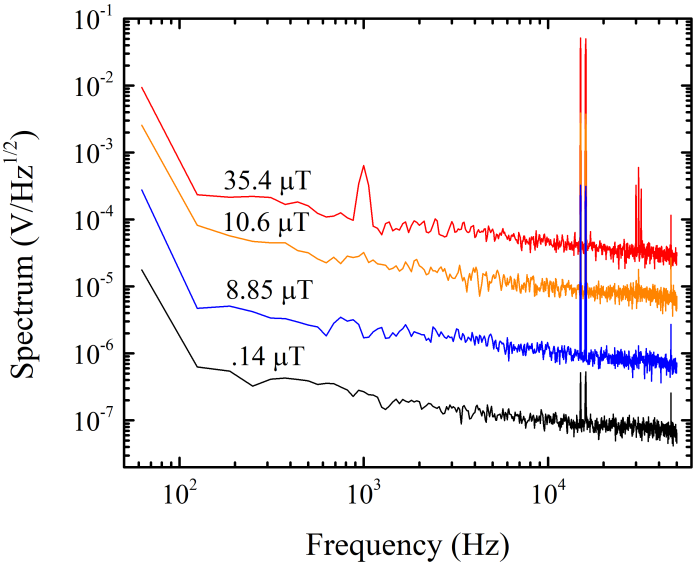

Figure 4.32: Example of two-tone spectroscopy of series arrays of planar Josephson junctions for device B2. Magnetic field signals applied at 15 and 16 kHz. Each spectra is offset by an order of magnitude for clarity.

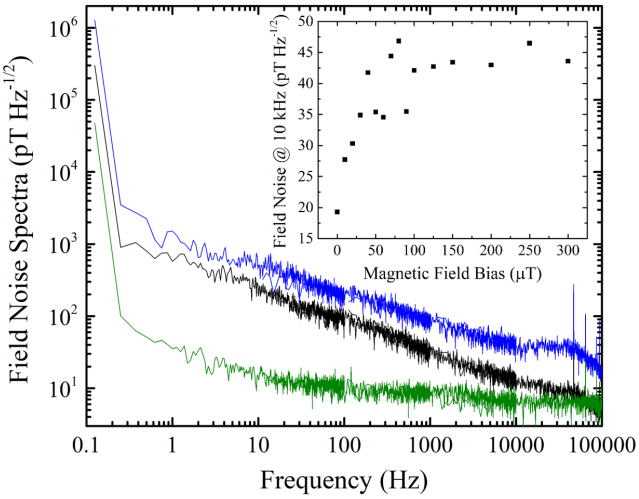

Figure 4.33: Noise spectroscopy of series arrays of planar Josephson junctions. Device B1 is blue and taken at 60 K, while device B2 spectra is given in black and taken at 40 K. The green curve is the background spectra when the device had zero applied magnetic bias and current bias. The inset shows the noise dependence on magnetic field bias at 10 kHz for B1 at 77 K while current biased at 50 μA.

strated to work in cryogenic nitrogen Dewars and feature desirable parameters for sensitive magnetometry. The transfer function is on the same magnitude of the nano-Slit SQUID presented in Ref. 4.2.1, with a response greater than 100 mV. This motivates the possibility of scaling Josephson devices via series arrays to achieve higher voltage responses so that they may interface with CMOS-based digital electronics. Furthermore, these studies in the deviation of the Josephson junction parameters motivates a deeper study of the underlying effects that cause the variation to occur.

Chapter 5

a-b Plane Angular Measurements of the Cuprate Superconducting Order Parameter

The geometry of directly-written Josephson junctions offers a unique opportunity to achieve characterization of the transport properties of cuprate superconductors in the a-b plane which has traditionally been challenging. The principle of the measurement is to measure angular dependence of the superconducting order parameter via direct tunneling experiments in the CuO plane of the cuprate. This dependence yields information of the symmetry of the pairing potential of cuprate superconductivity, which remains an open ended question.

Towards this end, we will be fabricating strong Josephson barriers in regular angles across the a-b plane so that quasi-particle tunneling can be measured across these junctions

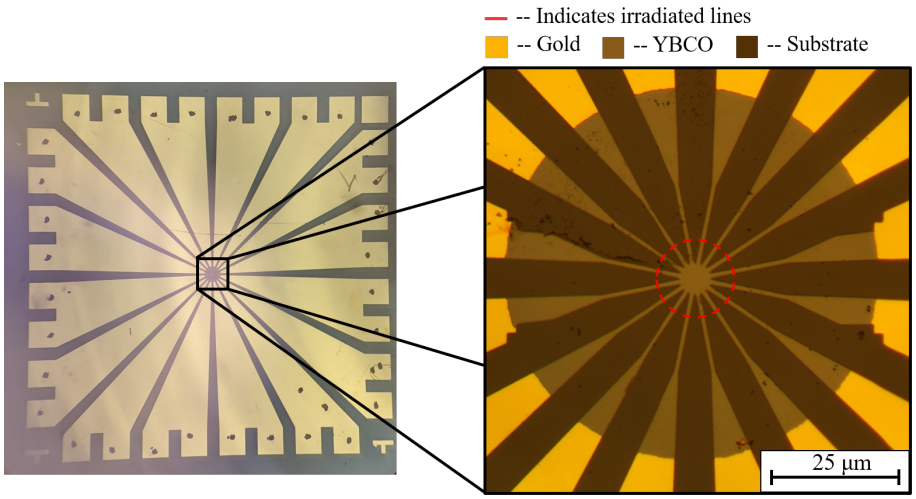

Figure 5.1: Geometry of the sample for the measurement of the angular dependence of the cuprate order parameter in the *a*-*b* plane designated Union Jack. Red lines indicate irradiated lines.

with little excess current. Measuring differential conductance vs. voltage will yield an estimation of the density of states. Two versions of this experiment were executed with slight variations to the geometry of the layout. Due to their resemblance to United Kingdom's flag, the Union Jack, and Japan's flag, the Rising Sun, the two versions will be termed as such.

5.1 YBCO

5.1.1 Union Jack

The Union Jack geometry was the first version of the experiment. It relied on lithographically defining electrodes in regular angles in the CuO plane and then direct-writing strong Josephson barriers across each one. An optical image of the geometry of the device is presented in Fig. 5.1. This geometry addresses every 22.5° in a 360° arc.

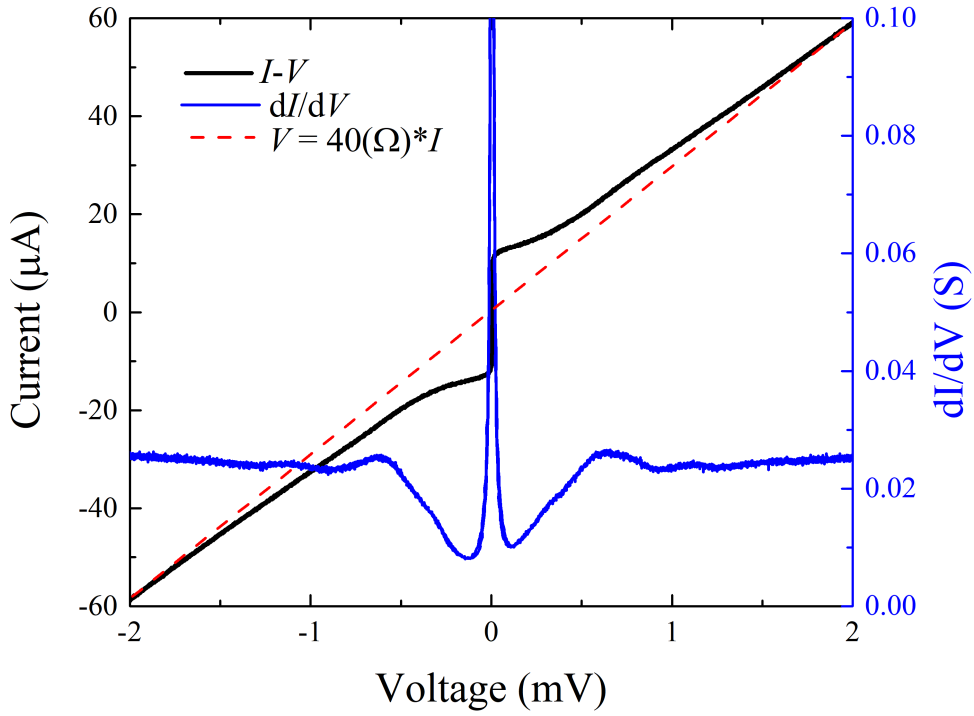

Figure 5.2: Typical current-voltage characteristic (left black axis) of a Josephson junction plotted alongside corresponding differential conductivity (right blue axis). A linear line (dotted red) with an intercept at current and voltage equal to zero fits the normal state resistance.

Transport characteristics can be taken across each individual Josephson junction. An example of a typical SIS Josephson junction current-voltage characteristic measured in the Union Jack configuration is exhibited in Fig. 5.2. In this figure, the Josephson junction featured an $I_C R$ value of 680 μV. The linear fit intercepting at (0,0) suggests insignificant presence of excess current. There is a slight asymmetry across the zero voltage bias that is clearly evident in the differential conductance measurement. This is possibly due to trapped flux. In this experiment no significant care was taken to expel residual fields due to the

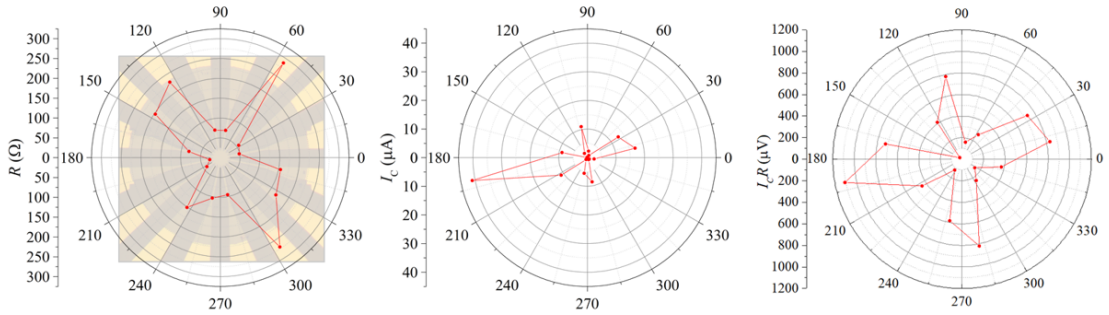

Figure 5.3: Angular dependence in the CuO plane of the Josephson junction parameters. From left to right the resistance, critical current and $I_C R$ product angular dependence is plotted.

intent to measure quasi-particle tunneling.

The current-voltage characteristics can be analyzed for each angle, as given in Fig. 5.3. It is clear that there is significant deviation in the Josephson junction parameters. There are multiple reasons for this including trapped flux, deviations in the Josephson barrier and even the anisotropy of the order parameter. In order to disentangle some of these effects. It is more accurate to measure the density of states directly via quasi-particle tunneling.

By increasing the voltage bias and measuring the differential conductance we arrive at the following Fig. 5.4. This is the density of states in the a-b plane of YBCO. Note there is no significant gap in the energy states. Dynes phenomenological model from Sec. 2.3 depicting the BCS density of states for a given thermal noise is overlaid for comparison purposes. Hence, YBCO is often referred as a "gapless" superconductor, yet herein we will refer to this region of depressed resistivity as the energy gap. It has been stated that this is evidence for d-wave symmetry as it hints at nodes in the pairing symmetry that could account for the states within the gap. The peak at zero applied voltage is the

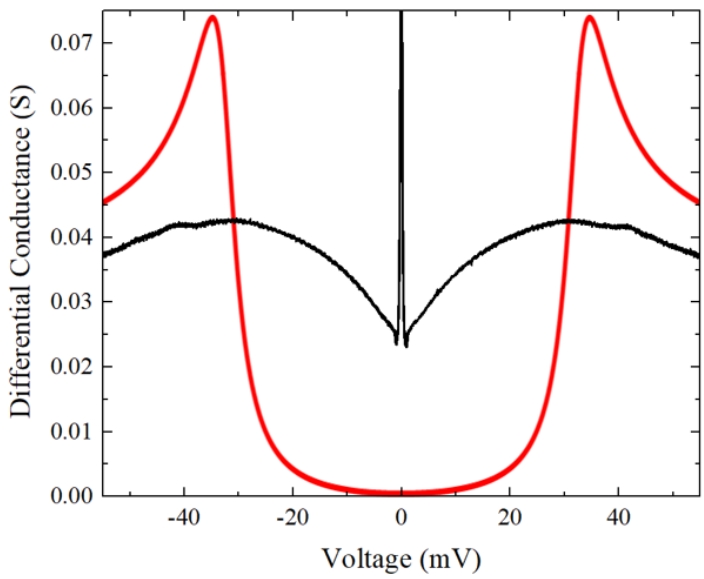

Figure 5.4: Typical differential conductance-voltage characteristic of a YBCO SIS Josephson Junction. As a comparison a red line is overlaid which is the Dynes phenomenological model for conventional superconductors.

Josephson current across the barrier. It is astonishing that this technique can resolve these two tunneling effects with energy scales that are several orders of magnitude different from each other.

Given that the density of states is unconventional, it must be rationalized as to how the order parameter is defined for cuprate materials. If we average the two global maximum on either side greater and less than the zero applied voltage and plot its temperature dependence, we resolve the following in Fig. 5.5. We see that this quantity follows closely to the temperature dependence of the BCS predicted energy gap with a coefficient of determination (R^2) equal to .994. Consequently, we define this value to be the superconducting order parameter as it seems to quantify the degree to which the material has transitioned. However, this fit to the BCS energy gap temperature dependence indicates a T_C of 76 K

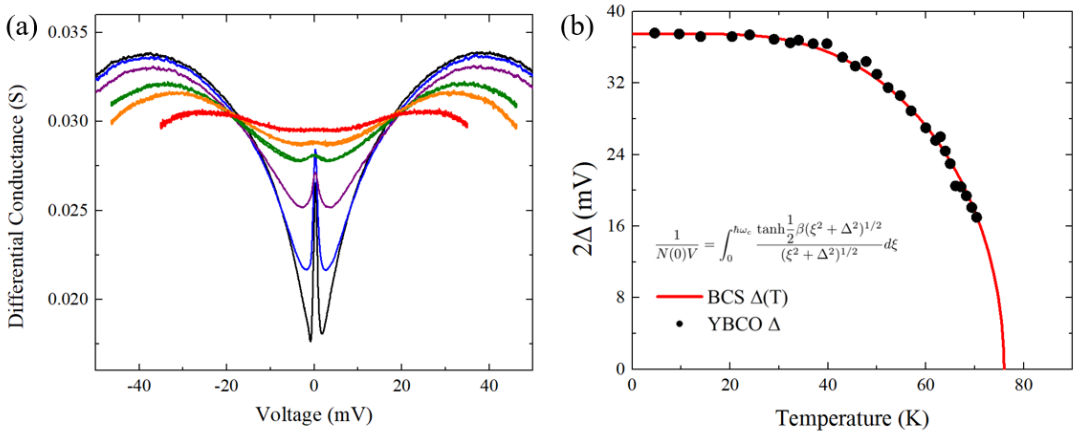

Figure 5.5: (a) Typical temperature dependence of the differential conductance of a YBCO Josephson junction with an insulating barrier for temperatures: 4.6, 20, 32, 45, 52 and 63 K. (b) Temperature dependence of the average of the peaks above and below zero applied voltage, which will be defined as the superconducting order parameter. Red line plots the BCS predicted temperature dependence of the energy gap (from Sec. 2.2.3).

which is lower than the the film T_C as determined by resistivity-temperature measurements. This is attributed to the necessary current to bias the junction to above the energy gap, which is comparable to the film critical current density at high temperatures.

It is now possible to plot the angular dependence of these peaks in the density of states to resolve the angular dependence of the superconducting order parameter. The first measurement was made on a Union Jack sample with electrode widths of 4 μm, and is presented in Fig. 5.6. It features an order parameter dependence that is relatively independent of the angle. The average energy gap value was 24.5 $\pm$ 2.3 mV. Recall that we can define a dimensionless ratio between the energy gap and the energy of the superconducting transition ($G \equiv \Delta/k_B T_C$) from Sec. 2.2.3. The transition of this circuit was determined by resistivity-temperature characteristics. We can compare G values from YBCO to the BCS predicted value. Here $G_{YBCO}^{4\mu m} = 3.5$, which is about two times $G_{BCS} \approx 1.8$.

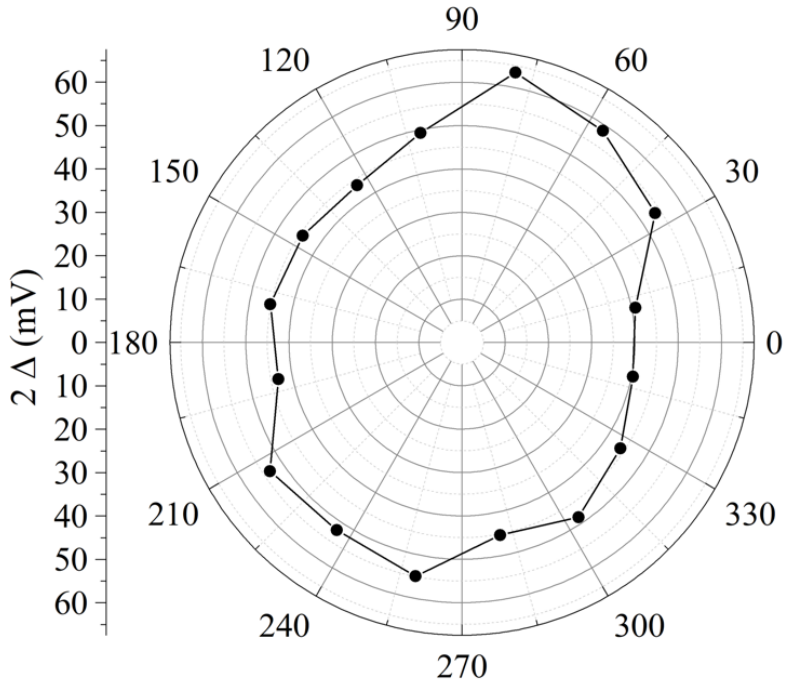

Figure 5.6: Angular dependence of YBCO superconducting order parameter in a-b plane on sample with electrode widths of 4 μm.

Two more Union Jack sample chips were fabricated and characterized each with 2 μm electrode widths. One sample was written with 7×10^{16} ions/cm^2 (UJ7), while the other slightly higher at 8×10^{16} ions/cm^2 (UJ8). Their respective energy gap polar dependencies are given in Fig. 5.7. The sample presented in Fig. 5.7a indicates two leads that were defective and measured to be an open circuit. In the UJ7 sample, the average energy gap was relatively low at 6.2 $\pm$ 1.1 mV, yielding $G_{YBCO}^{UJ7} = 1.5$. In the UJ8 sample, the average energy gap was at 13 $\pm$ 4.2 mV, yielding $G_{YBCO}^{UJ8} = 3.1$. For these samples the T_C was estimated by measuring the temperature dependence of the energy gap. It is observed that the magnitude of the energy gap has varied greatly between samples. This may be the result of variations in the films or due to the variations in the Josephson barrier. While we hypothesised this measurement would be more resilient against these types of deviations, it is possible that barriers with lower potential strength could be introducing more Andreev reflections that could obscure the peak in the conductance band that we are assuming to be indicative of the superconducting order parameter. The G parameters for UJ8 and 4 um width electrodes are comparable, while UJ7 deviates from the two and is comparable to G_{BCS}. While no nodes are observed in these measurements, there is significant deviation in the order parameter. Especially for Fig. 5.7, we observed a four-fold symmetry. However, it is suggested that the angular resolution may not have been high enough to characterize the presence of nodes.

Some criticisms of this technique for determining the actual underlying superconducting pairing symmetry stem from the nature of cuprate thin films. Due to the growth process and the strain from lattice mismatch, defects in the lattice are not uncommon which

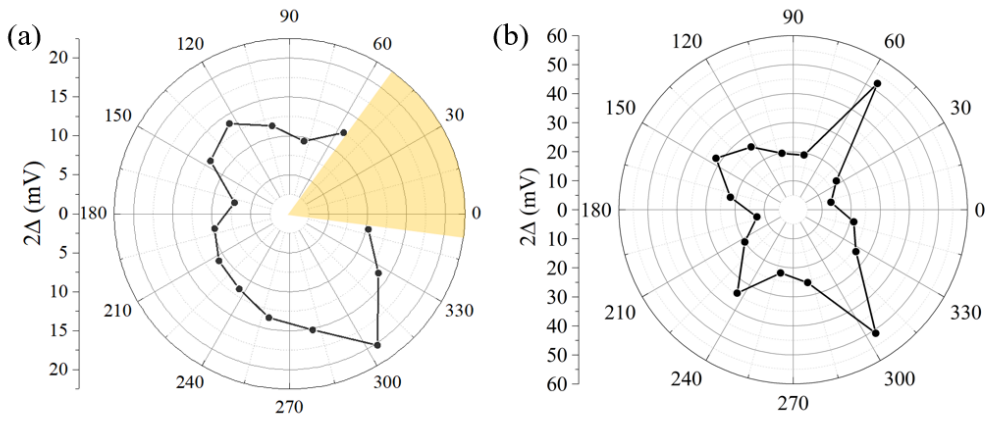

Figure 5.7: Angular dependencies of YBCO superconducting order parameters in a-b plane on samples with electrode widths of 2 μm. (a) is a sample written with 7×10^{16} ions/cm^2 and (b) gives the sample with 8×10^{16} ions/cm^2. Yellow block indicates leads that were measured as an open circuit.

may arbitrarily reflect the pairing potential along twinned boundaries or grain boundaries for instance. The orientation of these grains may also be arbitrary. In some historically important experiments, elaborated on in Sec. 2.8.2, films that were highly twinned and featured small grains were purposefully utilized. Their results suggest a "gyroscopic" nature of the film growth where orientation between grains and twinned boundaries are correlated. Consequently, at some limit we can average over them to determine the underlying symmetry. However, this limit may not be appropriate in our case. Images of the surface of the YBCO film were taken to try to discern the quality of the film. Images for UJ7 and UJ8 can be viewed in Fig. 5.8 and 5.9, respectively. Despite these criticisms this type of measurement is important for understanding the practical deviation of the order parameter, which can effect the Josephson junction parameters in our devices.

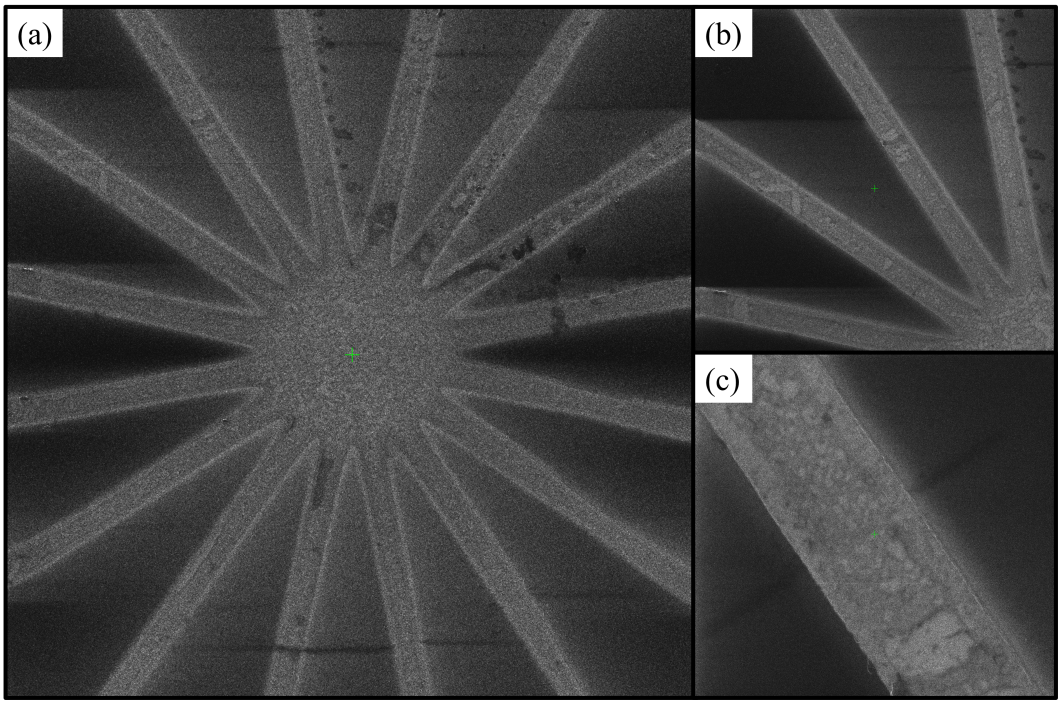

Figure 5.8: Helium focused ion beam microscope images for the surface of the YBCO sample for sample UJ7. (a) 50 μm field of view capturing each Josephson barrier. (b) 25 μm field of view zoom in on four Josephson barriers. (c) 5 μm field of view zoom in on a single directly-written Josephson junction.

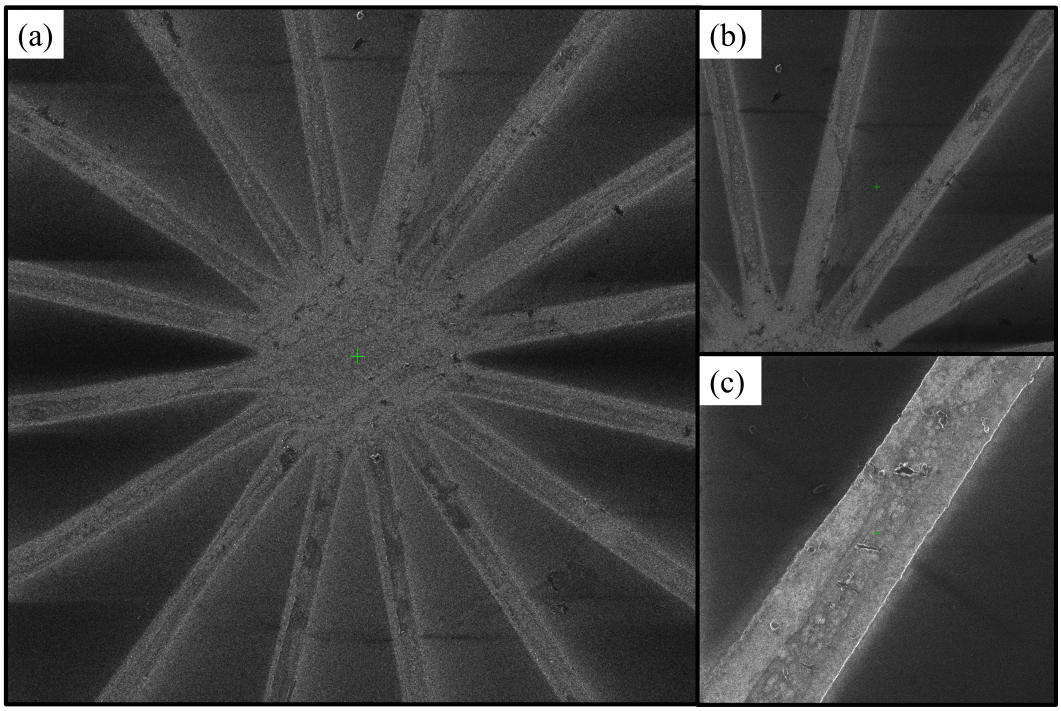

Figure 5.9: Helium focused ion beam microscope images for the surface of the YBCO sample for sample UJ8. (a) 50 μm field of view capturing each Josephson barrier. (b) 25 μm field of view zoom in on 4 Josephson barriers. (c) 5 μm field of view zoom in on a single direct written Josephson junction.

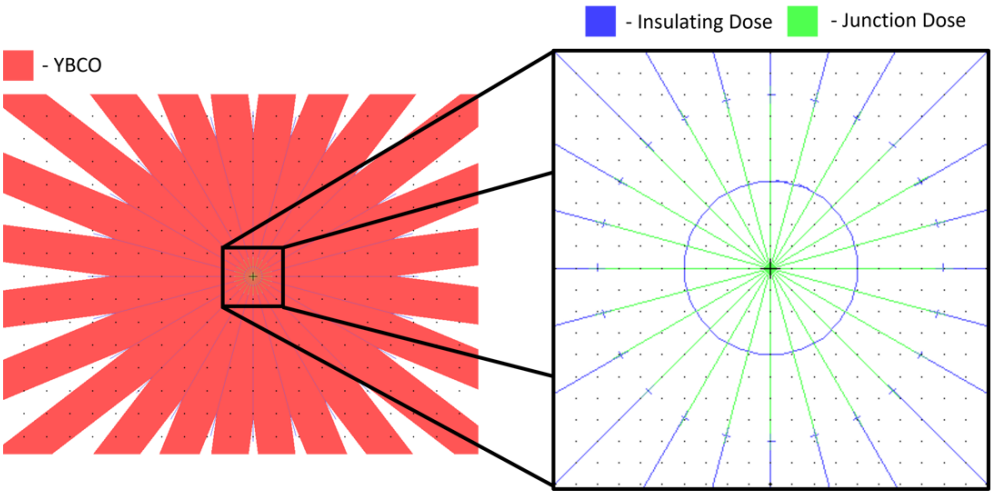

Figure 5.10: Geometry layout for the second experiment iteration to measure angular dependence of the YBCO order parameter, designated Rising Sun. The lithography is similar to the Union Jack design, except there are 24 directly-written junctions. Junctions (green lines) are directly-written in the center, zoom in on right. Insulating doses (blue lines) of ion fluence are used to isolate individual junctions for characterization. Junctions are written along the vertices of a regular icositetragon.

5.1.2 Rising Sun

To address the criticisms of the Union Jack experiment, the layout was miniaturized to be able to better characterize the region where the Josephson junctions are written. Moreover, this design reduces the chance that film defects may transform the measured pairing symmetry. Additionally, the number of junctions was increased to improve angular resolution. This experiment is designated the Rising Sun, its geometry layout is in Fig. 5.10. The layout resembles the Union Jack design, now with 24 electrodes. Junctions are written along the center of the sample where the electrodes intersect along the vertices of a regular icositetragon (24-sided polygon), probing every 15 degrees. Insulating lines are written with high doses of ion fluence to isolate the individual Josephson junctions for four-terminal

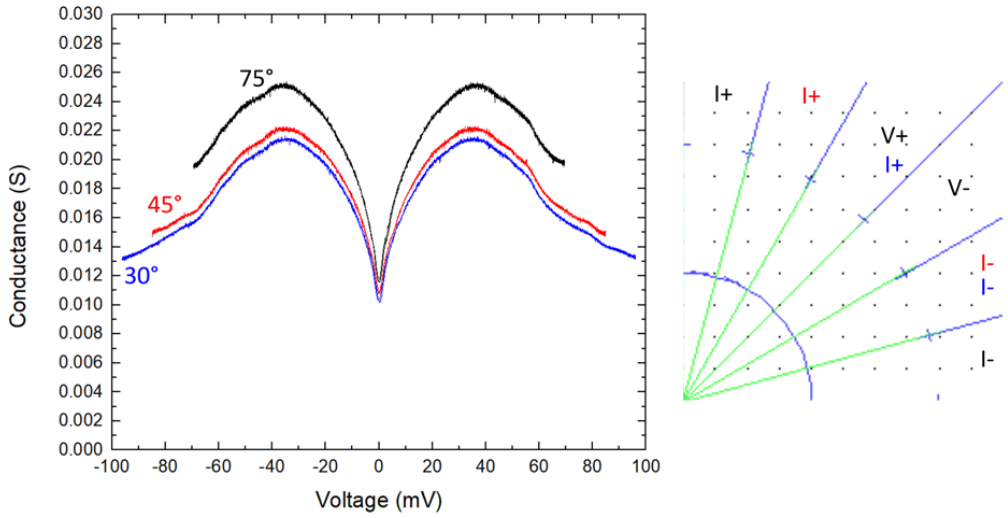

Figure 5.11: Example conductance curves from the sample designated Rising Sun and corresponding placement for the measurement terminals. Voltage probes are kept constant as three conductance curves were taken with differing current bias terminals. Each measurement was biased with the same current.

characterization. In this design all junctions are contained within an area of 4π μm^2.

Sample differential conductance curves and the corresponding placement of the 4 terminals are exhibited in Fig. 5.11. This figure demonstrates that the measurement of the energy gap is resistant to the exact placement of the current probes. The voltage probes were kept constant as the current probes were varied. This indicates that a small portion of the current will take the secondary path that bypasses the junction currently being measured. However, this should be limited to less than 5% of total applied current. Additionally, the differential current can be assumed to be roughly constant and therefore does not effect the determination of the energy gap.

The energy gap polar dependence in the *a*-*b* plane was measured for two samples that will be designated RS1 and RS2. The data and a corresponding focused ion beam

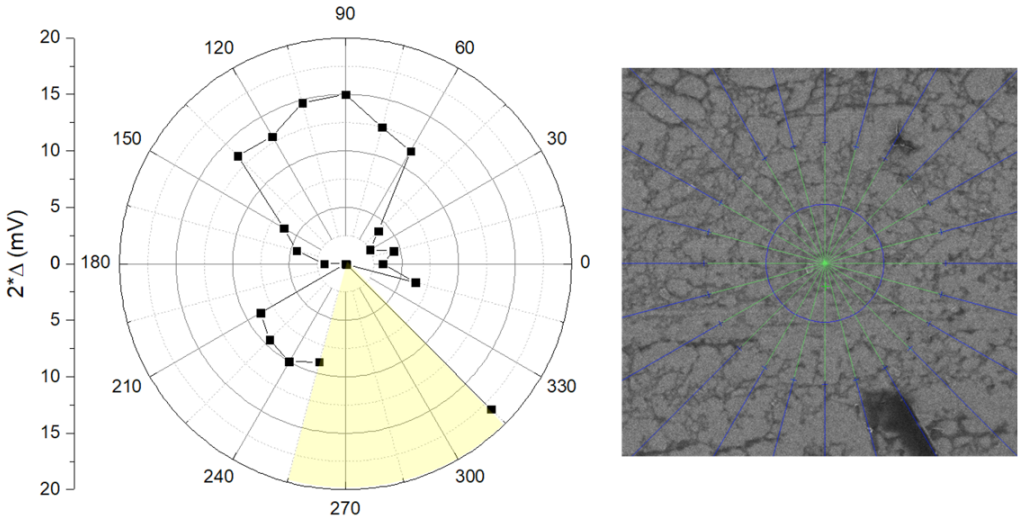

Figure 5.12: Angular dependence of energy gap data with comparison to surface image in sample designated RS1. Right image is overlaid insulating (blue lines) and Josephson barrier (green) directly-written layout.

microscopy image are arrayed for side-by-side comparison in Fig. 5.12 for RS1. The yellow region indicates electrodes that were damaged in fabrication and measured as an open circuit. This damage can be viewed in the focused ion beam microscopic image in the darkened regions which indicate insulating material. This is likely the result of charging and rapid discharge of ionic charge carriers during the direct-write process. The average Δ is 4.5 $\pm$ 4 mV, yielding an average G value of .8. For the Rising Sun experiments the T_C was determined from the energy gap dependence on temperature. In this curve we observed a two-fold symmetry with nodes along the 180 and 0 angles. This is reminiscent of the a 50%-50% mixed state symmetry of s and d. However, it should be noted that there is a feature on the surface image that aligns with these nodes and my be indicative of a film defect. This defect could have caused the node-like density of states we observed. The differential conductance curve and current-voltage characteristics along this potential node

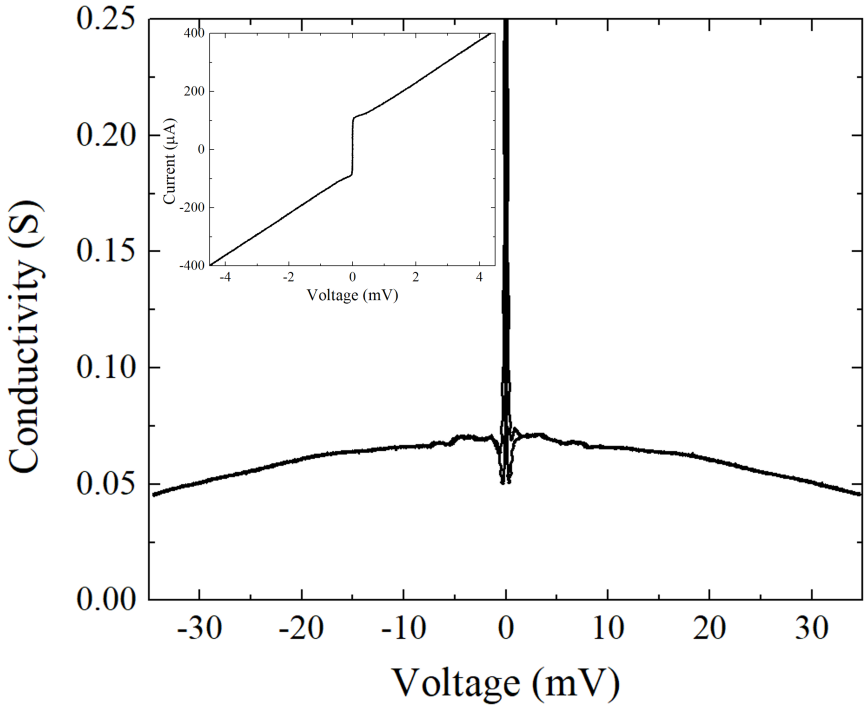

Figure 5.13: Current-voltage (inset) and differential conductance-voltage characteristics for a possible observed node along 180 degree angle in RS1.

is given in Fig. 5.13. There is no area of depressed conductance that can be observed. The current-voltage characteristics may indicate the presence of excess current.

The data for sample RS2 can be viewed in Fig. 5.14. In RS2 the same damage is present as RS1, indicating a systematic flaw in the fabrication method that can be addressed. However, this time only one lead was measured to be an open circuit and the junctions were able to be measured across separate leads. This prevented individual measurement for junctions at 285° and 300°. Instead the junctions were averaged by measuring them together in series. From Fig. 5.14, there is no evident dependence on the angle. The mean $\Delta = 14.7 \pm 2.9$ mV yielding a G value of 2.8.

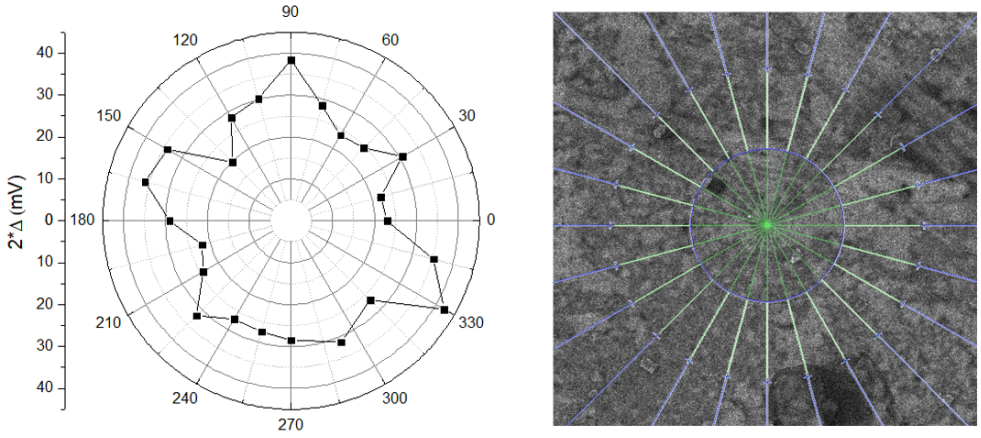

Figure 5.14: Angular dependence of energy gap data with comparison to surface image in sample designated RS2. Right image is overlaid insulating (blue lines) and Josephson barrier (green lines) directly-written layout.

5.2 HBCO

The Union Jack experiment was repeated with HBCO with 2 μm wide electrodes from the same wafer run as the Josephson junctions presented in Sec. 4.1.3. An example I-V characteristic for an SIS HBCO Josephson junction at 4.2 K is presented in Fig. 5.15. This example of a Josephson junction has a large $I_C R$ product at $\sim$840 μV. If the junction is biased out further it is possible to observe a similar structure for the differential conductance as YBCO (See Fig. 5.16). Again we will refer to the conductance peaks as the superconducting energy gap. The polar dependence of the magnitude of the voltages at which these peaks are measured are plotted in Fig. 5.17. For the HBCO sample the average Δ is 14 ± 4 mV, yielding a G of 1.8. The T_C was determined from a R-T characteristics. It seems reasonable to assume the pairing symmetries of HBCO would be the same as YBCO. The polar dependence of the HBCO film did not feature significant symmetry dependences.

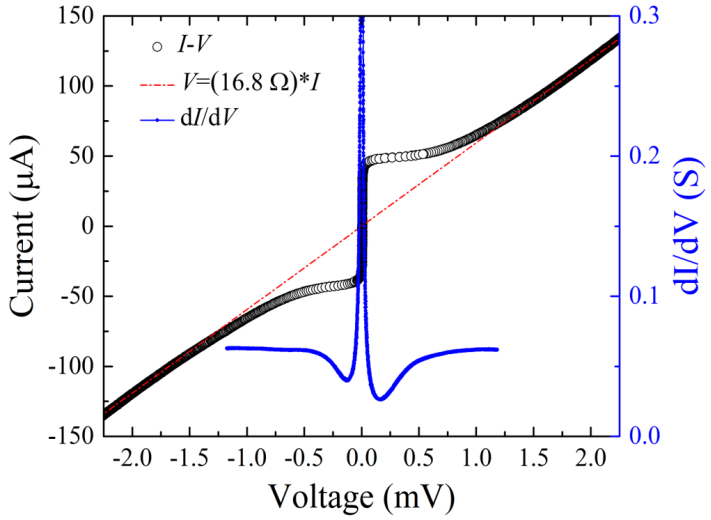

Figure 5.15: Typical current-voltage characteristic (left black axis) of an SIS HBCO Josephson junction in the Union Jack experiment plotted along the differential conductance (right blue axis). A linear line (dotted red) with an intercept at current and voltage equal to zero fits the normal state resistance.

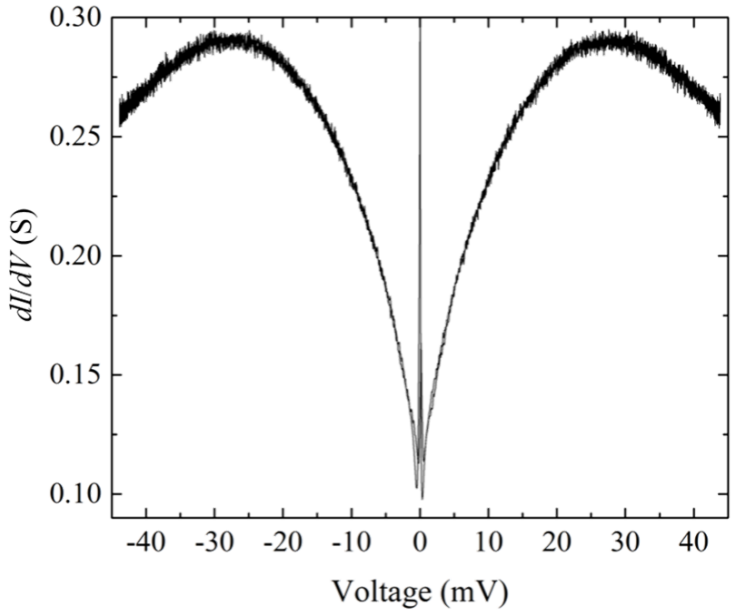

Figure 5.16: Typical differential conductance vs. voltage for a HBCO Union Jack Josephson junction biased above the energy gap.

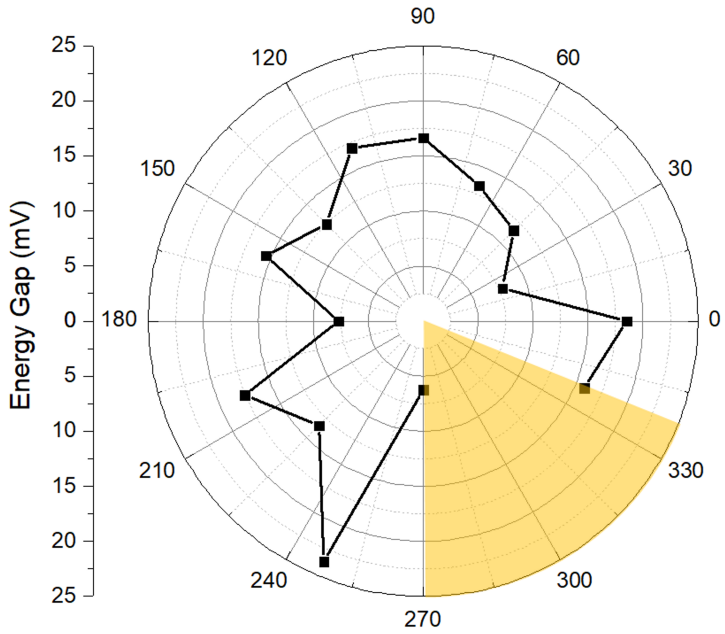

Figure 5.17: Polar dependence on the energy gap of HBCO from a Union Jack geometry. Yellow region indicates damaged leads that were unable to be measured.

5.3 BSCCO

In addition to HBCO and YBCO, we already demonstrated that the direct-write technique may be applied to BSCCO. This is a uniquely important material to perform a measurement of the polar dependence of the superconducting order parameter in the *a*-*b* plane due to the attribute that exfoliated thin film samples are single crystal. Consequently, performing a Rising Sun-like experiment in this material would not be subject to the same criticisms that are directed against films grown with defects. With a single crystal sample of exfoliated BSCCO, we can directly probe the CuO plane with directly-written Josephson junctions without concern for misorientation between the junctions due to film defects. As of writing this dissertation, this is an ongoing collaboration with my colleague Yan-Ting Wang.

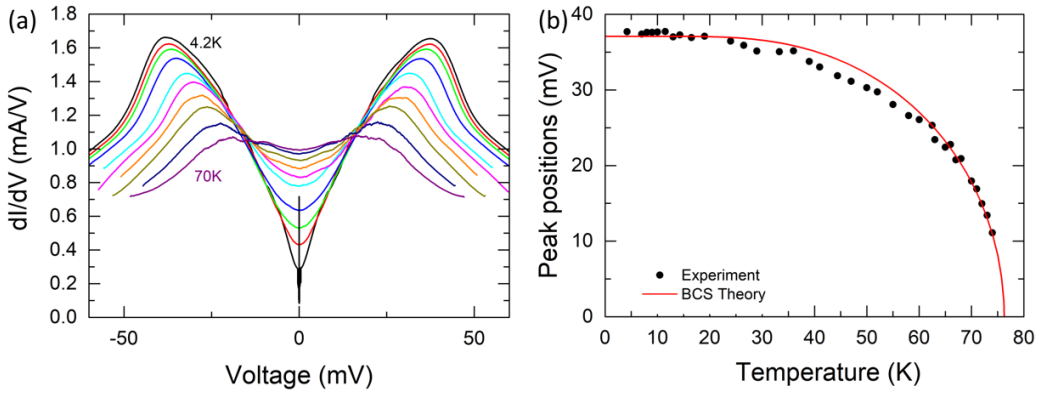

Figure 5.18: (a) Differential conductance temperature dependence of a directly-written Josephson junction in a single crystal exfoliated sample of BSCCO. (b) Temperature dependence of the conductance peak positions compared to the BCS predicted energy gap dependence.

We've already demonstrated SIS Josephson junctions directly-written in thin films of exfoliated BSCCO in Sec. 4.1.4. In order to voltage bias the BSCCO Josephson junction to above the energy gap without current biasing greater than the intrinsic junction I_C, we required a very resistive junction. A Josephson junction with $l = 400$ nm was written with a dose of 7×10^{16} ions/cm^2. The differential conductance of this junction was measured and is presented in Fig. 5.18. In this junction the energy gap is 19 mV at 4.2 K, which resulted in a G value of 2.9. The T_C is determined by a fitting to the predicted BCS temperature dependence and is estimated to be 76 K. The R^2 value of the BSCCO energy gap dependence fit to a BCS prediction is .983. Several attempts at measuring the polar dependence have been attempted in these films and is expected to be presented in the near future.

5.4 Cuprate Pairing Potential Analysis

A common density of states was observed among the various samples and cuprate types that was measured and presented within this chapter. These differential conductance curves are consistent with prior art measurements that propose gap-less densities of states in cuprates in the superconducting state. In our measurements of directly-written tunnel barriers, there appears to be a greater number of quasi-particles within the superconducting order parameter. This could be the result of a weaker tunnel barrier. However, our transport measurements indicate a strong barrier is created with helium ion beam irradiation. Consequently, it is believed that the deviation between the curves presented herein and the prior art is due to the effects of tunneling within the *a*-*b* plane and tunneling between two superconductors of the same material. Additionally, we observed an average G value across all our measurements of $\sim$2.6, which may be compared to the G_{BCS} value of 1.8. This constitutes evidence of features that deviates significantly from the BCS prediction.

While several of our observations deviate from the BCS predictions, the temperature dependence of the observed peaks in the conduction band closely follow the BCS temperature dependence of the order parameter. Therefore, without observation of a distinct energy gap, we refer to these peaks as the superconducting order parameter, which is synonymous with the energy gap in BCS theory. Careful measurement of this feature in the *a*-*b* plane may yield information on the pairing potential symmetry that is the underlying mechanism for high-T_C superconductivity.

In order to make a statement on the pairing symmetry, we will assume that the deviation of the order parameter in the polar coordinates of the *a*-*b* plane is solely due to the

anisotropy of the pairing potential. This may be a poor approximation in the case where the film deviates significantly in the spatial dimension either due to film defects or variation in oxygen concentration and causes anisotropy in the energy gap, or if there is significant deviation in barrier formation. Effects from these considerations are technically difficult to characterize and are assumed to be negligible in the following analysis.

If we consider that the deviation in the measured order parameter is purely caused by the pairing symmetry as predicted by group theory analysis, we find that if we pick some finite number of points evenly distributed across an arc of 2π radians there is a linear relation between the mixing of s and d wave and the deviation in the measured angular dependence of the order parameter. This dependence is plotted in Fig. 5.19 for symmetry mixing values e between 0 (pure d-wave) and 1 (pure s-wave). The inset of Fig. 5.19 represents the angular dependence of the magnitude of the expected order parameter for several choice values of e. We can now attribute the measured deviation to a corresponding pairing symmetry. Across all the measurements presented herein, there is a maximum average deviation in order parameter of about 30%. Therefore, we conclude that there is a mixed state pairing of s and d wave, with no more than 46% d-wave. If we omit the data from RS1, which represents an outlier of 89% deviation possibly due to a film defects, we can conclude that there is no more than 30% d-wave symmetry from the preceding measurements.

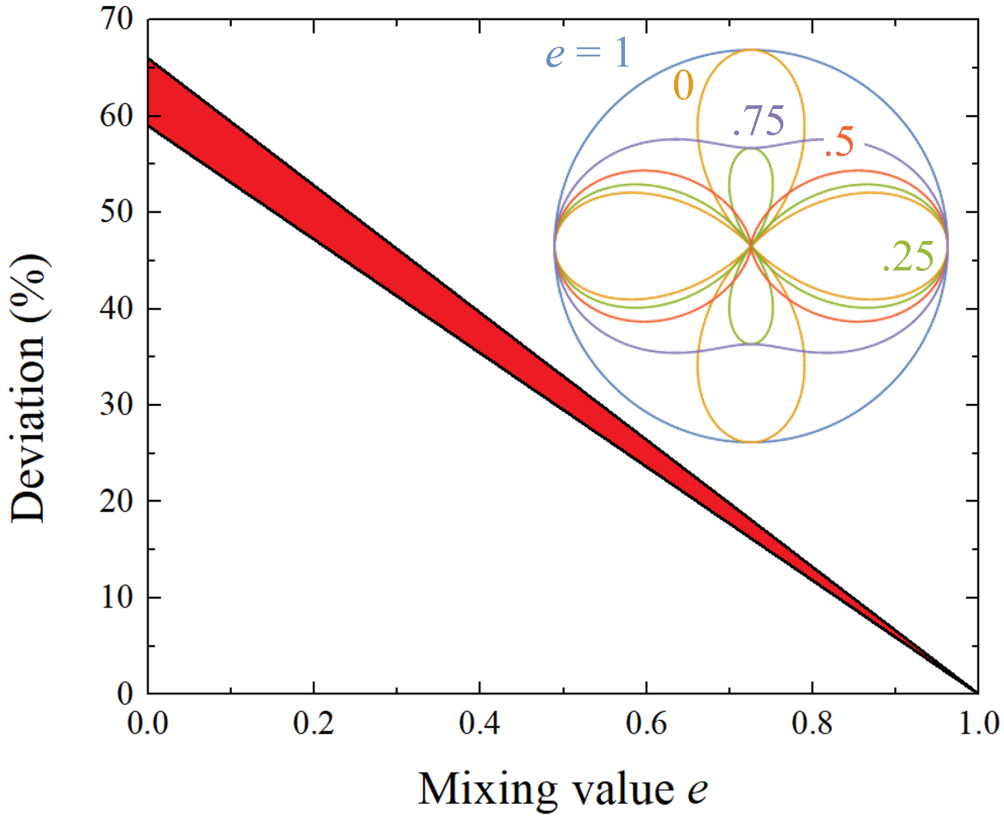

Figure 5.19: Deviation of the order parameter for a finite number of points evenly distributed across an arc of 2π radians plotted against arbitrary values of mixing between s and d state symmetries (e). The red area indicates a range that covers various arbitrary starting conditions such as number of points (16 vs. 24) and plane orientation.

Chapter 6

Conclusions

Herein, we have experimentally demonstrated the flexibility and applicability of helium ion microscopy as a resource for imaging and fabrication at the nanoscale. We specifically demonstrated the application of the direct-write technique that greatly reduces the complexity of lithography of cuprate superconducting devices. These materials are highly sensitive to ion fluence and demonstrate a metal to insulator transition. By focusing ion beam irradiation to the nanoscale, it is possible to produce interface-less Josephson junctions in the *a-b* plane of thin-films of cuprate superconductors. These Josephson junctions are highly tunable by dose, geometry and by direct-writing fundamental circuit elements in parallel. It is envisioned that engineering improvements can be made to the focused helium ion beam technology to improve consistency and expand scalability to larger and more complex wafer designs. Simultaneous *in-situ* measurement and writing of the beam current is an important technical challenge that must be overcome for improvements to the consistency of this technique. Despite an ongoing need for iteration and reform on a young

technology that is still in development, its application to research is easily demonstrated.

Several conventional Josephson devices were demonstrated via the direct-write technique that complicated superconducting devices can be comprised. High-quality SQUIDs coupled to flux concentrators in various geometries and operating at elevated temperatures are relatively facile to process in this workflow. More importantly, by taking full use of the resolution of helium ion microscopy, it is demonstrated that these superconducting circuits may be scaled down to the nanometer length scale. These fundamental Josephson devices can be integrated to produce more complicated circuits, such as single flux quanta logic. It was demonstrated that the building blocks of these logic circuits, such as Josephson transmission lines and DC to single flux converters, may be implemented via helium ion microscopy.

A revolutionary fabrication technique is a source of inspiration for the design of new experiments and technology. We wanted to leverage the sensitivity of the geometry of planar Josephson junctions for the high bandwidth and high dynamic range detection of magnetic flux. In doing so, it became possible to study the supercurrent density in these unique junctions. Furthermore, the success of demonstrating a Josephson device with a voltage output on the range of $\sim$ 100 mV is especially motivating. By further increasing the number of Josephson junctions in series, it is envisioned that voltage responses of $\sim$1 V can be attained by series arrays of $\sim$15,000 direct-written junctions. This represents less than an order of magnitude increase to the number of series junctions in the arrays presented herein. This opens the possibility of integration to more common semiconductor technologies.

Finally, this technique provided a way to directly address transport in the a-b plane of cuprate superconductors, which was an ongoing technical challenge since its discovery in the late 1980s. A technique was established to probe the polar dependence of the superconducting order parameter in cuprate superconductors. This technique provides essential evidence that can be integrated to a preponderance of historical experiments that may lead to greater understanding of the underlying physics of high temperature superconductivity. While the consensus of the scientific community at the time of writing was skewing towards pure d-wave models, this dissertation concludes that the pairing symmetry in cuprate materials features mixed-state symmetry between s and d-wave with a d-wave component that is no more than 30%.

All of these capabilities have inspired the development of advanced superconducting circuits. Advanced computing requires increasingly higher performance, necessitating research into hardware that features higher clock speeds while maintaining a low power density. Furthermore, there is motivation to increase the density of fabricated devices by scaling down and integrating into 3D hardware platforms. Increasingly, it appears that the need for hybridized circuits is ever increasing. Devices that exploit systems of several physics, each most efficient at its given task, seems to be the most tenable path forward for these ever increasingly complicated technologies. It is envisioned that superconducting circuits via the direct-write technique operating at relatively high temperatures will be part of that paradigm as high-frequency and low-dissipation devices.

Bibliography

[1] S. A. Cybart, *Planar Josephson junctions and arrays by electron beam lithography and ion damage*. University of California, San Diego, 2005.

[2] E. Y. Cho, *Focused helium beam irradiated josephson junctions*. University of California, San Diego, 2016.

[3] H. K. Onnes, "Investigations into the properties of substances at low temperatures, which have led, amongst other things, to the preparation of liquid helium," *Nobel lecture*, vol. 4, 1913.

[4] H. Kamerlingh Onnes, "The superconductivity of mercury," *Comm. Phys. Lab. Univ. Leiden*, vol. 122, pp. 122–124, 1911.

[5] J. Bardeen, L. N. Cooper, and J. R. Schrieffer, "Theory of superconductivity," *Phys. Rev.*, vol. 108, no. 5, p. 1175, 1957.

[6] V. L. Ginzburg, "On the theory of superconductivity," *Il Nuovo Cimento (1955-1965)*, vol. 2, no. 6, pp. 1234–1250, 1955.

[7] A. A. Abrikosov, "The magnetic properties of superconducting alloys," *Journal of Physics and Chemistry of Solids*, vol. 2, no. 3, pp. 199–208, 1957.

[8] B. D. Josephson, "Possible new effects in superconductive tunnelling," *Phys. Lett.*, vol. 1, no. 7, pp. 251–253, 1962.

[9] P. W. Anderson and J. M. Rowell, "Probable observation of the Josephson superconducting tunneling effect," *Physical Review Letters*, vol. 10, no. 6, p. 230, 1963.

[10] S. P. Benz and C. A. Hamilton, "A pulse-driven programmable Josephson voltage standard," *Applied physics letters*, vol. 68, no. 22, pp. 3171–3173, 1996.

[11] J. Clarke and A. I. Braginski, *The SQUID handbook*, vol. 1. Wiley Online Library, 2004.

[12] J. Clarke and A. I. Braginski, *The SQUID handbook. Vol. 2. applications of SQUIDs and SQUID systems*, vol. 2. Wiley Online Library, 2006.

[13] R. Jaklevic, J. Lambe, A. Silver, and J. Mercereau, "Quantum interference effects in Josephson tunneling," *Physical Review Letters*, vol. 12, no. 7, p. 159, 1964.

[14] J. M. Gambetta, J. M. Chow, and M. Steffen, "Building logical qubits in a superconducting quantum computing system," *npj Quantum Information*, vol. 3, no. 1, pp. 1–7, 2017.

[15] O. A. Mukhanov, "Energy-efficient single flux quantum technology," *IEEE Transactions on Applied Superconductivity*, vol. 21, no. 3, pp. 760–769, 2011.

[16] N. Takeuchi, D. Ozawa, Y. Yamanashi, and N. Yoshikawa, "An adiabatic quantum flux parametron as an ultra-low-power logic device," *Superconductor Science and Technology*, vol. 26, no. 3, p. 035010, 2013.

[17] J. M. Shainline, S. M. Buckley, R. P. Mirin, and S. W. Nam, "Superconducting optoelectronic circuits for neuromorphic computing," *Physical Review Applied*, vol. 7, no. 3, p. 034013, 2017.

[18] R. Cheng, U. S. Goteti, and M. C. Hamilton, "Superconducting neuromorphic computing using quantum phase-slip junctions," *IEEE Transactions on Applied Superconductivity*, vol. 29, no. 5, pp. 1–5, 2019.

[19] A. S. Arbab, L. A. Bashaw, B. R. Miller, E. K. Jordan, J. W. Bulte, and J. A. Frank, "Intracytoplasmic tagging of cells with ferumoxides and transfection agent for cellular magnetic resonance imaging after cell transplantation: methods and techniques," *Transplantation*, vol. 76, no. 7, pp. 1123–1130, 2003.

[20] S. Sepehri, E. Eriksson, A. Kalaboukhov, T. Zardán Gómez de la Torre, K. Kustanovich, A. Jesorka, J. F. Schneiderman, J. Blomgren, C. Johansson, M. Strømme, *et al.*, "Volume-amplified magnetic bioassay integrated with microfluidic sample handling and high-T_C SQUID magnetic readout," *APL bioengineering*, vol. 2, no. 1, p. 016102, 2018.

[21] M. Faley, J. Dammers, Y. Maslennikov, J. Schneiderman, D. Winkler, V. Koshelets, N. Shah, and R. Dunin-Borkowski, "High-T_C SQUID biomagnetometers," *Superconductor science and technology*, vol. 30, no. 8, p. 083001, 2017.

[22] M. N. Nabighian, J. C. Macnae, *et al.*, "Time domain electromagnetic prospecting methods," *Electromagnetic methods in applied geophysics*, vol. 2, no. Part A, pp. 427–509, 1991.

[23] A. Nekut and B. Spies, "Petroleum exploration using controlled-source electromagnetic methods," *Proceedings of the IEEE*, vol. 77, no. 2, pp. 338–362, 1989.

[24] E. Dantsker, D. Koelle, A. H. Miklich, D. T. Nemeth, F. Ludwig, J. Clarke, J. T. Longo, and V. Vinetskiy, "High-T_C three-axis dc SQUID magnetometer for geophysical applications," *Review of Scientific Instruments*, vol. 65, no. 12, pp. 3809–3813, 1994.

[25] V. K. Kornev, I. I. Soloviev, N. V. Klenov, T. V. Filippov, H. Engseth, and O. A. Mukhanov, "Performance advantages and design issues of SQIFs for microwave applications," *IEEE Transactions on Applied Superconductivity*, vol. 19, no. 3, pp. 916–919, 2009.

[26] M. Tarasov, G. Prokopenko, V. Koshelets, I. Lapitskaya, and L. Filippenko, "Integrated rf amplifier based on dc SQUID," *IEEE Transactions on Applied Superconductivity*, vol. 5, no. 2, pp. 3226–3229, 1995.

[27] C. Hilbert and J. Clarke, "Measurements of the dynamic input impedance of a dc SQUID," *Journal of low temperature physics*, vol. 61, no. 3, pp. 237–262, 1985.

[28] H. Weinstock, *Applications of superconductivity*, vol. 365. Springer Science & Business Media, 2013.

[29] F. Tafuri, *Fundamentals and frontiers of the Josephson effect*, vol. 286. Springer Nature, 2019.

[30] J. G. Bednorz and K. A. Müller, "Possible high T_C superconductivity in the Ba-La-Cu-O system," *Physik B*, vol. 64, no. 2, pp. 189–193, 1986.

[31] H. Maeda, Y. Tanaka, M. Fukutomi, and T. Asano, "A new high-T_C oxide superconductor without a rare earth element," *Jpn. J. Appl. Phys*, vol. 27, pp. L209–L210, feb 1988.

[32] M. K. Wu, J. R. Ashburn, C. J. Torng, P. H. Hor, R. L. Meng, L. Gao, Z. J. Huang, Y. Q. Wang, and C. W. Chu, "Superconductivity at 93 K in a new mixed-phase Y-Ba-Cu-O compound system at ambient pressure," *Phys. Rev. Lett.*, vol. 58, pp. 908–910, Mar 1987.

[33] F. London and H. London, "The electromagnetic equations of the supraconductor," *Proceedings of the Royal Society of London. Series A-Mathematical and Physical Sciences*, vol. 149, no. 866, pp. 71–88, 1935.

[34] W. Meissner and R. Ochsenfeld, "Ein neuer effekt bei eintritt der supraleitfähigkeit," *Naturwissenschaften*, vol. 21, no. 44, pp. 787–788, 1933.

[35] F. London, "Superfluids: Macroscopic theory of superconductivity, Vol. I.," *Science*, vol. 113, no. 2938, pp. 447–447, 1951.

[36] A. B. Pippard and W. L. Bragg, "An experimental and theoretical study of the relation between magnetic field and current in a superconductor," *Proceedings of the Royal Society of London. Series A. Mathematical and Physical Sciences*, vol. 216, no. 1127, pp. 547–568, 1953.

[37] V. L. Ginzburg and L. D. Landau, "On the theory of superconductivity," in *On superconductivity and superfluidity*, pp. 113–137, Springer, 2009.

[38] M. Tinkham, *Introduction to superconductivity*. Courier Corporation, 2004.

[39] L. N. Cooper, "Bound electron pairs in a degenerate Fermi gas," *Physical Review*, vol. 104, no. 4, p. 1189, 1956.

[40] H. Fröhlich, "Theory of the superconducting state. I. the ground state at the absolute zero of temperature," *Physical Review*, vol. 79, no. 5, p. 845, 1950.

[41] E. Maxwell, "Isotope effect in the superconductivity of mercury," *Physical Review*, vol. 78, no. 4, p. 477, 1950.

[42] C. Reynolds, B. Serin, W. Wright, and L. Nesbitt, "Superconductivity of isotopes of mercury," *Physical Review*, vol. 78, no. 4, p. 487, 1950.

[43] F. (https://physics.stackexchange.com/users/16689/fraschelle), "Superconducting gap, temperature dependence: how to calculate this integral?." Physics Stack Exchange. URL:https://physics.stackexchange.com/q/65444 (version: 2017-04-13).

[44] I. Giaever, "Electron tunneling between two superconductors," *Physical Review Letters*, vol. 5, no. 10, p. 464, 1960.

[45] V. Ambegaokar and A. Baratoff, "Tunneling between superconductors," *Phys. Rev. Lett.*, vol. 10, no. 11, p. 486, 1963.

[46] R. Dynes, V. Narayanamurti, and J. P. Garno, "Direct measurement of quasiparticle-lifetime broadening in a strong-coupled superconductor," *Physical Review Letters*, vol. 41, no. 21, p. 1509, 1978.

[47] G. Blonder, m. M. Tinkham, and k. T. Klapwijk, "Transition from metallic to tunneling regimes in superconducting microconstrictions: Excess current, charge imbalance, and supercurrent conversion," *Physical Review B*, vol. 25, no. 7, p. 4515, 1982.

[48] A. Andreev, "Thermal conductivity of the intermediate state of superconductors II," *Sov. Phys. JETP*, vol. 20, p. 1490, 1965.

[49] W. Stewart, "Current-voltage characteristics of Josephson junctions," *Applied physics letters*, vol. 12, no. 8, pp. 277–280, 1968.

[50] D. McCumber, "Effect of ac impedance on dc voltage-current characteristics of superconductor weak-link junctions," *Journal of Applied Physics*, vol. 39, no. 7, pp. 3113–3118, 1968.

[51] V. Ambegaokar and B. Halperin, "Voltage due to thermal noise in the dc Josephson effect," *Physical Review Letters*, vol. 22, no. 25, p. 1364, 1969.

[52] R. Dynes and T. Fulton, "Supercurrent density distribution in Josephson junctions," *Physical Review B*, vol. 3, no. 9, p. 3015, 1971.

[53] C. Owen and D. Scalapino, "Vortex structure and critical currents in Josephson junctions," *Physical Review*, vol. 164, no. 2, p. 538, 1967.

[54] P. A. Rosenthal, M. Beasley, K. Char, M. Colclough, and G. Zaharchuk, "Flux focusing effects in planar thin-film grain-boundary Josephson junctions," *Applied physics letters*, vol. 59, no. 26, pp. 3482–3484, 1991.

[55] S. K. Tolpygo and M. Gurvitch, "Critical currents and Josephson penetration depth in planar thin-film high-T_C Josephson junctions," *Applied physics letters*, vol. 69, no. 25, pp. 3914–3916, 1996.

[56] A. Ustinov, H. Kohlstedt, M. Cirillo, N. Pedersen, G. Hallmanns, and C. Heiden, "Coupled fluxon modes in stacked Nb/AlO_x/Nb long josephson junctions," *Physical Review B*, vol. 48, no. 14, p. 10614, 1993.

[57] D. Coon and M. D. Fiske, "Josephson ac and step structure in the supercurrent tunneling characteristic," *Physical Review*, vol. 138, no. 3A, p. A744, 1965.

[58] S. Shapiro, "Josephson currents in superconducting tunneling: The effect of microwaves and other observations," *Physical Review Letters*, vol. 11, no. 2, p. 80, 1963.

[59] E. Mitchell, K. Hannam, J. Lazar, K. Leslie, C. Lewis, A. Grancea, S. Keenan, S. Lam, and C. Foley, "2D SQIF arrays using 20 000 YBCO high R_n Josephson junctions," *Superconductor Science and Technology*, vol. 29, no. 6, p. 06LT01, 2016.

[60] S. A. Cybart, T. Dalichaouch, S. Wu, S. Anton, J. Drisko, J. Parker, B. Harteneck, and R. Dynes, "Comparison of measurements and simulations of series-parallel incommensurate area superconducting quantum interference device arrays fabricated from $YBa_2Cu_3O_{7-\delta}$ ion damage Josephson junctions," *Journal of Applied Physics*, vol. 112, no. 6, p. 063911, 2012.

[61] S. A. Cybart, S. Wu, S. Anton, I. Siddiqi, J. Clarke, and R. Dynes, "Series array of incommensurate superconducting quantum interference devices from $YBa_2Cu_3O_{7-\delta}$ ion damage Josephson junctions," *Applied Physics Letters*, vol. 93, no. 18, p. 182502, 2008.

[62] B. Taylor, S. Berggren, M. O'Brien, B. Higa, A. L. de Escobar, *et al.*, "Characterization of large two-dimensional $YBa_2Cu_3O_{7-\delta}$ SQUID arrays," *Superconductor Science and Technology*, vol. 29, no. 8, p. 084003, 2016.

[63] J. Oppenlander, T. Trauble, C. Haussler, and N. Schopohl, "Superconducting multiple loop quantum interferometers," *IEEE transactions on applied superconductivity*, vol. 11, no. 1, pp. 1271–1274, 2001.

[64] F. Steglich, J. Aarts, C. Bredl, W. Lieke, D. Meschede, W. Franz, and H. Schäfer, "Superconductivity in the presence of strong Pauli paramagnetism: $CeCu_2Si_2$," *Physical Review Letters*, vol. 43, no. 25, p. 1892, 1979.

[65] D. Jérome, A. Mazaud, M. Ribault, and K. Bechgaard, "Superconductivity in a synthetic organic conductor $(TMTSF)_2PF_6$," *Journal de Physique Lettres*, vol. 41, no. 4, pp. 95–98, 1980.

[66] K. Bechgaard, K. Carneiro, M. Olsen, F. B. Rasmussen, and C. S. Jacobsen, "Zero-pressure organic superconductor: Di-(tetramethyltetraselenafulvalenium)-perchlorate [$(TMTSF)_2ClO_4$]," *Physical Review Letters*, vol. 46, no. 13, p. 852, 1981.

[67] Y. Maeno, H. Hashimoto, K. Yoshida, S. Nishizaki, T. Fujita, J. Bednorz, and F. Lichtenberg, "Superconductivity in a layered perovskite without copper," *nature*, vol. 372, no. 6506, pp. 532–534, 1994.

[68] A. Schilling, M. Cantoni, J. Guo, and H. Ott, "Superconductivity above 130 K in the Hg–Ba–Ca–Cu–O system," *Nature*, vol. 363, no. 6424, pp. 56–58, 1993.

[69] T. Friedmann, M. Rabin, J. Giapintzakis, J. Rice, and D. Ginsberg, "Direct measurement of the anisotropy of the resistivity in the *a-b* plane of twin-free, single-crystal, superconducting $YBa_2Cu_3O_{7-\delta}$," *Physical Review B*, vol. 42, no. 10, p. 6217, 1990.

[70] J. Martindale, S. Barrett, C. Klug, K. O'Hara, S. DeSoto, C. Slichter, T. Friedmann, and D. Ginsberg, "Anisotropy and magnetic field dependence of the planar copper NMR spin-lattice relaxation rate in the superconducting state of $YBa_2Cu_3O_{7-\delta}$," *Physical review letters*, vol. 68, no. 5, p. 702, 1992.

[71] Y. Uemura, G. Luke, B. Sternlieb, J. Brewer, J. Carolan, W. Hardy, R. Kadono, J. Kempton, R. Kiefl, S. Kreitzman, *et al.*, "Universal correlations between T_C and n_s/m^*(carrier density over effective mass) in high-T_C cuprate superconductors," *Physical review letters*, vol. 62, no. 19, p. 2317, 1989.

[72] M. K. Wu, J. R. Ashburn, C. J. Torng, P. H. Hor, R. L. Meng, L. Gao, Z. J. Huang, Y. Q. Wang, and C. W. Chu, "Superconductivity at 93 K in a new mixed-phase Y-Ba-Cu-O compound system at ambient pressure," *Phys. Rev. Lett.*, vol. 58, pp. 908–910, Mar 1987.

[73] P. Benzi, E. Bottizzo, and N. Rizzi, "Oxygen determination from cell dimensions in YBCO superconductors," *Journal of Crystal Growth*, vol. 269, no. 2-4, pp. 625–629, 2004.

[74] H. Jiang, T. Yuan, H. How, A. Widom, C. Vittoria, and A. Drehman, "Measurements of anisotropic characteristic lengths in YBCO films at microwave frequencies," *Journal of applied physics*, vol. 73, no. 10, pp. 5865–5867, 1993.

[75] G. Kästner, D. Hesse, R. Scholz, H. Koch, F. Ludwig, M. Lorenz, and H. Kittel, "Microstructure defects in YBCO thin films: A TEM study to discuss their influence on device properties," *Physica C: Superconductivity*, vol. 243, no. 3-4, pp. 281–293, 1995.

[76] D. F. Johnston, "Group theory in solid state physics," *Reports on Progress in Physics*, vol. 23, pp. 66–153, jan 1960.

[77] M. Takigawa, P. C. Hammel, R. H. Heffner, and Z. Fisk, "Spin susceptibility in superconducting $YBa_2Cu_3O_7$ Knight shift," *Phys. Rev. B*, vol. 39, pp. 7371–7374, Apr 1989.

[78] S. E. Barrett, J. A. Martindale, D. J. Durand, C. H. Pennington, C. P. Slichter, T. A. Friedmann, J. P. Rice, and D. M. Ginsberg, "Anomalous behavior of nuclear spin-lattice relaxation rates in $YBa_2Cu_3O_7$," *Phys. Rev. Lett.*, vol. 66, pp. 108–111, Jan 1991.

[79] J. F. Annett, N. Goldenfeld, and A. J. Leggett, *Experimental constraints on the pairing state of the cuprate superconductors: an emerging consensus*, pp. 375–461. World Scientific Publishing Co, 1996.

[80] J. L. Tallon and J. Loram, "The doping dependence of T*–what is the real high-T_C phase diagram?," *Physica C: Superconductivity*, vol. 349, no. 1-2, pp. 53–68, 2001.

[81] R. Kleiner, F. Steinmeyer, G. Kunkel, and P. Müller, "Intrinsic Josephson effects in $Bi_2Sr_2CaCu_2O_8$ single crystals," *Physical review letters*, vol. 68, no. 15, p. 2394, 1992.

[82] C. C. Tsuei and J. R. Kirtley, "Pairing symmetry in cuprate superconductors," *Rev. Mod. Phys.*, vol. 72, pp. 969–1016, Oct 2000.

[83] A. T. Fiory, A. F. Hebard, P. M. Mankiewich, and R. E. Howard, "Renormalization of the mean-field superconducting penetration depth in epitaxial $YBa_2Cu_3O_7$ films," *Phys. Rev. Lett.*, vol. 61, pp. 1419–1422, Sep 1988.

[84] L. Krusin-Elbaum, R. L. Greene, F. Holtzberg, A. P. Malozemoff, and Y. Yeshurun, "Direct measurement of the temperature-dependent magnetic penetration depth in Y-Ba-Cu-O crystals," *Phys. Rev. Lett.*, vol. 62, pp. 217–220, Jan 1989.

[85] S. M. Anlage, B. W. Langley, G. Deutscher, J. Halbritter, and M. Beasley, "Measurements of the temperature dependence of the magnetic penetration depth in $YBa_2Cu_3O_7$ superconducting thin films," *Phys. Rev. B*, vol. 44, no. 17, p. 9764, 1991.

[86] W. N. Hardy, D. A. Bonn, D. C. Morgan, R. Liang, and K. Zhang, "Precision measurements of the temperature dependence of λ in $YBa_2Cu_3O_{6.95}$: Strong evidence for nodes in the gap function," *Phys. Rev. Lett.*, vol. 70, pp. 3999–4002, Jun 1993.

[87] N. Klein, N. Tellmann, H. Schulz, K. Urban, S. A. Wolf, and V. Z. Kresin, "Evidence of two-gap s-wave superconductivity in $YBa_2Cu_3O_{7-x}$ from microwave surface impedance measurements," *Phys. Rev. Lett.*, vol. 71, pp. 3355–3358, Nov 1993.

[88] Z. Ma, R. C. Taber, L. W. Lombardo, A. Kapitulnik, M. R. Beasley, P. Merchant, C. B. Eom, S. Y. Hou, and J. M. Phillips, "Microwave penetration depth measurements on $Bi_2Sr_2CaCu_2O_8$ single crystals and $YBa_2Cu_3O_{7-\delta}$ thin films," *Phys. Rev. Lett.*, vol. 71, pp. 781–784, Aug 1993.

[89] J. Sonier, R. Kiefl, J. Brewer, D. Bonn, J. Carolan, K. Chow, P. Dosanjh, W. Hardy, R. Liang, W. MacFarlane, *et al.*, "New muon-spin-rotation measurement of the temperature dependence of the magnetic penetration depth in $YBa_2Cu_3O_{6.95}$," *Phys. Rev. Lett.*, vol. 72, no. 5, p. 744, 1994.

[90] S. M. Anlage, D. H. Wu, J. Mao, S. Mao, X. X. Xi, T. Venkatesan, J. L. Peng, and R. L. Greene, "Surface impedance measurements of cuprate superconductors: $Nd_{1.85}Ce_{0.15}CuO_{4-\delta}$ – a case study," *Journal of Superconductivity*, vol. 7, pp. 453–458, Apr 1994.

[91] B. O. Wells, Z. X. Shen, D. S. Dessau, W. E. Spicer, D. B. Mitzi, L. Lombardo, A. Kapitulnik, and A. J. Arko, "Evidence for k-dependent, in-plane anisotropy of the superconducting gap in $Bi_2Sr_2CaCu_2O_{8+\delta}$," *Phys. Rev. B*, vol. 46, pp. 11830–11834, Nov 1992.

[92] Z.-X. Shen, D. S. Dessau, B. O. Wells, D. M. King, W. E. Spicer, A. J. Arko, D. Marshall, L. W. Lombardo, A. Kapitulnik, P. Dickinson, S. Doniach, J. DiCarlo, T. Loeser, and C. H. Park, "Anomalously large gap anisotropy in the *a-b* plane of $Bi_2Sr_2CaCu_2O_{8+\delta}$," *Phys. Rev. Lett.*, vol. 70, pp. 1553–1556, Mar 1993.

[93] Z.-X. Shen, W. Spicer, D. King, D. Dessau, and B. Wells, "Photoemission studies of high-T_C superconductors: The superconducting gap," *Science*, vol. 267, no. 5196, pp. 343–350, 1995.

[94] S. H. Liu and R. A. Klemm, "Surface state effects in high-T_C superconductors," *Phys. Rev. Lett.*, vol. 73, pp. 1019–1022, Aug 1994.

[95] R. J. Birgeneau and G. Shirane, *Physical properties of high temperature superconductors*. World Scientific, Singapore, 1989.

[96] H. F. Fong, B. Keimer, P. W. Anderson, D. Reznik, F. Dogan, and I. A. Aksay, "Phonon and magnetic neutron scattering at 41 meV in $YBa_2Cu_3O_7$," *Phys. Rev. Lett.*, vol. 75, pp. 316–319, Jul 1995.

[97] G. Shirane, "Magnetic excitations in $YBa_2Cu_3O_{6+x}$ and Cr," *Physica B*, vol. 215, no. 1, pp. 1 – 6, 1995. Magnetism and Superconductivity.

[98] T. Staufer, R. Nemetschek, R. Hackl, P. Müller, and H. Veith, "Investigation of the superconducting order parameter in $Bi_2Sr_2CaCu_2O_8$ single crystals," *Phys. Rev. Lett.*, vol. 68, pp. 1069–1072, Feb 1992.

[99] T. P. Devereaux, D. Einzel, B. Stadlober, R. Hackl, D. H. Leach, and J. J. Neumeier, "Electronic raman scattering in high-T_C superconductors: A probe of d_x^2-y^2 pairing," *Phys. Rev. Lett.*, vol. 72, pp. 396–399, Jan 1994.

[100] R. A. Klemm and S. H. Liu, "Role of normal layers in penetration depth determinations of the pairing state in high- T_c superconductors," *Phys. Rev. Lett.*, vol. 74, pp. 2343–2346, Mar 1995.

[101] A. G. Sun, D. A. Gajewski, M. B. Maple, and R. C. Dynes, "Observation of Josephson pair tunneling between a high-T_C cuprate ($YBa_2Cu_3O_{7-\delta}$) and a conventional superconductor (Pb)," *Phys. Rev. Lett.*, vol. 72, pp. 2267–2270, Apr 1994.

[102] A. S. Katz, A. G. Sun, R. C. Dynes, and K. Char, "Fabrication of all thin-film $YBa_2Cu_3O_{7-\delta}$/Pb Josephson tunnel junctions," *Appl. Phys. Lett.*, vol. 66, no. 1, pp. 105–107, 1995.

[103] I. Iguchi and Z. Wen, "Experimental evidence for a d-wave pairing state in $YBa_2Cu_3O_{7-y}$ from a study of $YBa_2Cu_3O_{7-y}$/insulator/Pb Josephson tunnel junctions," *Phys. Rev. B*, vol. 49, pp. 12388–12391, May 1994.

[104] D. A. Wollman, D. J. Van Harlingen, W. C. Lee, D. M. Ginsberg, and A. J. Leggett, "Experimental determination of the superconducting pairing state in YBCO from the phase coherence of YBCO-Pb dc SQUIDs," *Phys. Rev. Lett.*, vol. 71, pp. 2134–2137, Sep 1993.

[105] C. C. Tsuei, J. R. Kirtley, C. C. Chi, L. S. Yu-Jahnes, A. Gupta, T. Shaw, J. Z. Sun, and M. B. Ketchen, "Pairing symmetry and flux quantization in a tricrystal superconducting ring of $YBa_2Cu_3O_{7-\delta}$," *Phys. Rev. Lett.*, vol. 73, pp. 593–596, Jul 1994.

[106] A. Mathai, Y. Gim, R. C. Black, A. Amar, and F. C. Wellstood, "Experimental proof of a time-reversal-invariant order parameter with a π shift in $YBa_2Cu_3O_{7-\delta}$," *Phys. Rev. Lett.*, vol. 74, pp. 4523–4526, May 1995.

[107] P. Chaudhari and S.-Y. Lin, "Symmetry of the superconducting order parameter in a $YBa_2Cu_3O_{7-\delta}$ epitaxial films," *Phys. Rev. Lett.*, vol. 72, pp. 1084–1087, Feb 1994.

[108] J. H. Miller, Jr., Q. Y. Ying, Z. G. Zou, N. Q. Fan, J. H. Xu, M. F. Davis, and J. C. Wolfe, "Use of tricrystal junctions to probe the pairing state symmetry of $YBa_2Cu_3O_{7-\delta}$," *Phys. Rev. Lett.*, vol. 74, pp. 2347–2350, Mar 1995.

[109] M. Sigrist and T. M. Rice, "Unusual paramagnetic phenomena in granular high-temperature superconductors—a consequence of d/s-wave pairing?," *Rev. Mod. Phys.*, vol. 67, pp. 503–513, Apr 1995.

[110] R. A. Klemm, "Comment on 'Experimental determination of the superconducting pairing state in YBCO from the phase coherence of YBCO-Pb dc squids'," *Phys. Rev. Lett.*, vol. 73, pp. 1871–1871, Sep 1994.

[111] J. Kirtley, C. Tsuei, C. Verwijs, S. Harkema, H. Hilgenkamp, *et al.*, "Angle-resolved phase-sensitive determination of the in-plane gap symmetry in $YBa_2Cu_3O_{7-\delta}$," *Nature Physics*, vol. 2, no. 3, p. 190, 2006.

[112] C. Berthod, I. Maggio-Aprile, J. Bruér, A. Erb, and C. Renner, "Observation of Caroli–de Gennes–Matricon vortex states in $YBa_2Cu_3O_{7-\delta}$," *Phys. Rev. Lett.*, vol. 119, p. 237001, Dec 2017.

[113] Y. Zhong, Y. Wang, S. Han, Y.-F. Lv, W.-L. Wang, D. Zhang, H. Ding, Y.-M. Zhang, L. Wang, K. He, R. Zhong, J. A. Schneeloch, G.-D. Gu, C.-L. Song, X.-C. Ma, and Q.-K. Xue, "Nodeless pairing in superconducting copper-oxide monolayer films on $Bi_2Sr_2CaCu_2O_{8+\delta}$," *Science Bulletin*, vol. 61, pp. 1239–1247, Aug 2016.

[114] M. I. Faley, P. Reith, V. S. Stolyarov, I. A. Golovchanskiy, A. A. Golubov, H. Hilgenkamp, and R. E. Dunin-Borkowski, "π-loops with ds Josephson junctions," *IEEE Trans. Appl. Supercond.*, vol. 29, pp. 1–5, Aug 2019.

[115] H. Edwards, J. Markert, and A. De Lozanne, "Energy gap and surface structure of $YBa_2Cu_3O_{7-\delta}$ probed by scanning tunneling microscopy," *Physical review letters*, vol. 69, no. 20, p. 2967, 1992.

[116] K. Kitazawa, M. Nantoh, S. Heike, A. Takagi, H. Ikuta, and T. Hasegawa, "Superconducting gap observed by the atomic-site tunneling spectroscopy on YBCO and BSCCO," *Physica C: Superconductivity*, vol. 209, no. 1-3, pp. 23–26, 1993.

[117] H. Kimura, R. Barber Jr, S. Ono, Y. Ando, and R. Dynes, "Josephson scanning tunneling microscopy: A local and direct probe of the superconducting order parameter," *Physical Review B*, vol. 80, no. 14, p. 144506, 2009.

[118] M. Gurvitch, J. M. Valles, R. C. Dynes, A. Cucolo, and L. Schneemeyer, "Reproducibility in tunneling achieved through liquid etching of YBCO," *Physica C: Superconductivity and its Applications*, vol. 162, pp. 1067–1068, 1989.

[119] A. Cucolo, R. Di Leo, P. Romano, L. Schneemeyer, and J. V. Waszczak, "YBCO/Pb tunnel junctions: reproducibility, cyclability and role of the oxygen content at the YBCO surface," *IEEE transactions on magnetics*, vol. 27, no. 2, pp. 1349–1352, 1991.

[120] S. A. Cybart, E. Cho, T. Wong, B. H. Wehlin, M. K. Ma, C. Huynh, and R. Dynes, "Nano Josephson superconducting tunnel junctions in $YBa_2Cu_3O_{7-\delta}$ directly patterned with a focused helium ion beam," *Nature nanotechnology*, vol. 10, no. 7, p. 598, 2015.

[121] S. K. Tolpygo, V. Bolkhovsky, T. J. Weir, L. M. Johnson, M. A. Gouker, and W. D. Oliver, "Fabrication process and properties of fully-planarized deep-submicron Nb/Al-AlO_x/Nb Josephson junctions for VLSI circuits," *IEEE transactions on Applied Superconductivity*, vol. 25, no. 3, pp. 1–12, 2014.

[122] D. Olaya, P. D. Dresselhaus, P. F. Hopkins, S. P. Benz, *et al.*, "Fabrication of high-speed and high-density single-flux-quantum circuits at NIST," in *Proceedings of 16th International Superconductive Electronics Conference*, pp. 12–16, 2017.

[123] R. Fagaly, "Superconducting quantum interference device instruments and applications," *Review of scientific instruments*, vol. 77, no. 10, p. 101101, 2006.

[124] J. Valles Jr, A. White, K. Short, R. Dynes, J. Garno, A. Levi, M. Anzlowar, and K. Baldwin, "Ion-beam-induced metal-insulator transition in $YBa_2Cu_3O_{7-\delta}$: A mobility edge," *Physical Review B*, vol. 39, no. 16, p. 11599, 1989.

[125] J. F. Annett, N. Goldenfeld, and A. J. Leggett, "Constraints on the pairing state of the cuprate superconductors," *Journal of Low Temperature Physics*, vol. 105, no. 3, pp. 473–482, 1996.

[126] S. A. Cybart, K. Chen, Y. Cui, Q. Li, X. Xi, and R. Dynes, "Planar MgB_2 Josephson junctions and series arrays via nanolithography and ion damage," *Applied physics letters*, vol. 88, no. 1, p. 012509, 2006.

[127] S. A. Cybart, S. M. Anton, S. M. Wu, J. Clarke, and R. C. Dynes, "Very large scale integration of nanopatterned $YBa_2Cu_3O_{7-\delta}$ Josephson junctions in a two-dimensional array," *Nano letters*, vol. 9, no. 10, pp. 3581–3585, 2009.

[128] E. W. Müller and K. Bahadur, "Field ionization of gases at a metal surface and the resolution of the field ion microscope," *Physical Review*, vol. 102, no. 3, p. 624, 1956.

[129] A. V. Steele, A. Schwarzkopf, J. J. McClelland, and B. Knuffman, "High-brightness Cs focused ion beam from a cold-atomic-beam ion source," *Nano futures*, vol. 1, no. 1, p. 015005, 2017.

[130] Y. Deng, Q. Huang, Y. Zhao, D. Zhou, C. Ying, and D. Wang, "Precise fabrication of a 5 nm graphene nanopore with a helium ion microscope for biomolecule detection," *Nanotechnology*, vol. 28, no. 4, p. 045302, 2016.

[131] P. Gratia, G. Grancini, J.-N. Audinot, X. Jeanbourquin, E. Mosconi, I. Zimmermann, D. Dowsett, Y. Lee, M. Grätzel, F. De Angelis, *et al.*, "Intrinsic halide segregation at nanometer scale determines the high efficiency of mixed cation/mixed halide perovskite solar cells," *Journal of the American Chemical Society*, vol. 138, no. 49, pp. 15821–15824, 2016.

[132] D. Winston, V. R. Manfrinato, S. M. Nicaise, L. L. Cheong, H. Duan, D. Ferranti, J. Marshman, S. McVey, L. Stern, J. Notte, *et al.*, "Neon ion beam lithography (NIBL)," *Nano letters*, vol. 11, no. 10, pp. 4343–4347, 2011.

[133] D. Winston, B. M. Cord, B. Ming, D. Bell, W. DiNatale, L. Stern, A. Vladar, M. Postek, M. Mondol, J. Yang, *et al.*, "Scanning-helium-ion-beam lithography with hydrogen silsesquioxane resist," *Journal of Vacuum Science & Technology B: Microelectronics and Nanometer Structures Processing, Measurement, and Phenomena*, vol. 27, no. 6, pp. 2702–2706, 2009.

[134] H. Wu, L. Stern, D. Xia, D. Ferranti, B. Thompson, K. Klein, C. Gonzalez, and P. Rack, "Focused helium ion beam deposited low resistivity cobalt metal lines with 10 nm resolution: implications for advanced circuit editing," *Journal of Materials Science: Materials in Electronics*, vol. 25, no. 2, pp. 587–595, 2014.

[135] E. Bielejec, "Deterministic positioning of defect based qubits using ion beam implantation for nanofabrication and modification," *Bulletin of the American Physical Society*, 2021.

[136] B. Ward, J. A. Notte, and N. Economou, "Helium ion microscope: A new tool for nanoscale microscopy and metrology," *Journal of Vacuum Science & Technology B: Microelectronics and Nanometer Structures Processing, Measurement, and Phenomena*, vol. 24, no. 6, pp. 2871–2874, 2006.

[137] Y. Wang, E. Y. Cho, H. Li, and S. A. Cybart, "Estimation of focused helium ion beam Josephson junction width," in *2019 IEEE International Superconductive Electronics Conference (ISEC)*, pp. 1–3, 2019.

[138] J. C. LeFebvre and S. A. Cybart, "Large-scale focused helium ion beam lithography," *IEEE Transactions on Applied Superconductivity*, vol. 31, no. 5, pp. 1–4, 2021.

[139] S. McCoy, *Rare earth cuprate analysis for high-T_C superconducting devices.* University of California, Riverside, 2020.

[140] Y. Yamauchi, Y. Hirohata, T. Hino, and M. Nishikawa, "Bubble formation on silicon by helium ion bombardment," *Applied surface science*, vol. 169, pp. 626–630, 2001.

[141] H. Kinder, P. Berberich, W. Prusseit, S. Rieder-Zecha, R. Semerad, and B. Utz, "YBCO film deposition on very large areas up to 20×20 cm^2," *Physica C: Superconductivity*, vol. 282-287, pp. 107–110, 1997.

[142] A. Ramadan, R. Gould, and A. Ashour, "On the Van der Pauw method of resistivity measurements," *Thin Solid Films*, vol. 239, no. 2, pp. 272–275, 1994.

[143] C. Rao, P. Ganguly, J. Gopalakrishnan, and D. Sarma, "Mechanism of high-temperature superconductivity in $YBa_2Cu_3O_{7-\delta}$: crucial role of oxygen," *Materials research bulletin*, vol. 22, no. 8, pp. 1159–1163, 1987.

[144] R. Poole, "New superconductors answer some questions," *Science*, vol. 240, no. 4849, pp. 146–148, 1988.

[145] J. M. Tarascon, W. R. McKinnon, L. H. Greene, G. W. Hull, and E. M. Vogel, "Oxygen and rare-earth doping of the 90-K superconducting perovskite $YBa_2Cu_3O_{7-\delta}$," *Phys. Rev. B*, vol. 36, pp. 226–234, Jul 1987.

[146] Y.-T. Wang, J. C. LeFebvre, E. Y. Cho, S. J. McCoy, H. Li, G. Gu, K. Kadowaki, and S. A. Cybart, "Fabrication of $Bi_2Sr_2CaCu_2O_{8+x}$ *ab*-plane Josephson junctions by a focused helium ion beam," *IEEE Transactions on Applied Superconductivity*, vol. 31, no. 5, pp. 1–4, 2021.

[147] E. Y. Cho, H. Li, J. C. LeFebvre, Y. W. Zhou, R. Dynes, and S. A. Cybart, "Direct-coupled micro-magnetometer with Y-Ba-Cu-O nano-slit SQUID fabricated with a focused helium ion beam," *Applied physics letters*, vol. 113, no. 16, p. 162602, 2018.

[148] H. Li, H. Cai, E. Y. Cho, S. J. McCoy, Y.-T. Wang, J. C. LeFebvre, Y. W. Zhou, and S. A. Cybart, "High-transition-temperature nanoscale superconducting quantum interference devices directly written with a focused helium ion beam," *Applied Physics Letters*, vol. 116, no. 7, p. 070601, 2020.

[149] O. A. Mukhanov, "Energy-efficient single flux quantum technology," *IEEE Transactions on Applied Superconductivity*, vol. 21, no. 3, pp. 760–769, 2011.

[150] V. V. Ryazanov, V. V. Bol'ginov, D. S. Sobanin, I. V. Vernik, S. K. Tolpygo, A. M. Kadin, and O. A. Mukhanov, "Magnetic Josephson junction technology for digital and memory applications," *Physics Procedia*, vol. 36, pp. 35–41, 2012.

[151] J. Zmuidzinas and P. L. Richards, "Superconducting detectors and mixers for millimeter and submillimeter astrophysics," *Proceedings of the IEEE*, vol. 92, no. 10, pp. 1597–1616, 2004.

[152] H. Cai, H. Li, E. Y. Cho, J. C. LeFebvre, and S. A. Cybart, "$YBa_2Cu_3O_{7-\delta}$ single flux quantum flip flop directly written with a focused helium ion beam," *IEEE Transactions on Applied Superconductivity*, vol. 31, no. 5, pp. 1–5, 2021.

[153] S. A. Cybart, T. J. Wong, R. C. Dynes, and E. Y. Cho, "Magnetic flux-to-voltage transducer based on Josephson junction arrays," Feb. 12 2019. US Patent 10,205,081.

[154] J. C. LeFebvre, E. Cho, H. Li, K. Pratt, and S. A. Cybart, "Series arrays of planar long Josephson junctions for high dynamic range magnetic flux detection," *AIP Advances*, vol. 9, no. 10, p. 105215, 2019.

[155] G. Wendin, "Quantum information processing with superconducting circuits: a review," *Reports on Progress in Physics*, vol. 80, no. 10, p. 106001, 2017.

[156] K. K. Likharev, "Superconductor digital electronics," *Physica C*, vol. 482, pp. 6–18, 2012.

[157] M. Sigrist and K. Ueda, "Phenomenological theory of unconventional superconductivity," *Rev. Mod. Phys.*, vol. 63, pp. 239–311, Apr 1991.

[158] C. N. Yang, "Concept of off-diagonal long-range order and the quantum phases of liquid He and of superconductors," *Rev. Mod. Phys.*, vol. 34, pp. 694–704, Oct 1962.

[159] J. F. Annett, "Symmetry of the order parameter for high-temperature superconductivity," *Adv. Phys.*, vol. 39, no. 2, pp. 83–126, 1990.

[160] P. J. Hirschfeld and N. Goldenfeld, "Effect of strong scattering on the low-temperature penetration depth of a d-wave superconductor," *Phys. Rev. B*, vol. 48, no. 6, p. 4219, 1993.

[161] N. E. Bickers, D. J. Scalapino, and S. R. White, "Conserving approximations for strongly correlated electron systems: Bethe-Salpeter equation and dynamics for the two-dimensional Hubbard model," *Phys. Rev. Lett.*, vol. 62, pp. 961–964, Feb 1989.

[162] P. Monthoux and D. Pines, "Spin-fluctuation-induced superconductivity and normal-state properties of $YBa_2Cu_3O_{7-\delta}$," *Phys. Rev. B*, vol. 49, pp. 4261–4278, Feb 1994.

[163] R. E. Walstedt and W. W. Warren, "Nuclear resonance studies of $YBa_2Cu_3O_{7-\delta}$," in *Mechanisms of High Temperature Superconductivity* (H. Kamimura and A. Oshiyama, eds.), (Berlin, Heidelberg), pp. 137–147, Springer Berlin Heidelberg, 1989.

[164] V. B. Geshkenbein, A. I. Larkin, and A. Barone, "Vortices with half magnetic flux quanta in 'heavy-fermion' superconductors," *Phys. Rev. B*, vol. 36, pp. 235–238, Jul 1987.

[165] M. Sigrist and T. M. Rice, "Unusual paramagnetic phenomena in granular high-temperature superconductors—a consequence of d-wave pairing?," *Rev. Mod. Phys.*, vol. 67, pp. 503–513, Apr 1995.

[166] J. Nicol, S. Shapiro, and P. H. Smith, "Direct measurement of the superconducting energy gap," *Phys. Rev. Lett.*, vol. 5, pp. 461–464, Nov 1960.

[167] C. C. C. GmbH. http://www.ceraco.de/, 2019.

[168] L. Dorosinskii, V. Nikitenko, A. Polyanskii, and V. Vlasko-Vlasov, "Influence of twins on the critical current in YBaCuO single crystals," *Physica C*, vol. 219, no. 1, pp. 81 – 86, 1994.

[169] C. A. Hamilton, C. J. Burroughs, and S. P. Benz, "Josephson voltage standard-a review," *IEEE Trans. Appl. Supercond.*, vol. 7, pp. 3756–3761, June 1997.

[170] I. HYPRES. https://www.hypres.com, 2019.

[171] N. Bergeal, J. Lesueur, M. Sirena, G. Faini, M. Aprili, J. Contour, and B. Leridon, "Using ion irradiation to make high-T_C Josephson junctions," *J. Appl. Phys.*, vol. 102, no. 8, p. 083903, 2007.

[172] T. Van Duzer and C. W. Turner, *Principles of superconductive devices and circuits*. Pearson, 1981.

[173] S. Benz, M. Rzchowski, M. Tinkham, and C. Lobb, "Fractional giant Shapiro steps and spatially correlated phase motion in 2D Josephson arrays," *Physical review letters*, vol. 64, no. 6, p. 693, 1990.

[174] G. Samara, W. Hammetter, and E. Venturini, "Temperature and frequency dependences of the dielectric properties of $YBa_2Cu_3O_{6+x}$ ($x \approxeq 0$)," *Physical Review B*, vol. 41, no. 13, p. 8974, 1990.

[175] C. Rey, H. Mathias, L. Testardi, and S. Skirius, "High dielectric constant and nonlinear electric response in nonmetallic $YBa_2Cu_3O_{6+\delta}$," *Physical Review B*, vol. 45, no. 18, p. 10639, 1992.